

GLACIAL HISTORY OF THE RWENZORI MOUNTAINS, UGANDA

A Thesis
Submitted to the Faculty
in partial fulfillment of the requirements for the
degree of

Doctor of Philosophy

in

Earth Sciences

By Margaret S. Jackson

Guarini School of Graduate and Advanced Studies
Dartmouth College
Hanover, New Hampshire

February, 2019

Examining Committee:

(chair) Meredith A. Kelly

Erich C. Osterberg

Jonathan W. Chipman

Alice M. Doughty

Joseph M. Licciardi

F. Jon Kull, Ph.D.

Dean of the Guarini School of Graduate and Advanced Studies

ABSTRACT

The tropics are a key component of Earth's climate system. Establishing the role of the tropics in past climates is crucial to assessing their likely response under future climate scenarios. Glaciers within the humid 'inner' tropics ($\sim 10^{\circ}\text{N}$ - 10°S) are particularly sensitive to changes in temperature; determining the timing and magnitude of past changes in tropical glacial extents therefore provides a valuable proxy for low-latitude paleotemperatures. Prior work investigating past glacial fluctuations in the South American tropics has established that glaciers there responded coherently to climate changes during and since the Last Glacial Maximum (LGM ~ 26.5 - 19.0 ka), but whether this pattern of change holds for other regions in the tropics remains uncertain. The Rwenzori Mountains (0.3°N , 30°E) in East Africa provide an opportunity to establish a chronology of tropical glaciation in Africa and evaluate the potential synchrony of glacial fluctuations across the low latitudes.

This dissertation applies cosmogenic-nuclide surface-exposure dating to establish a chronology of past glacial fluctuations in the Rwenzori Mountains over the last ~ 30 ka and assess the potential mechanisms that influenced these fluctuations. The chronology comprises 73 surface-exposure ages and establishes the most detailed glacial record from Africa. The Rwenzori chronology indicates that glacial retreat at the end of the LGM was underway by ~ 20 - 19 ka, coeval with glaciers in tropical South America and prior to the onset of rapid CO_2 rise at ~ 18.2 ka. I suggest that a reduced meridional thermal gradient influenced tropical glacial recession after the LGM. Deglaciation continued after the LGM, although the rate of retreat slowed between ~ 14.0 and 11.7 ka. Tropical South American glaciers show a similar pattern of post-LGM recession. Tropical glacial

fluctuations do not correspond with any single forcing mechanism during deglaciation and likely reflect the influence of multiple forcings including greenhouse gasses and atmospheric and oceanic circulation changes. By ~11.0-10.0 ka ice in multiple Rwenzori catchments retreated rapidly to near or within the late-Holocene (~4 ka-present) maxima, coherent with glacial extent changes elsewhere in the tropics. Ice extents remained restricted until ~450-270 years ago. I suggest insolation changes acted as a primary control on tropical Holocene (~11.7 ka-present) glacial extents.

ACKNOWLEDGEMENTS

I owe an immense debt of gratitude to many people that helped make this research possible. First and foremost I thank my advisor, Meredith Kelly, for inviting me to work in the Rwenzori and for her guidance and support as I progressed through the many stages and iterations of this project. I thank my thesis committee, Alice Doughty, Jonathan Chipman, Erich Osterberg, and Joe Licciardi for their advice and encouragement. James Russell introduced me to Uganda and has been a source of great support and guidance as I worked through data interpretation and writing. Jennifer Howley taught me beryllium-10 chemistry, the perfect coffee order, and how to conduct mindful lab work. David Cavagnaro, Laura Hutchison, Katherine Salamido, Daniel Propp, and Zachary Plante all helped process samples and move the project forward. Susan Zimmerman and Alan Hidy at Lawrence Livermore National Laboratory measured samples and answered my many questions. Patricia Alves, Griffin Shumway, and Mila Pilgin provided technical and administrative help more times than I can count. Suzanne Auerbach helped me navigate the grants process. Josh Landis helped me brainstorm lab weirdness, and Edward Meyer troubleshoot innumerable technical, mechanical, and philosophical issues.

This research would not have been possible without the support of the National Science Foundation, Comer Family Foundation, Sigma Xi, Dartmouth College and the Department of Earth Sciences, and the DigitalGlobe Foundation. I thank the Uganda Wildlife Authority and the Uganda National Council on Science and Technology for their support of this project. Bob Nakileza made sure the wheels kept turning and offered valuable advice and support. Rwenzori Trekking Services and Rwenzori Mountaineering

Services kept us safe and healthy while in the field. Thank you to the guides and porters who helped us make it through the mountains and kept the jaguars and forest elephants away, and who helped find the samples that comprise the final project. There would be no data without them. And also no Maggie.

I'm also grateful to Gordon Bromley and Greg Balco for inviting me to take part in their research, and for their advice and support in all scientific realms. Alexandra Balter, Lauren Farnsworth, and Holly Thomas are excellent field geologists and even better humans. The Kelly Lab Group and EARS grad students past and present gave me advice, encouragement, and a million research ideas.

Finally, Microsoft Word made things infinitely more difficult than need be. But Zelda, Ed, Howard, D'argo, Elizabeth, Esther, Josephine, Arthur, Gord, and Mum made things much easier - and a lot more fun.

TABLE OF CONTENTS

ABSTRACT.....	ii
ACKNOWLEDGEMENTS.....	iv
LIST OF TABLES.....	xi
LIST OF FIGURES.....	xii
CHAPTER 1: INTRODUCTION.....	1
1.1 MOTIVATION.....	1
1.2 BACKGROUND.....	2
1.2.1 THE RWENZORI MOUNTAINS: SETTING AND CLIMATE.....	2
1.2.2 GLACIATION IN THE RWENZORI MOUNTAINS.....	6
1.2.3 CONTROLS ON TROPICAL GLACIATION.....	8
1.3 RESEARCH OBJECTIVES AND DISSERTATION STRUCTURE.....	14
1.3.1 OBJECTIVES.....	14
1.3.2 DISSERTATION STRUCTURE.....	16
1.4 AUTHOR CONTRIBUTION STATEMENT.....	18
CHAPTER 2: METHODS.....	20
2. INTRODUCTION.....	20
2.1 GLACIAL-GEOMORPHIC MAPPING.....	20
2.2 COSMOGENIC NUCLIDE SURFACE-EXPOSURE DATING.....	21
2.2.1 COSMOGENIC NUCLIDE PRODUCTION AND THEORY.....	21
2.2.2 SAMPLING FOR ¹⁰ BE DATING.....	24
2.2.3 LABORATORY METHODOLOGY.....	25
2.2.4 EXPOSURE AGE CALCULATION.....	27

2.2.5 DATA INTERPRETATION AND RECALCULATION.....	30
CHAPTER 3: SYNCHRONOUS LOW- AND HIGH-LATITUDE WARMING AT THE ONSET OF THE LAST DEGLACIATION.....	32
3.1 ABSTRACT.....	32
3.2 INTRODUCTION.....	33
3.3 RESULTS.....	37
3.4 DISCUSSION.....	41
3.5 MATERIALS AND METHODOLOGY.....	47
3.5.1 FIELD METHODOLOGY.....	47
3.5.2 LAB METHODOLOGY.....	47
3.5.3 ¹⁰ BE AGE CALCULATION.....	48
3.5.4 RECALCULATION OF PRE-EXISTING TROPICAL ¹⁰ BE DATASETS.....	51
3.6 ACKNOWLEDGEMENTS.....	52
CHAPTER 4: GLACIAL FLUCTUATIONS IN TROPICAL AFRICA DURING THE LAST DEGLACIATION.....	54
4.1 ABSTRACT.....	54
4.2 INTRODUCTION.....	55
4.3 BACKGROUND.....	58
4.3.1 GEOLOGIC SETTING AND PREVIOUS WORK.....	58
4.3.2 STUDY SITES.....	62

4.4 METHODOLOGY.....	66
4.5 RESULTS.....	73
4.5.1 MUBUKU VALLEY.....	73
4.5.2 BUJUKU VALLEY.....	75
4.5.3 NYAMUGASANI VALLEY.....	79
4.6 DISCUSSION.....	82
4.6.1 RWENZORI ICE EXTENTS DURING TERMINATION 1.....	82
4.6.2 GLACIAL FLUCTUATIONS IN EAST AFRICA.....	86
4.6.3 GLACIAL FLUCTUATIONS IN SOUTH AMERICA.....	87
4.6.4 CONTROLS ON TROPICAL GLACIAL MASS BALANCE DURING DEGLACIATION.....	88
4.6.5 POTENTIAL CONTROLS ON TROPICAL TEMPERATURES FOLLOWING THE LGM.....	90
4.7 CONCLUSIONS.....	95
4.8 ACKNOWLEDGEMENTS.....	96
CHAPTER 5: ¹⁰ BE AGES OF GLACIAL EXTENTS IN THE RWENZORI MOUNTAINS AND THEIR IMPLICATIONS FOR HOLOCENE CLIMATE IN EAST AFRICA.....	97
5.1 ABSTRACT.....	97
5.2 INTRODUCTION.....	98
5.3 PRIOR WORK ON TROPICAL AFRICAN HOLOCENE GLACIAL EXTENTS.....	100

5.4 STUDY SITES.....	109
5.5 METHODS.....	111
5.6 RESULTS.....	113
5.7 DISCUSSION.....	118
5.7.1 RWENZORI GLACIAL EXTENTS DURING THE HOLOCENE.....	118
5.7.2 HOLOCENE GLACIAL FLUCTUATIONS ACROSS THE GLOBAL TROPICS.....	122
5.7.3 DRIVERS OF TROPICAL GLACIATION DURING THE HOLOCENE.....	123
5.8 CONCLUSIONS.....	128
5.9 ACKNOWLEDGEMENTS.....	129
 CHAPTER 6: CONCLUSIONS	129
6.1 SUMMARY OF RESULTS.....	130
6.2 FUTURE WORK.....	135
 APPENDIX A: SUPPLEMENTARY MATERIALS TO CHAPTER 3.....	138
A.1 TROPICAL ¹⁰ BE SITE DESCRIPTIONS.....	138
A.2 CLIMATIC CONTROLS ON TROPICAL GLACIATION.....	149
A.3 EVIDENCE OF OCEAN CIRCULATION CHANGE AT THE ONSET OF THE LAST DEGLACIATION.....	151
A.4 SAMPLE INFORMATION FOR CHAPTER 3.....	153

APPENDIX B: SAMPLE INFORMATION FOR CHAPTER 4.....173

APPENDIX C: SAMPLE INFORMATION FOR CHAPTER 5.....185

REFERENCES.....188

LIST OF TABLES

APPENDIX A

A1 - ^{10}Be surface-exposure age calculation input for the online calculator as described by Balco et al. (2008) and subsequently updated and measured beryllium ratios.....	153
A2 - ^{10}Be surface-exposure ages as described in Chapter 3.....	157
A3 – Summary statistics for Mahoma and Moulyambouli moraines.....	159
A4 – Age recalculations for previously reported ^{10}Be chronologies from the South American tropics.....	160
A5 – Input for the Kelly et al. (2015) calibration dataset to the online calculator as described by Balco et al. (2008) and subsequently updated.....	169

APPENDIX B

B1 – ^{10}Be surface-exposure ages as described in Chapter 4.....	173
B2 – ^{10}Be surface-exposure age calculation input for the online calculator as described by Balco et al. (2008) and subsequently updated.....	177
B3 – ^{10}Be surface-exposure sample laboratory and age-processing data.....	181

APPENDIX C

C1 – ^{10}Be surface-exposure ages as described in Chapter 5.....	185
C2 – ^{10}Be surface-exposure age calculation input for the online calculator as described by Balco et al. (2008) and subsequently updated.....	186
C3 – ^{10}Be surface-exposure sample laboratory and age-processing data.....	187

LIST OF FIGURES

CHAPTER 1

1.1 East Africa and the Rwenzori Mountains.....	4
1.2 Monthly mean precipitation in mm/day and 10 m asl winds.....	5
1.3 The Rwenzori high peaks on a clear day.....	7
1.3 Relief map of the central Rwenzori Mountains with locations mentioned in the text.....	7

CHAPTER 2

2.1 Impacts of vegetation and boulder height on ^{10}Be ages.....	30
--	----

CHAPTER 3

3.1 Map of East Africa and the Rwenzori Mountains and glacial-geomorphic maps of the Mubuku and Moulyambouli valleys with surface-exposure ages as reported in Table A1.....	35
3.2 The Rwenzori surface-exposure chronology compared with similar chronologies from the South American tropics.....	40
3.3 Glacial boundary conditions during the LGM, including insolation, sea-level, and greenhouse gas forcing, compared with the Rwenzori surface- exposure chronology.....	42
3.4 Longitudinal temperature changes at the onset of the last deglaciation from syntheses of global temperature records.....	46

CHAPTER 4

4.1 Map of East Africa and the Rwenzori Mountains.....	58
4.2 Photographs of the Mubuku, Bujuku, and Nyamugasani valleys.....	65
4.3 Individual beryllium-10 ages from Rwenzori moraines plotted versus vegetation thickness in cm and boulder height.....	71
4.4 Glacial-geomorphic map of the Mubuku and Bujuku valleys with surface- exposure ages as reported in Table B1.....	74
4.5 Glacial-geomorphic map of the Bujuku valley with surface-exposure ages as reported in Table B1.....	78
4.6 Glacial-geomorphic map of the Nyamugasani valley with surface-exposure ages as reported in Table B1.....	82
4.7 Changes in glacier extent in three Rwenzori valleys following the LGM.....	85
4.8 Global and tropical climate during the last deglaciation.....	92

CHAPTER 5

5.1 Map of East Africa and the Rwenzori Mountains.....	100
5.2 Evidence of Holocene glaciation on Mt. Kenya	102
5.3 Photos of the Rwenzori high peaks and field sites within the Bujuku and Nyamugasani valleys.....	107
5.4 ¹⁰ Be ages of the rampart moraine on the south-facing slope of Mt. Speke at the head of the Bujuku valley.....	114
5.5a ¹⁰ Be ages in the Nyamugasani valley.....	116

5.5b ^{10}Be ages in the Nyamugasani valley, including previously reported ages from the Nyamugasani 0 moraine that dams Lake Bigata and from perched boulders near Lake Kopello.....	117
5.6 Aerial photo of Mt. Weisman and the former Thomson glacier in 1937.....	121
5.7 East African climate during the Holocene.....	127

CHAPTER 6

6.1 Rwenzori glacial chronology showing arithmetic mean moraine ages in three catchments.....	131
--	-----

APPENDIX A

A1: Camel plots showing probability-distribution curves for individual moraine ages with sample age statistics.....	151
--	-----

CHAPTER 1

INTRODUCTION

1.1. Motivation

The tropics comprise nearly half the Earth's surface and are the primary source of latent heat and water vapor to the global atmosphere (Pierrehumbert, 1999). Through phenomena such as the El Niño Southern Oscillation the region is a dominant control on modern (global) inter-annual climate variability (e.g., Pierrehumbert, 1995). The tropics today are also undergoing rapid change; high-altitude regions are warming at a rate nearly twice the global average, comparable with rates of warming in the northern high latitudes (Vuille et al., 2003; 2008). Determining how the tropics will respond to future warming is fundamental to projecting accurately the impacts of global climate change and has direct ramifications for the billions who live in the low latitudes. One means of understanding recent and future change is to determine records of past climate conditions and use these to assess the mechanisms which have induced past climate changes. However terrestrial records of tropical temperatures are relatively scarce, and more records are needed to accurately reconstruct past tropical climate variability. In addition, climate models used to establish the bounds of potential future climate states are predicated upon rigorous geologic, geochemical, and ecologic reconstructions of past climate (e.g., Stocker et al., 2013). These records are used to benchmark and validate climate model output and are crucial for accurate future climate projections.

Tropical alpine glaciers provide an excellent opportunity to investigate the timing of past temperature change in the low latitudes. Glaciers within the humid 'inner' tropics

(~10°N-10°S) are particularly sensitive to changes in temperature (Kaser and Osmaston, 2002; Sagredo and Lowell, 2012; Sagredo et al., 2014) and leave an accessible geologic record of past variations in their spatial extent – and thus temperature – on the landscape (Oerlemans, 2004). Determining the timing and magnitude of past changes in tropical glacier extents therefore provides a window into past temperature fluctuations in the low latitudes. My dissertation research focuses upon establishing a chronology of past glacial fluctuations in the equatorial Rwenzori Mountains of Uganda. The results presented here yield insight into the timing, magnitude, and potential drivers of past glacier - and thus temperature - changes in the low latitudes during and since the last ice age.

1.2. Background

1.2.1. The Rwenzori Mountains: Setting and Climate

The Rwenzori Mountains (0.3°N, 30°E), located on the border between Uganda and the Democratic Republic of Congo, are an uplifted horst of basement rock on the western margin of the East African Rift system (Figure 1.1). The highest peak in the Rwenzori, Mt. Stanley, is 5109 m asl and stands roughly 360 m above the modern freezing level (~4750 m asl; Lentini et al., 2011). Evergreen afro-alpine and montane vegetation dominate within the Rwenzori, although there is a distinct altitudinal zonation in vegetation (Foster, 2001). Above ~4000 m asl vegetation is sparse, although mosses and lichens are common on exposed bedrock surfaces (Bauer et al., 2010).

Eastern tropical Africa is relatively arid compared with other regions in the humid inner tropics, a result of the high elevation of the East African Rift Zone and persistently cool sea-surface temperatures in the western Indian Ocean (Yang et al., 2015). In

contrast, the slopes of the Rwenzori receive ~2.0-2.7 m of precipitation each year and have $\geq 90\%$ humidity year round, with two distinct rainy seasons in the boreal spring and fall as the Intertropical Convergence Zone (ITCZ) passes overhead (Osmaston, 1989; Lentini et al., 2011). Because the Rwenzori occur on the western edge of the East African Rift zone, they are influenced by air masses sourced from the east and west. The Congo Air Boundary (CAB) marks the transition where moist Atlantic air meets relatively dry air sourced from the Indian Ocean or Horn of Africa (Singarayer et al., 2015)(Figure 1.2). The Rwenzori are located to the west of the CAB during boreal winter and are under stronger influence from Atlantic air masses during this time. During the boreal spring, summer, and fall, the Rwenzori are generally located east of the CAB and are under greater influence from Indian Ocean or continental African air masses during this time.

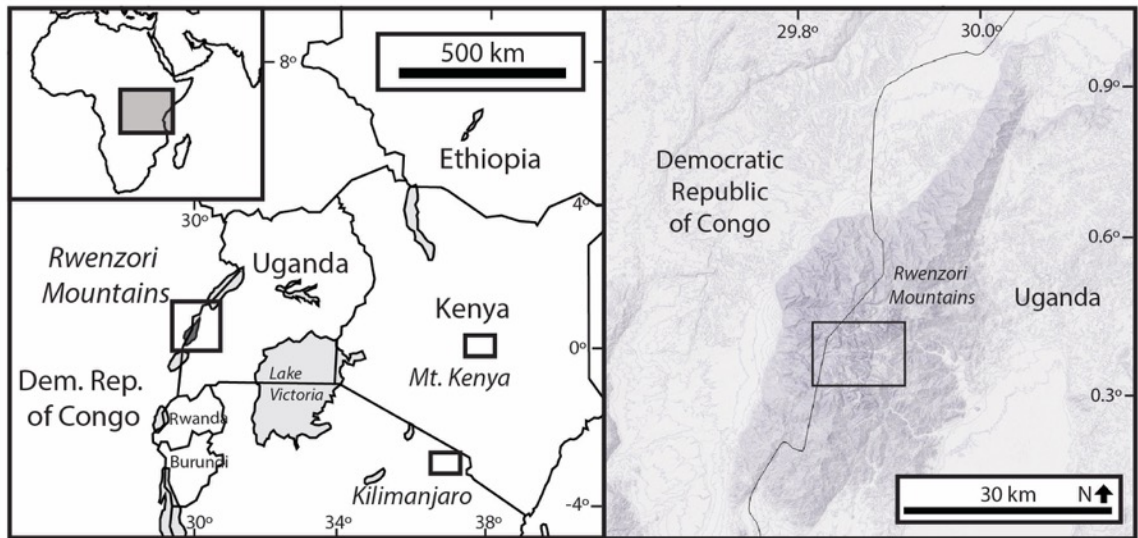


Figure 1.1. East Africa and the Rwenzori Mountains. The Rwenzori Mountains are one of three still-glaciated (boxed) regions in East Africa (left). The Rwenzori Mountains (right) occur on the border between Uganda and the Democratic Republic of Congo, and are the most extensive alpine glacier environment in Africa. The black box outlines the area shown in Figure 1.4. The contour map of the Rwenzori is based upon a 30-m DEM of the Rwenzori region and constructed using QGIS.

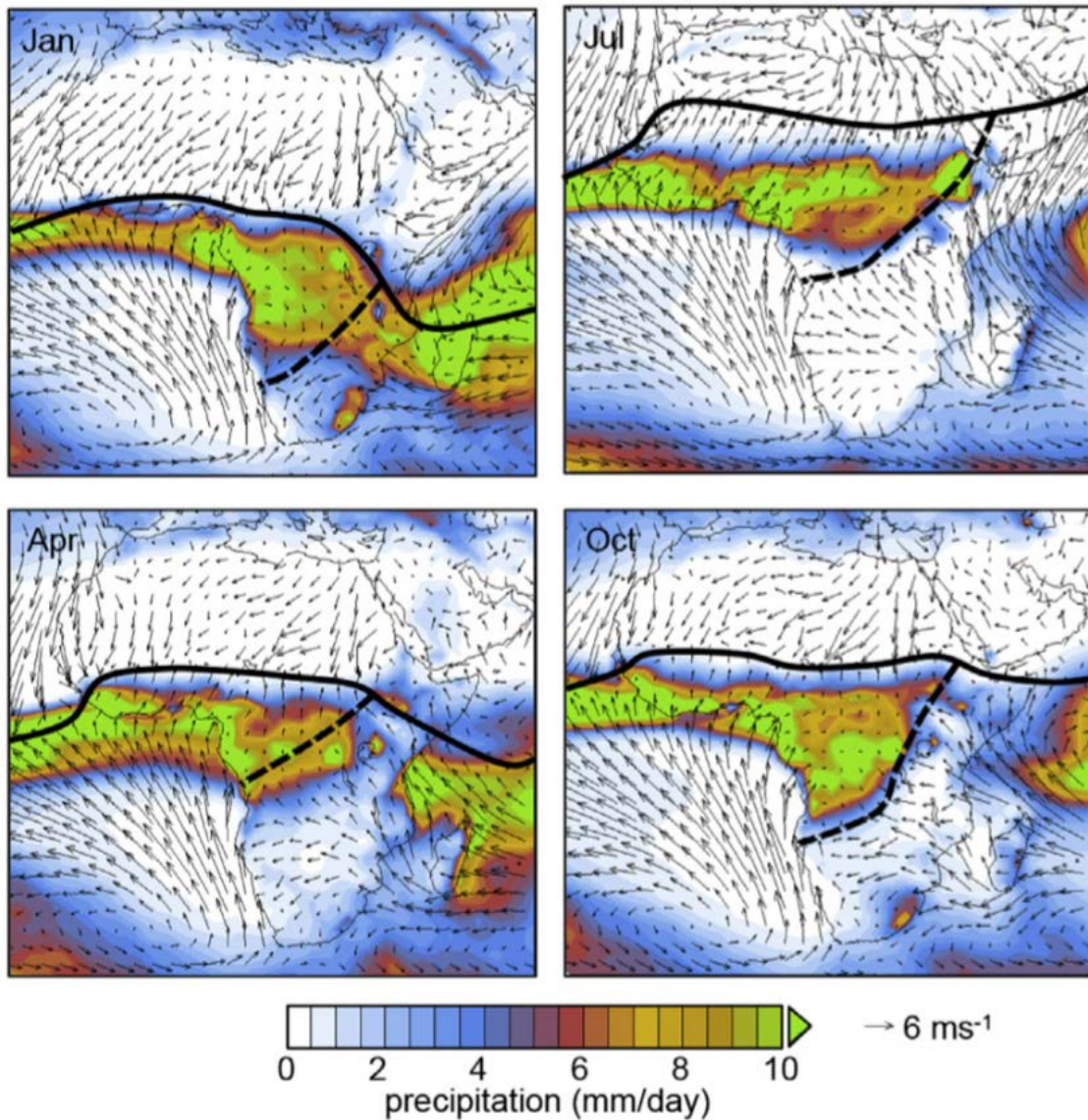


Figure 1.2. Monthly mean precipitation in mm/day and 10 m asl winds. The solid black line marks the mean position of the ITCZ, and the dashed black line indicates the CAB. Data are from ERA Interim reanalysis (1979-2013). Image modified from Singarayer et al. (2015).

1.2.2. Glaciation in the Rwenzori Mountains

The first recorded observations of glacial extents in the Rwenzori are from an Italian research expedition led by the Duke of Abruzzi in 1906 (Abruzzi, 1907). Since these initial measurements, Rwenzori glaciers have shrunk from a total estimated area of ~6.5 km² in 1906 CE to ~0.96 km² in 2003 CE (Kaser and Noggler, 1996; Taylor et al., 2006). The glaciers lost ~50% of their areal extent between 1987 CE and 2003 CE (Taylor et al., 2006). The recent snowline elevation is estimated to be ~4750 m asl (Lentini et al., 2011), a rise of roughly ~150 m since 1955 CE (Osmaston, 1989; Kaser and Osmaston, 2002). Today glaciers in the Rwenzori persist only above ~4400 m asl on the slopes of Mt. Stanley, Mt. Baker, and Mt. Speke (Figure 1.3; 1.4). Should recession continue at its current rate, remaining glaciers are predicted to melt away entirely within the next two decades (Taylor et al., 2006).

Osmaston (1965) conducted extensive glacial-geomorphic mapping in the Rwenzori in an effort to identify and establish relative age control on past glaciation events. Osmaston (1965; 1989) classified glacial moraines into five distinct stages based upon their size, morphology, and relative degree of preservation and weathering. These stages include, from oldest to youngest, the Katabarua, Rwimi, Lake Mahoma, Omurubaho, and Lac Gris stages. The earliest of the stages, the Katabarua and Rwimi, likely pre-date the Last Glacial Maximum (~26.5-19.0 ka; LGM; Clark et al., 2009) and represent the most extensive preserved glacial extents in the Rwenzori. The Lake Mahoma stage moraines are characterized by high-relief (30-100 m) ridges that extend as low as ~2000 m asl. Most Lake Mahoma stage moraines are lateral moraines; terminal moraines of this stage are rarely preserved. Omurubaho stage moraines occur at

elevations ~3600-4000 m asl, are 3-30 m in relief, and are stratigraphically inboard of Lake Mahoma stage deposits. Omurubaho moraines often feature terminal ridges in addition to lateral moraines. Lac Gris stage moraines are inboard of Omurubaho deposits and indicate presumed near-historical ice margin positions. Lac Gris moraines are within ~90-100 m of recorded 1906 CE glacier extents and are generally low (≤ 1 m) relief features, although certain Lac Gris moraines rise ~3-5 m above the valley floor.



Figure 1.3. The Rwenzori high peaks on a clear day. Glaciers persist on the slopes of Mt. Stanley, Mt. Speke, and Mt. Baker, but are projected to disappear within the coming decades. This photo was taken from the peak of Mt. Weisman in January 2015 (see Figure 1.3 for map view of this area). View is to the north.

Until recently, the only numerical age control on Rwenzori glaciation came from a few radiocarbon ages of lake sediment (Livingstone, 1962; 1967) and lichenometric estimates on Lac Gris stage moraines (Bergström, 1955). Livingstone (1962) reported a radiocarbon age of ~17.5 ka from moraine-dammed Lake Mahoma (~3000 m asl; Figure

1.3). The radiocarbon age is a bulk age from the lowermost 20 cm of organic sediments which overlie a horizon of inorganic silt at the base of the 6 m long sediment core (Livingstone, 1962). The age provides a minimum-limiting age on deglaciation from the Lake Mahoma stage moraines in the Mubuku valley. In the Butahu valley, a bulk age from the lowermost collected layer of organic sediments in a core from Upper Lake Kitandara (~4000 m asl; Figure 1.3) yield a radiocarbon age of ~7.7 ka (Livingstone, 1967). It is important to note that unlike Lake Mahoma, upper Lake Kitandara is not moraine dammed. In addition, Livingstone (1967) notes that this age come only from the lowermost horizon of organics retrieved from the lake, and does not interpret the age as necessarily representing the contact between organic and glacial clastic sedimentation. Nonetheless, this age provides a minimum-limiting age constraint on deglaciation of the valley. Bergström (1955) used lichenometry to estimate that Lac Gris moraines near the margin of Elena Glacier on Mt. Stanley date to ~1750 CE. However, the rate at which lichen colonizes rock surfaces in the Rwenzori is unconstrained (Osmaston, 1989). More recently, cosmogenic beryllium-10 (^{10}Be) surface-exposure dating has been used to date Rwenzori glacial deposits directly. Eight ^{10}Be ages of boulders on the crests of two Lake Mahoma stage moraines in the Mubuku valley indicate that moraine deposition occurred at ~21.5 and ~24.9 ka, during the LGM (Kelly et al., 2014).

1.2.3. Controls on Tropical Glaciation

The tropics are defined geographically as the region between 23°N and 23°S latitudes, where the sun passes directly overhead at least once per year. Kaser and Osmaston (2002) suggest that the tropics are defined best climatologically as the region

in which diurnal temperature variations are greater than corresponding annual (seasonal) changes in temperature (Figure 1.5). Within this framework the tropics can be further broken into two regimes: the humid ‘inner’ tropics and the more arid ‘outer’ tropics (Kaser and Osmaston, 2002). The inner tropics comprise the area from $\sim 10^{\circ}\text{N}$ to 10°S latitude (although this extent varies between ocean-influenced and more continental regions) which receive significant rainfall throughout the year. In contrast, the outer tropics have more clearly defined wet and dry seasons dictated primarily by the position of the ITCZ and seasonal monsoon rainfall.

Mid-latitude glacier extents are a robust proxy for summer temperatures (Oerlemans, 2005; Anderson and Mackintosh, 2006). In contrast, seasonality in the tropics is marked by changes in precipitation rather than temperature. Due to the lack of seasonal temperature changes in the tropics, some argue that alterations in hydroclimate conditions (i.e., precipitation, humidity, and cloudiness) are the primary controls on tropical glacier extents (Mölg et al., 2003). Although hydroclimate conditions assuredly impact tropical glacier mass balance the degree to which these factors influence individual glaciers over time remains uncertain, particularly in East Africa where there are few numerically dated records of past glaciation (Mölg, 2003; 2006; Kaser and Osmaston, 2002; Taylor et al., 2006).

Lake-level records from Lake Victoria are interpreted as a proxy for East African precipitation amounts (Nicholson and Yin, 2001). Mölg et al. (2003, 2006) use these lake-level data to suggest that a sharp decline in precipitation inferred at ~ 1880 CE occurred concurrently with the recession of regional glaciers. In contrast, Taylor et al. (2006) use aerial and satellite imagery of Rwenzori glaciers to argue that ongoing glacier recession is

primarily driven by rising temperature. Although there is a marked precipitation gradient across the Rwenzori (Osmaston, 1989), changes in the surface area of glaciers are uniform across the Rwenzori since at least 1955 CE with no indication of precipitation gradients on changing glacial extent (Taylor et al., 2006). More recently, sediment records collected from glacially influenced Rwenzori lakes indicate that glacier recession was underway by at least 1870 CE, prior to the lowering of Lake Victoria and coincident with rising air temperature (Russell et al., 2009).

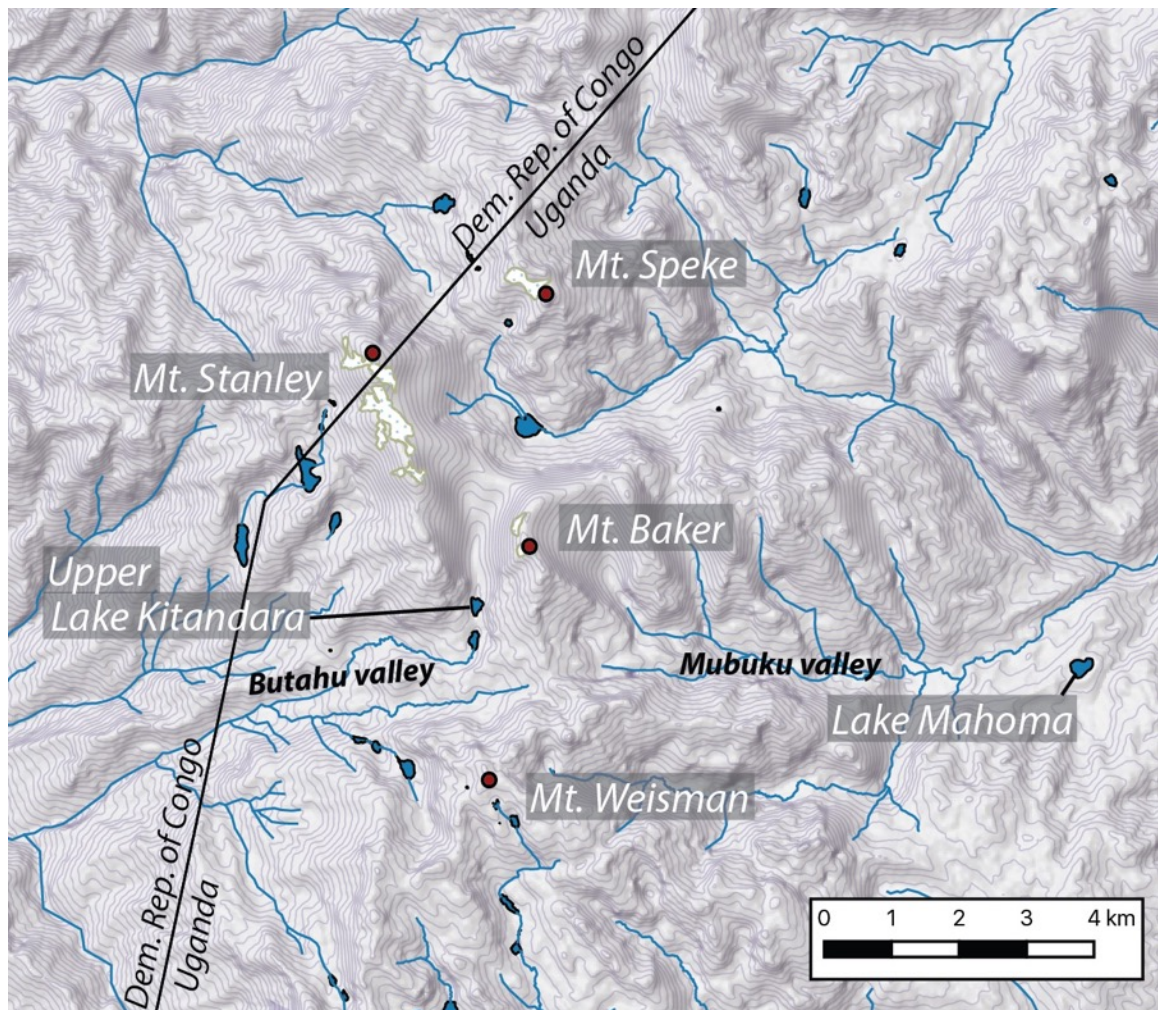


Figure 1.4. Contour map of the high peaks of the Rwenzori Mountains. Today Mt. Stanley, Mt. Speke, and Mt. Baker all feature active glaciers (white and blue stipple). Limiting radiocarbon ages from Lake Mahoma and Upper Lake Kitandara until recently provided the only numerical age control on past Rwenzori glacier fluctuations. North is toward the top of the image.

Studies of glacier mass balance in other tropical regions yield a more detailed picture of the primary controls on low-latitude glacial extent. Sagredo and Lowell (2012) used both cluster and principal component analysis to evaluate the climatology of 234 glaciers along the spine of the South American Andes. Their results defined seven unique climate zones in which Andean glaciers persist and suggest that a clear delineation of the climate regime in which a given glacier occurs is essential to determining the dominant control on both past and present glacier extents. Their results also suggest that in humid regions, where glaciers are never ‘starved’ for precipitation, temperature is the primary limiting factor on glacial extent. In contrast, glaciers in arid regions are precipitation-limited systems, and may respond more sensitively to changes in hydroclimate than temperature. Thus a glacier located in the more humid inner tropics may be expected to respond more sensitively to a change in temperature than a glacier in the more arid outer tropics. These results are supported by modeling studies that similarly suggest a dominant temperature control on glaciers in humid regions (Rupper and Roe, 2008; Rupper et al., 2009; Sagredo et al., 2014).

Studies of past tropical glacial extents also suggest that temperature was a dominant control on glacier size. Jomelli et al. (2014) compiled cosmogenic-nuclide surface exposure-age based moraine chronologies from sites in the tropical Andes both north and south of the equator ($\sim 6^{\circ}\text{N}$ - 17°S). These results indicated a broad synchrony of glacier fluctuations during deglaciation, a period when precipitation patterns in the northern and southern Andes were out of phase. The apparent synchrony of regional glacial fluctuations therefore suggests that temperature was the primary driver of glacial fluctuations in the tropical Andes (Jomelli et al., 2014; 2017). Similarly, Stroup et al.

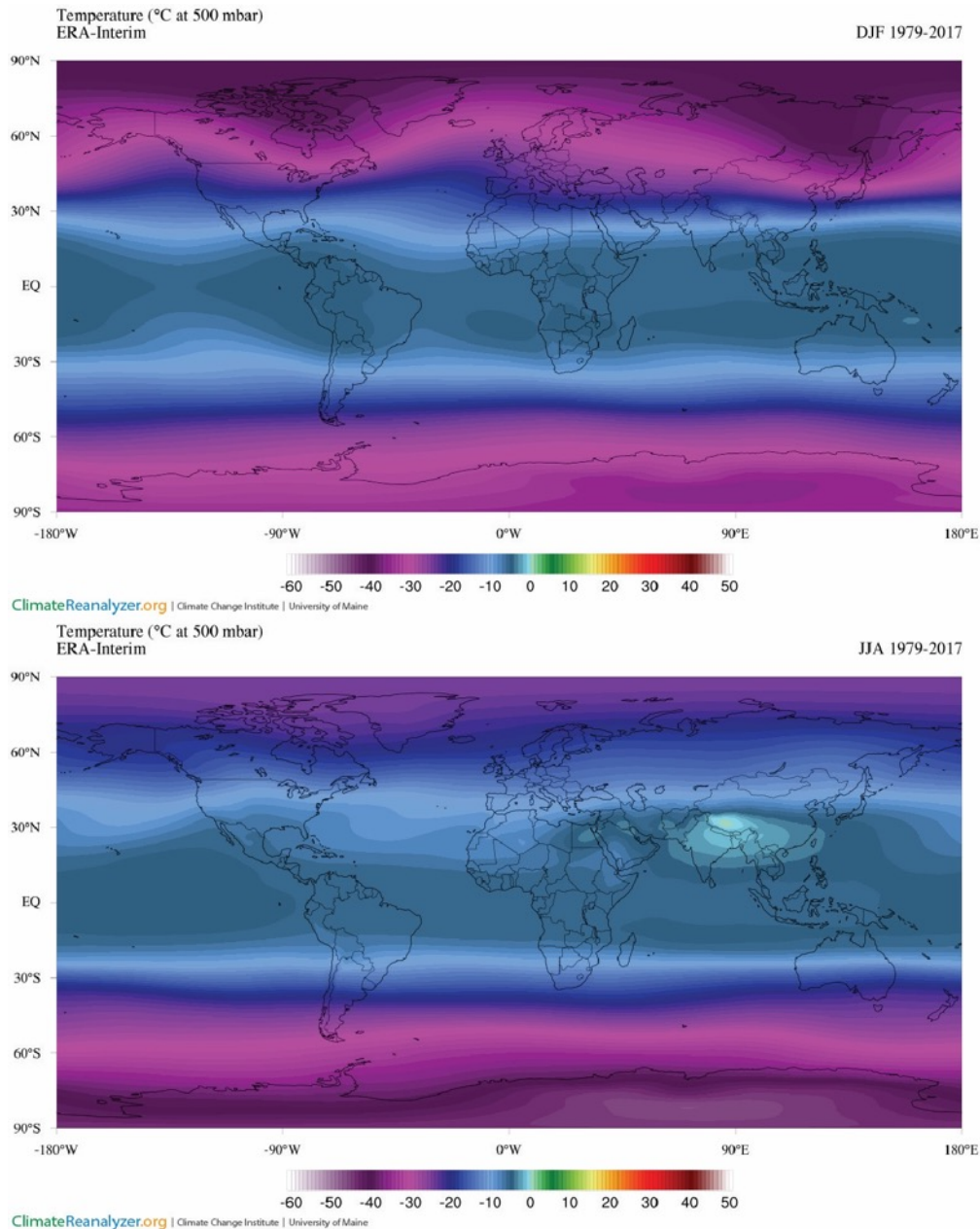


Figure 1.5. ERA-Interim temperatures (C°) at 500 mb, or roughly 5000 m asl, where many tropical glaciers persist, averaged between 1979 and 2017 CE. The upper plot shows temperature during the boreal winter (DJF) months, and the lower plot shows boreal summer (JJA) temperatures. In contrast to the spatial and temporal variability in the low latitudes over time, temperatures in the high-elevation tropics are more constant and uniform. Image from the CCI Climate Reanalyzer [climatereanalyzer.org].

(2014) document late-Holocene glacial recession at Quelccaya Ice Cap during the period of highest accumulation in the Quelccaya ice core. The authors thus suggest that temperature was the dominant influence on glacial extent. The results of Jomelli et al. (2014; 2017) and Stroup et al. (2014) suggest that glaciers in both the ‘inner’ and portions of the ‘outer’ Andean tropics responded primarily to temperature during the last deglaciation and Holocene Epoch. These results are supported by modeling of Peruvian glaciers at ~13°S which shows the dominance of temperature on past deglacial and Holocene glacial extents (Malone et al., 2015).

As mentioned above, the Rwenzori are located in the inner tropics and receive ~2.5 m annual precipitation (Osmaston, 1989; Lentini et al., 2011). ¹⁰Be surface-exposure ages of Lake Mahoma stage moraines indicate extensive Rwenzori glaciation during the LGM when regional precipitation rates were relatively low (Kelly et al., 2014). In addition, Russell et al. (2009) suggest that the onset of glacier recession from the historical maxima was underway during a period of wet and warming conditions. Based upon these data, I hypothesize that Rwenzori glaciers have responded primarily to changes in temperature both during and since the LGM.

1.3. Research Objectives and Dissertation Structure

1.3.1. Objectives

Tropical glaciers provide a unique and valuable proxy for terrestrial low-latitude climate conditions over the last glacial cycle. In tropical South America, cosmogenic-nuclide surface-exposure dating of glacial deposits has yielded information regarding the timing and magnitude of past climate shifts, revealing a regional coherence in

temperature change since the LGM (e.g., Jomelli et al., 2014; Mark et al., 2017). In the humid tropics, Andean glaciers appear to have retreated rapidly following the LGM. Between ~16 and 11 ka, glacier retreat slowed yet was punctuated by periods of readvance or stillstand at ~16, ~14, and ~12-11 ka (Jomelli et al., 2014; Bromley et al., 2016; Stansell et al., 2015; 2017). Glaciers in the tropical Andes then retreated rapidly during the early Holocene to near or inboard of their late-Holocene or near-historical maxima (Stansell et al., 2015; 2017; Mark et al., 2017). That glaciers across the region fluctuated similarly throughout the period ~20 ka to present suggests that these systems responded primarily to changes in temperature rather than to precipitation, since precipitation changes varied distinctly across the region (Thompson et al., 2006; Jomelli et al., 2014; Bromley et al., 2016; Novello et al., 2017).

The Rwenzori Mountains are an ideal site for investigating past low-latitude glacial fluctuations outside the Andes. Rwenzori glacial deposits range in age from estimated pre-LGM to historical and, unlike the volcanic terrains of Mt. Kenya and Kilimanjaro, the Rwenzori are underlain primarily by quartz-rich lithologies (McConnell, 1959). These quartz-bearing rocks enable surface-exposure dating using the cosmogenic nuclide ^{10}Be (hereinafter ^{10}Be dating; Gosse and Phillips, 2001). The Rwenzori therefore offer the unique opportunity in tropical Africa to apply ^{10}Be dating to glacial deposits. The primary objectives of my research are to:

1. Determine the timing and magnitude of glacial fluctuations in the Rwenzori during and since the LGM.
2. Establish whether changes in Rwenzori glacial extents are primarily influenced by temperature and, therefore, are useful as paleotemperature proxies.

3. Compare the timing of Rwenzori glacial fluctuations with glacial fluctuations elsewhere in the tropics to investigate whether there is a pan-tropical coherence of glacier/temperature change during and since the LGM.
4. Compare the timing of Rwenzori and wider tropical glacial fluctuations with other records of past temperature and climate in order to investigate potential forcing mechanisms of climate changes in the low latitudes.

1.3.2. Dissertation Structure

This dissertation is comprised of six chapters, including an introduction (Chapter 1), a detailed description of the methods used (Chapter 2), three scientific papers (Chapters 3, 4, and 5), and a final chapter that includes a summary of major findings and suggestions for future work (Chapter 6). The three scientific papers are in their current *in review* (Chapter 3) or *in preparation* (Chapters 4 and 5) versions. The only modifications made to these papers are those needed to comply with the Dartmouth College dissertation requirements. These modifications include the combination of all references into a single complete list (presented after the summary Chapter 6), and the use of in-text citation throughout the dissertation. However, the format and length of each paper varies based upon the submission standards for each target journal. I briefly describe each chapter below.

1. *Introduction.* The tropics are a key component of the global climate system, yet there are few records of past tropical temperatures that can be used to contextualize observed modern climate changes. Tropical glaciers offer a useful vantage on past climate in the low latitudes. Here I describe why and briefly how I

use past glacial extents in the Rwenzori Mountains of Uganda as a proxy for past temperature changes.

2. *Methods.* I used careful glacial-geomorphic mapping and ^{10}Be dating to identify, contextualize, and date glacial deposits in the Rwenzori Mountains. Here I describe these methods in detail.
3. *High-latitude warming initiated the onset of the last deglaciation in the tropics.* At the end of the last ice age, global temperatures warmed in step with the onset of rising atmospheric CO_2 . Yet there is evidence that deglacial warming began ‘early’ in the low latitudes, which may require the invocation of additional mechanisms to initiate this apparent tropical and, perhaps, global warming. This chapter explores the onset of deglaciation at the end of the LGM in the Rwenzori Mountains as well as in tropical South America (Jackson et al., submitted and in review at *Science Advances*).
4. *Millennial-scale glacial fluctuations in tropical Africa during the last deglaciation.* The last deglaciation was marked by abrupt, millennial-scale climate events. While rooted in the high-latitudes, the imprint of these shifts are recognized far beyond the poles. Due to a paucity of temperature records, the effects of these events within the tropics remain enigmatic. This chapter documents Rwenzori glacial fluctuations throughout the late-glacial period, and compares these with similar records from the tropical Andes to assess the pan-tropical signal of late-glacial climate change (Jackson et al., in prep. For submission to *Quaternary Science Reviews*).

5. *Holocene glaciation in the African tropics.* Africa's tropical glaciers are retreating rapidly as the world warms and are projected to disappear entirely within the next century. However, there is some evidence that East African glaciers persisted throughout the Holocene. This includes the early middle Holocene, when temperatures were as warm as or warmer than today. This chapter explores the persistence, or lack thereof, of tropical African glaciers during Holocene time (Jackson et al., in prep. For submission to *Journal of Quaternary Science*).
6. *Discussion.* Here I synthesize the research presented, offer broad conclusions, and highlight opportunities for future research.

1.4. Author Contribution Statement

Three chapters within this thesis (Chapters 3-5) are prepared as manuscripts for journal submission and include the work and input of multiple co-authors. Here I highlight the roles and contributions of all co-authors.

Chapter 1: M.S. Jackson collected and processes samples, created all figures, analyzed results, and wrote the paper. M.A. Kelly, J.M. Russell, and A.M. Doughty collected samples, analyzed results, co-wrote and edited the paper and figures. J.A. Howley and S.H. Zimmerman processed samples for analysis at Dartmouth College and at Lawrence Livermore national Laboratory, respectively. D. Cavagnaro collected and processed samples for analysis at Dartmouth College. J.W. Chipman and S.H. Zimmerman edited the paper and figures. M.A. Kelly, J.M. Russell, and B. Nakileza conceptualized the project. B. Nakileza coordinated the project within Uganda.

Chapter 2: M.S. Jackson collected and processes samples, created all figures, analyzed results, and wrote the paper. M.A. Kelly, J.M. Russell, and A.M. Doughty collected samples, analyzed results, co-wrote and edited the paper and figures. J.A. Howley and S.H. Zimmerman processed samples for analysis at Dartmouth College and at Lawrence Livermore national Laboratory, respectively. M.B. Baber and D. Cavagnaro collected and processed samples for analysis at Dartmouth College. J.W. Chipman and S.H. Zimmerman edited the paper and figures. M.A. Kelly, J.M. Russell, and B. Nakileza conceptualized the project. B. Nakileza coordinated the project within Uganda.

Chapter 3: M.S. Jackson collected and processes samples, created all figures, analyzed results, and wrote the paper. M.A. Kelly, J.M. Russell, and A.M. Doughty collected samples, analyzed results, co-wrote and edited the paper and figures. J.A. Howley and S.H. Zimmerman processed samples for analysis at Dartmouth College and at Lawrence Livermore national Laboratory, respectively. J.W. Chipman and S.H. Zimmerman edited the paper and figures. M.A. Kelly, J.M. Russell, and B. Nakileza conceptualized the project. B. Nakileza coordinated the project within Uganda.

CHAPTER 2

METHODS

2. Introduction

The results of the research presented in this dissertation are predicated upon two primary methods: glacial-geomorphic mapping and surface-exposure dating using the cosmogenic nuclide Beryllium 10 (^{10}Be). Through detailed mapping, I identified, classified, and contextualized glacial deposits in the Rwenzori Mountains. These observations aided in identifying target landforms for cosmogenic-nuclide surface-exposure dating, the method by which I determined numerical ages of glacial deposits in the Rwenzori. This chapter details the field and laboratory techniques I used to assess the timing of past glacial fluctuations in the Rwenzori, as well as the methods I used to compare the Rwenzori glacial chronology with cosmogenic-nuclide surface-exposure ages from elsewhere around the globe.

2.1. Glacial-Geomorphic Mapping

Prior to going into the field, I identified and classified glacial-geomorphic features in the Rwenzori Mountains using panchromatic WorldView-1 half-meter resolution satellite imagery. These preliminary maps enabled the identification and prioritization of target landforms for ^{10}Be dating (below) and were essential resources while in the field. I ground truthed and expanded upon these preliminary maps once in the field, noting the morphology and relative weathering characteristics of glacial and other sedimentary deposits. I later used these collected observations to finalize interpretations and to draft detailed glacial-geomorphic maps of sampled field sites. I produced geomorphic maps for

all of the valleys in which I worked. The completed maps are drawn onto a 30-m resolution digital-elevation-model (DEM) contour map of the Rwenzori (Chapters 3 and 4) or onto WorldView-1 satellite imagery (Chapter 5). I drafted all maps in QGIS version 3.

2.2. Cosmogenic-Nuclide Surface-Exposure Dating

2.2.1. Cosmogenic-Nuclide Production and Theory

Cosmogenic-nuclide surface-exposure dating has rapidly become a primary tool in glacial geochronology and glacial-geologic research (e.g., Dunai, 2010). The method allows for the direct dating of glacial deposits and so allows numerical age constraints to be placed on past glacial fluctuations. *In-situ* cosmogenic ^{10}Be (hereinafter ^{10}Be) is one of the most common nuclides targeted for use in determining surface-exposure age chronologies, as it is applicable in a wide variety of sites and settings and its production pathway is relatively simple and well known (Dunai, 2010). ^{10}Be is produced primarily through spallation reactions between incoming cosmic rays to Earth surface and oxygen atoms within molecules of quartz (Lal, 1991), although muonic production accounts for ~3.6% of total ^{10}Be in and near a rock surface (Heisinger et al., 2002). The production rate of ^{10}Be is controlled by properties of the sample such as rock density (Dunne et al., 1999), attenuation of the incoming cosmic ray flux by the atmosphere (expressed as elevation/air pressure; Dunai, 2010), and geomagnetic latitude, as the Earth's magnetic field deflects incoming cosmic rays and the effects of this deflection vary over Earth's surface (Dorman et al., 1999; Smart et al., 2000). Additional factors such as surface cover

by snow (Zweck et al., 2013) or vegetation (e.g., Balco et al., 2009) also may affect nuclide production.

Local or regional ^{10}Be production rates are constrained at a number of sites at various latitudes and elevations (e.g., Borchers et al., 2016), however many are from northern middle latitudes and relatively low elevations (<2000 m asl). These calibrations are determined by measuring nuclide concentrations within rock surfaces for which independent age control exists, for example, via radiocarbon dating (e.g., Goehring et al., 2010; Putnam et al., 2010).

The ^{10}Be production rate in a given rock surface is affected by local factors such as rock density and sample thickness, as well as shielding of incoming cosmic rays by surrounding topography. The rate of attenuation of incoming cosmic rays with depth in a rock surface increases with rock density (Dunai, 2010). Relatedly, because more nuclides are produced nearer the rock surface than at depth, the thickness of a sample affects the expected profile of nuclide accumulation. Shielding of incoming cosmic rays by topography reduces the net flux of incoming cosmic rays to the rock surface (Gosse and Phillips, 2001; Dunai, 2010). The potential impact of topographic shielding is determined when a sample is collected by measuring the angle to the surrounding horizon in all directions (360°). Calculated local ^{10}Be production rates may then be ‘scaled’ to other sites around the globe by adjusting for altered elevation (atmospheric thickness) and geomagnetic latitude.

Of the variables that may impact the ^{10}Be production rate at a given site, the effect of changing geomagnetic latitude (dipole moment) is the least well constrained (e.g., Dunai, 2010). This is particularly true in the tropics, where the predicted impacts of

geomagnetic latitude are much stronger than at middle- or high-latitude sites (Kurz et al., 1990; Clark et al., 1995; Licciardi et al., 1999; Lifton, 2016). Scaling frameworks generally predict a three-fold increase in the rate of nuclide production when moving from sea level to 1500 m elevation, and a doubling in production at sea level when moving from the equator to the poles (Balco et al., 2008). However there is yet no standardized method for adjusting for magnetic field changes over time and space. Certain ‘time-variant’ scaling frameworks account for changing magnetic field strength over time using paleomagnetic (“Lm” scaling; Lal, 1991; Stone, 2000; Balco et al., 2008) or cosmic ray flux models (“LSDn” scaling; Lifton et al., 2014). Alternatively, ‘time-invariant’ scaling frameworks hold the strength and orientation of the magnetic field as constant (“St” scaling; Lal, 1991; Stone, 2000).

One assumption made for ^{10}Be dating is that there was no ^{10}Be present in the rock surface prior to the most recent period of exposure (Gosse and Phillips, 2001). Such pre-existing ^{10}Be is commonly known as “inherited ^{10}Be ”. In regions with active, wet-based glaciers, glacially transported clasts are typically abraded during entrainment and transport and any pre-existing ^{10}Be is removed. However, where glaciers are non-erosive at their beds or where rockfall on glacier surfaces is transported supraglacially some inherited ^{10}Be may be present in the surfaces of rocks deposited at the glacier margin. In addition, samples buried for some period by soil or rockfall may still accumulate ^{10}Be through muogenic production at depth (Dunai, 2010). This inherited ^{10}Be increases the total nuclide concentration in the sample, resulting in an ‘apparently old’ ^{10}Be age.

In contrast, cover by snow, sediment, or vegetation may reduce the flux of incoming high-energy particles to a rock surface, thereby resulting in a lower ^{10}Be

concentration in the rock surface than would be expected for the actual age of the sample. In this case, a sample would have an “apparently young” ^{10}Be age (Balco et al., 2008; Dunai, 2010). Erosion of a rock surface would also cause an apparently young ^{10}Be age, as the upper rock surface with the highest ^{10}Be concentration is removed, resulting in a lower ^{10}Be concentration (Gosse and Philips, 2001). In all cases, it is best to assess the potential impacts of pre- and post-depositional processes on measured nuclide concentrations with careful field observations. In addition, prioritizing tall (≥ 1 m) boulders tends to yield more uniformly distributed age populations than more shorter boulders or cobbles (Heyman et al., 2016), although in certain settings boulders and cobbles or pebbles on moraine crests yield similar ages (Briner, 2009).

2.2.2. Sampling for ^{10}Be Dating

Over the course of three field seasons (January, 2015; June, 2016; June, 2018) in the Rwenzori I collected samples from boulders on the crests of moraine ridges as well as from perched boulders set down on bedrock and glacially abraded bedrock surfaces. While in the field I prioritized sampling tall (≥ 1 m) boulders on the crests of moraines that showed little or no indication of post-depositional modification or movement. I collected samples from the uppermost ~ 5 cm of boulder surfaces using a hammer and chisel or the drill-and-blast method of Kelly (2003). In order to determine the shielding of incoming cosmic rays by the surrounding topography, I measured the angle to the horizon in 30° compass quadrants using a handheld compass and clinometer. Where low clouds precluded the determination of topographic shielding in the field I later estimated shielding values using a 30-m DEM of the Rwenzori. To check for accuracy, I compared

additional DEM-based shielding results with similar field-based shielding estimates. The DEM method yielded estimates similar to (within ~0-1% of) those based upon field measurements. I also used a handheld compass to measure the surface dip and dip direction of each sample prior to collection. Wherever possible I collected samples from flat rock surfaces in order to minimize potential uncertainties with topographic shielding corrections. I recorded the geographic position of each sample using a handheld GPS unit. Each measurement is the 'average' position recorded by the GPS unit over the course of two to five minutes, sufficient time to obtain ≥ 100 individual measurements. The final reported sample locations are accurate to within ± 3 m in the vertical plane (i.e., latitude and longitude) and ± 1 m in the horizontal plane (i.e., elevation).

2.2.3. Laboratory Methodology

I measured the thickness of each sample to the nearest millimeter (± 1 mm) using analog hand calipers. I constructed a 1 cm x 1 cm grid on each sample surface and measured the sample thickness at each gridpoint. I averaged these measurements to obtain an arithmetic mean sample thickness for use in determining the subsequent surface exposure age. I also documented the lithology of each sample and made note of any unique sample characteristics (quartz veins, mineralogy, surface weathering, etc.). Once measured and described, I crushed, ground, and sieved samples to obtain the 210-750 μm grain size. After rinsing away remaining fine grains and dust using de-ionized water I boiled ~115 g of crushed sample fraction in o-phosphoric acid (H_3PO_4) followed by sodium hydroxide (NaOH). These boils removed any remaining organics within the sample and also removed certain micaceous minerals from the bulk sample fraction.

After rinsing each sample with MQ-H₂O I leached each sample 2-3 times in a 5% hydrofluoric/nitric acid (HF, HNO₃) solution, rinsing samples thoroughly with MQ-H₂O between each leach. These HF/HNO₃ leaches are used to dissolve away non-silicate minerals and to etch the remaining quartz grains to remove any potential surficial (meteoric-sourced) ¹⁰Be. Afterwards I used a 1% HF/HNO₃ leach to continue the etching process, followed by heavy liquid separation to isolate quartz from the bulk sample fraction. This step was followed by 2-4 more 1% HF/HNO₃ leaches in order to continue etching the remaining quartz grains. For certain samples I used a Frantz mineral separator to magnetically separate magnetic and non-magnetic (e.g., quartz) grains from the bulk fraction. Both heavy liquids and magnetic separation were always followed by at least one additional 1% HF/HNO₃ leach to remove any potential ¹⁰Be contamination.

After obtaining clean quartz I continued the methodology for isolating beryllium with batches of samples that typically consisted of ~5-8 samples. With each batch I included a process blank that contained no sample. I spiked all samples and the process blank with a known mass of ⁹Be carrier and digested each in concentrate HF. The carrier used is a ⁹Be carrier developed at Dartmouth from a deeply buried beryl crystal. I then used a modified version of the procedures described in Schaefer et al. (2009) to isolate beryllium from each sample and the process blank. ¹⁰Be/⁹Be ratios of samples were measured at the Center for Accelerator Mass Spectrometry at Lawrence Livermore National Laboratory and normalized to the 07KNST3110 standard (Nishiizumi et al., 2007). I subtracted the ¹⁰Be/⁹Be process blank ratio from the ¹⁰Be/⁹Be ratios of measured samples and used the blank-corrected sample ratios to determine the concentration of ¹⁰Be in each sample per gram of quartz.

2.2.4. Exposure Age Calculation

I calculated ^{10}Be ages for all Rwenzori samples using the version 3 of the online calculator as described by Balco et al. (2008 and subsequently updated) with a high-altitude, low-latitude ^{10}Be production rate (Kelly et al., 2015) and time-invariant (“St”) scaling (Lal, 1991; Stone, 2000). Local ^{10}Be production-rate calibrations from high-elevation sites in the South American tropics yield the most robust results (lowest uncertainty by total scatter; Balco et al., 2008 and subsequently updated) when paired with time-independent scaling (Blard et al., 2013; Kelly et al., 2015), which suggests that this scaling method may be most appropriate for sites such as the Rwenzori. These calibrations employ glacial deposits that date to ~13-11 ka and so are particularly applicable to similarly aged deposits elsewhere (e.g., the late-glacial moraines described in Chapter 4). Assuming that changes in the geomagnetic field influenced the cosmic ray flux both before and after this period, an alternative, time-dependent scaling framework may be more appropriate for samples of Holocene (≤ 11 ka) or glacial (≥ 15 ka) age. For this reason, I also report ^{10}Be ages as calculated using the time-dependent “LSDn” scaling framework (Lifton et al., 2014). Because of the uncertainties in production-rate variability in the low latitudes (Lifton et al., 2016), I choose to base my interpretations on ^{10}Be ages calculated using time-independent (“St”) scaling.

I did not correct Rwenzori ^{10}Be ages for the potential influence of boulder surface erosion. Although many samples showed evidence of surface erosion (e.g., exfoliation, raised quartz veins), ^{10}Be ages obtained from raised quartz veins are indistinguishable from those obtained from boulder surfaces on single moraine ridges. For example, on the Mahoma 4 moraine (Chapter 3) samples RZ-16-49 ($28,650 \pm 570$ yrs) and RZ-16-50

($30,100 \pm 790$ yrs) are from raised quartz veins (1-3 cm above the boulder surface) on gneissic boulders. The other four samples from the Mahoma 4 moraine are from gneissic boulder surfaces and yielded ages between ~ 29.9 and 27.5 ka. The arithmetic mean age of the Mahoma 4 moraine including these quartz-vein samples ($28,960 \pm 1020$ yrs) is statistically indistinguishable from the mean age with these samples excluded ($28,750 \pm 1100$ yrs). Although the final calculated exposure ages may be impacted by erosion effects I suggest that any such impact is negligible.

Similarly, I did not correct the Rwenzori ^{10}Be ages for the potential impacts of cover by snow, soil or vegetation. Snow does not likely persist for a considerable length of time at the elevation of the sample sites due to the intense equatorial solar radiation and warm daytime temperatures. In most cases cover by sediment would be unlikely because the boulders were tall (≥ 1 m) and, therefore, it is unlikely that they were exhumed from within the moraine. Shielding of samples by vegetation, however, may impact the reported ^{10}Be ages from the Rwenzori as most samples were covered by mosses and, in some cases, shrubs and trees.

It is possible to estimate the influence that vegetation cover may have on the ^{10}Be ages by determining the density of the vegetation and estimating the thickness and duration of cover. The average biomass of mosses in the montane forest zone (1500-2500 m asl) in the Rwenzori is $0.004\text{-}0.25$ g/cm² (Pentecost, 1998; Osmaston, 2006). I sampled and measured the density of moss cover from atop a Rwenzori boulder in the montane forest zone and this yielded a dry bulk density of $\sim 0.10\text{-}0.20$ g/cm³. The average density of peat and soil (in varying states of decay and with varying vegetation content) from bogs in the central North America is $\sim 0.15\text{-}0.24$ g/cm³ (Boelter, 1968).

Modeled estimates of the impacts of temperate boreal or rainforest vegetation on the incoming high-energy particle flux suggest a reduction of cosmogenic nuclide production of ~2-7% in areas of dense forest cover (Plug et al., 2007). The majority of this reduction is caused by tree stems, although some comes from shielding by the tree canopy.

Moss cover on sampled Rwenzori boulders ranged between 1 and 15 cm in thickness, although certain samples on the Mahoma moraines (Chapter 3) featured mosses 30-50 cm thick. Based upon the ‘shredded biomass’ model for uniform vegetation cover, mosses and peat of thickness 1-15 cm would require a shielding correction of ~0-3% (Plug et al., 2007; Dunai et al., 2010). However this calculation likely overestimates the impact of such moss cover on cosmogenic nuclide production because the Rwenzori boulders would have had variable moss cover over time. Although ^{10}Be sample locations in the Mubuku and Bujuku valleys currently lie within the montane forest zone and bamboo zone, the timing and pattern of forest succession in these valleys since the Last Glacial Maximum (~26.5-19 ka) unknown. ^{10}Be sample locations in the Nyamugasani valley are currently covered by low (~1-1.5 m tall) shrubs and shielding of these samples by stem biomass is negligible. Moreover, there is no apparent trend in the plot of ^{10}Be ages and thickness of moss/vegetation (Figure 2.1). Due to the uncertainties described above and lack of correlation in the plot, we do not correct the Rwenzori ^{10}Be ages for vegetation cover.

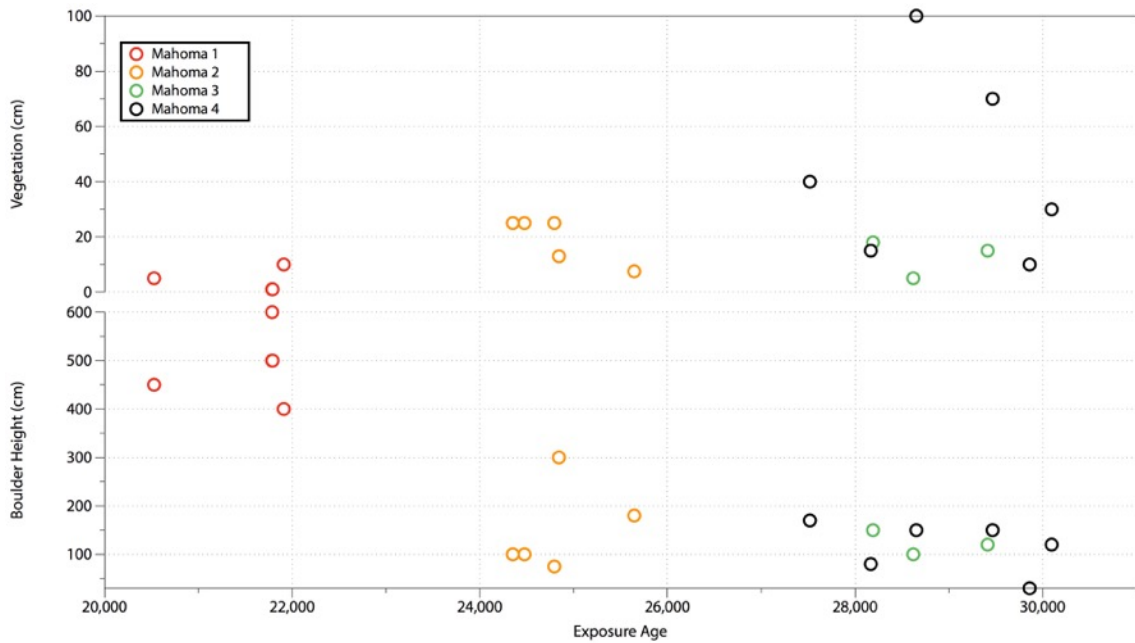


Figure 2.1. Surface-exposure ages from four Rwenzori moraines (Mahoma 1-4) plotted with depth of vegetation cover (in cm; upper) and to show the height (in cm) of each sampled boulder (lower). Each sample age is plotted as a single open circle and color coded by moraine.

2.2.5. Data Interpretation and Recalculation

Although I did not produce new radiocarbon ages as a portion of this project, I reference previously published radiocarbon ages and utilize these data within my larger exploration of past tropical glaciation. I report all radiocarbon ages as calibrated ages in years BP (cal yrs BP). Unless otherwise noted, these ages are as calibrated using the Intcal13 radiocarbon curve (Reimer et al., 2013) and the Calib 7.1 online calculator. Reported ages are the midpoint (with uncertainty) of the returned 2-sigma age range of greatest statistical probability.

Where I discuss ^{10}Be ages from prior work from sites outside the Rwenzori, I recalculated the ^{10}Be ages using version 3 of the online calculator described by Balco et al. (2008 and subsequently updated). I calculated tropical ^{10}Be ages from prior work using the same high-latitude, low-latitude production rate as used for the Rwenzori chronology (i.e., Kelly et al., 2015). For sites in the northern middle latitudes, I used the northeastern North American production rate (Balco et al., 2009), and version 3 of the online calculator described by Balco et al. (2008 and subsequently updated).

Because boulders set down on moraine crests were likely the last sediments deposited before a given moraine was abandoned by a receding glacier, I interpret the ^{10}Be ages obtained from boulders on moraine crests as representing the time of glacial recession from a given moraine position. In contrast, boulders set down on bedrock were likely deposited as ice thinned or retreated past a given location. Samples from bedrock, particularly those from high elevations where glaciers may fluctuate but are thin and potentially not erosive, may contain inherited ^{10}Be accrued over multiple periods of exposure. Therefore ^{10}Be concentrations of bedrock samples may reflect a potentially non-sequential total duration of site exposure.

CHAPTER 3
HIGH-LATITUDE WARMING INITIATED THE ONSET OF THE LAST
DEGLACIATION IN THE TROPICS

Margaret S. Jackson^{1*}, Meredith A. Kelly¹, James M. Russell², Alice M. Doughty^{1,3},
Jennifer A. Howley^{1,^}, Jonathan W. Chipman¹, David Cavagnaro¹, Bob Nakileza⁴, and
Susan H. Zimmerman⁵

¹Department of Earth Sciences, Dartmouth College, Hanover, NH 03755.

*²Department of Earth, Environmental, and Planetary Sciences, Brown University,
Providence, RI 02912.*

³Geology Department, Bates College, Lewiston, ME 04240.

⁴Mountain Resource Centre, Makerere University, Kampala, Uganda.

*⁵Center for Accelerator Mass Spectrometry, Lawrence Livermore National Laboratory,
Livermore, CA 94550.*

*[^]New Hampshire Department of Health and Human Services, Concord, NH 03301
(current address).*

3.1. Abstract

Atmospheric greenhouse-gas concentrations are thought to have synchronized global temperatures during Pleistocene glacial-interglacial cycles, yet their impact relative to changes in high-latitude insolation and ice sheet extent remain poorly constrained. Here we use tropical glacial fluctuations to assess the timing of low-latitude

temperature changes relative to global climate forcings. We report ^{10}Be ages of moraines in tropical East Africa and South America and show that glaciers reached their maxima at ~29-20 ka, during the global Last Glacial Maximum. Tropical glacial recession was underway by 20 ka, prior to the rapid CO_2 rise at ~18.2 ka. This “early” tropical warming was influenced by rising high-latitude insolation and coincident ice-sheet recession in both Polar Regions, which lowered the meridional thermal gradient and reduced tropical heat export to the high latitudes.

3.2. Introduction

The inter-hemispheric synchrony of the ice age cycles is one of the greatest questions in paleoclimate research. During much of the Pleistocene, Northern Hemisphere (NH) high-latitude summer insolation appears to have paced global glaciation, yet the mechanisms by which this climate response was propagated to the Southern Hemisphere (SH) are uncertain (Mercer, 1984; He et al., 2013). The rapid terminations of ice ages complicate the problem, as these occurred during periods of both high and low-amplitude NH high-latitude summer insolation changes (Denton et al., 2010).

Atmospheric greenhouse gases (GHGs), particularly CO_2 , are often invoked to explain the global synchrony of glacial-interglacial cycles (Saltzman and Maasch, 1990). This hypothesis is supported by near-concurrent changes in atmospheric CO_2 levels and Antarctic temperatures over the last ~800,000 years (Monnin et al., 2001), and numerous studies point to atmospheric GHGs as a key factor in warming the Earth during the last deglaciation (Clark et al., 2012; Shakun et al., 2012; Paillard, 2015). However other

climate processes may have also played a role in unifying global temperatures. For example, low NH high-latitude summer insolation and coincident high ice-sheet albedo altered the meridional thermal gradient, which likely impacted the strength and position of wind belts (Bush and Philander, 1998). Such changes in atmospheric circulation may have altered the strength of atmospheric and oceanic heat transport during glacial periods and induced cooling separate from that caused by GHG changes (Bush and Philander, 1998). The interconnected nature of high-latitude and GHG forcings complicates efforts to assess the sensitivity of Earth's climate system to changes in these boundary conditions.

The tropics are an ideal region in which to investigate the impact of global forcings on glacial-interglacial temperature change as they are far from the direct forcing from high-latitude insolation and large ice sheets (Pierrehumbert, 2002; Dyez and Ravelo, 2013). Tropical glaciers in particular provide an invaluable record of past change in the low-latitudes as these glaciers are highly sensitive to changes in temperature (Sagredo and Lowell, 2012; supplementary material) and their past fluctuations reflect changes in mid-tropospheric temperature (Jomelli et al., 2014). Prior work using cosmogenic beryllium-10 (^{10}Be) surface-exposure dating and analysis of glacially influenced lake sediments indicates that some tropical glaciers achieved their maximum extents either before or early during the Last Glacial Maximum (LGM; ~26.5-19.0 ka; Clark et al., 2009) (Seltzer et al., 2002; Smith et al., 2005a, 2005b; Clark et al., 2009) and that deglaciation from their LGM maxima was underway by ~20 ka, prior to the rapid CO_2 rise at ~18.2 ka (Shakun et al., 2015; Bromley et al., 2016). Critically, these existing data are limited to tropical South America. It is therefore unknown whether these records

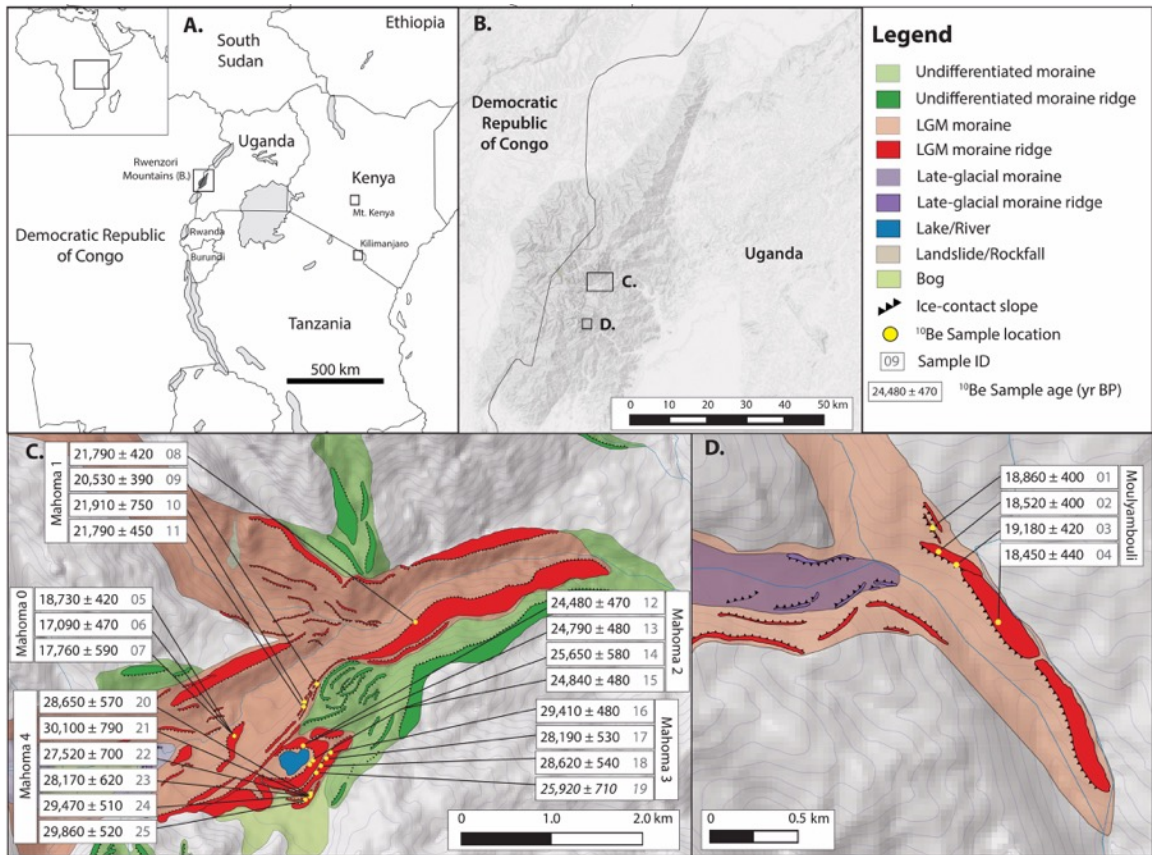


Figure 3.1. A) The Rwenzori Mountains (boxed) occur on the border between Uganda and the Democratic Republic of Congo. B) They are an uplifted horst of basement rock in the western branch of the East African Rift System. We targeted two separate catchments for glacial chronology: C) the Mubuku and D) the Moulyambouli valleys. Sample locations are yellow circles. ^{10}Be ages are in years ago with internal, one-sigma uncertainties. Numbers in grey are the Map ID # of samples in Tables A1-A3. One outlier [sample 19] is presented in italics.

reflect temperature across the wider tropics or more regional conditions. In addition, the recent determination of low-latitude, high-elevation cosmogenic nuclide production rates (Blard et al., 2013; Kelly et al., 2015) requires recalculation of ^{10}Be ages from tropical South America to allow for accurate comparison with global records.

To assess the timing of glacial fluctuations across the tropics during the LGM, we determined a chronology of past glacial extents using ^{10}Be dating of moraines in tropical East Africa, far from the South American tropics. Our ^{10}Be chronology includes seventeen new and eight previously published ages (Kelly et al., 2014) that constrain the timing of glacial fluctuations in the equatorial Rwenzori Mountains ($\sim 0.3^\circ\text{N}$, 30.0°E), located on the border between Uganda and the Democratic Republic of the Congo, during the LGM and the onset of deglaciation (Figure 3.1.). We also recalculated 177 ^{10}Be ages of 48 LGM moraines in tropical South America from ten prior studies (nine sites) (Figure 3.2.; supplementary material). All ages are calculated using a low-latitude, high-altitude ^{10}Be production rate (Kelly et al., 2015) and time-independent ("St") scaling (Lal, 1991; Stone, 2000; Nishiizumi et al., 1989)(supplementary material). There are significant uncertainties in tropical production-rate scaling during the LGM (Lifton et al., 2016); although these uncertainties impact comparisons of tropical ^{10}Be glacial chronologies with other paleoclimate records, they do not affect the larger conclusions of this work (supplementary material). All ^{10}Be ages reported here are of boulders on the crests of moraines, which we infer as representing the final sedimentation on the moraine. We therefore interpret a ^{10}Be age as the time of glacial recession from a given moraine and, thus, the onset of warming.

3.3. Results

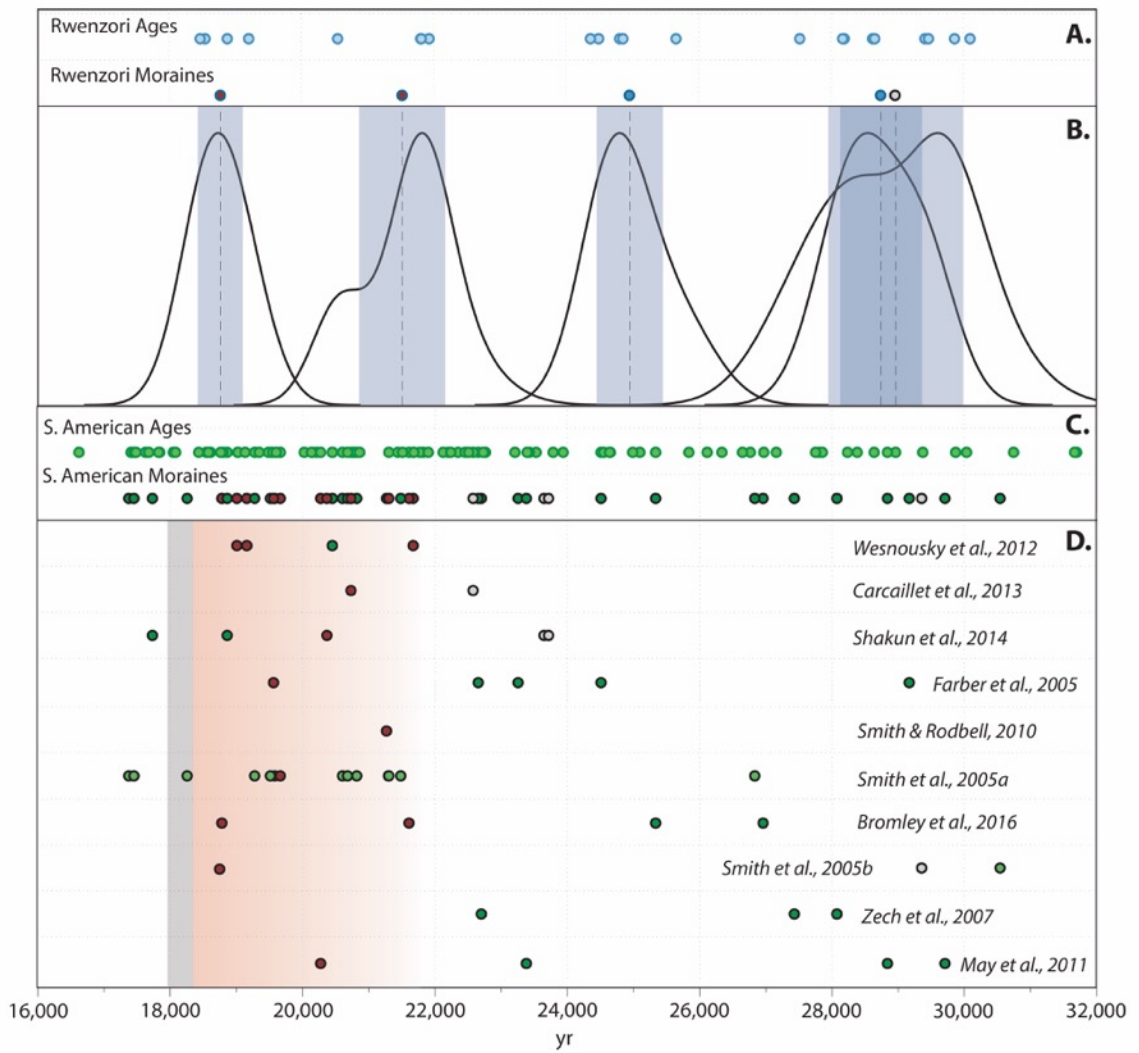
During the last ice age, glaciers from the central peaks in the Rwenzori Mountains flowed down the Bujuku and Mubuku valleys and merged to form a single glacier in the lower Mubuku valley that terminated at ~2000 m elevation (Figure 3.1.). At its maximum extent the glacier overtopped the right-lateral (south) valley wall, flowed ~500 m southward, and formed a series of moraines that enclose Lake Mahoma at ~3000 m a.s.l. (Figure 3.1., Table A1-A3). We term these moraines, from the outermost to innermost, the Mahoma 4, 3, 2, and 1 moraines. The two outermost moraines yield mean ^{10}Be ages of $28,960 \pm 1020$ yrs ago (Mahoma 4; $n = 6$) and $28,740 \pm 620$ yrs ago (Mahoma 3; $n = 3$; one outlier omitted). Inboard of the Mahoma 3 moraine, the Mahoma 2 moraine has a mean age of $24,940 \pm 500$ yrs ago ($n = 4$; Kelly et al., 2014). The Mahoma 2 moraine is cross cut by the largest of these moraines, Mahoma 1, which has a mean age of $21,500 \pm 650$ yrs ago ($n = 4$; Kelly et al., 2014) and extends down the Mubuku valley to ~2300 m a.s.l. The Mahoma 1 moraine has the greatest relief of any moraine within the sequence (~150 m relief above the Mubuku river valley floor) and marks the farthest down-valley extent of ice in the Mubuku valley during the last ice age. Approximately five kilometers up the Mubuku valley from the Mahoma 1 terminus, the Mahoma 0 moraine has a mean age of $17,860 \pm 830$ yrs ago ($n = 3$).

We also dated a single large (30-50 m relief above the valley floor), sharp-crested moraine in the Moulyambouli valley, ~10 km south of the Mubuku valley (Figure 3.1.). While there are smaller, partially preserved moraine segments on the steep bedrock valley wall opposite the large Moulyambouli moraine, there is not a sequence of moraines comparable to that in the Mubuku valley. ^{10}Be ages of the Moulyambouli moraine yield a

mean of $18,750 \pm 340$ yrs ago ($n = 4$). Because there is only a single moraine dated in the Moulyambouli valley, we rely more heavily on the moraine chronology from the Mubuku valley where we can track glacial fluctuations throughout the LGM. Together, the Mahoma and Moulyambouli moraine chronologies indicate that Rwenzori glaciers reached their maximum extents by ~ 28 ka. The glaciers fluctuated near their maxima until ~ 21.5 ka in the Mubuku valley and ~ 18.8 ka in the Moulyambouli valley, at which point deglaciation was underway in both catchments.

A comparison of the Rwenzori moraine chronology with 48 recalculated moraine ages from nine sites in tropical South America shows a broad similarity in the timing and structure of tropical glacial fluctuations during the LGM (Figure 3.2.; supplementary material). South American glaciers fluctuated throughout the LGM, with some glaciers achieving their maximum extents by ~ 28 - 29 ka. Similar to the Rwenzori glaciers, the tropical South American glaciers retreated from or from near their LGM maxima by ~ 20 - 19 ka. Together, the Rwenzori and South American moraine chronologies show a coherent signal of cool tropical temperatures during the LGM until the onset of glacial recession indicating warming at ~ 20 - 19 ka.

Figure 3.2. The Rwenzori (Mahoma 1-4 and Moulyambouli moraines) and recalculated tropical South American LGM moraine chronologies. (A) Light blue circles are individual Rwenzori ^{10}Be ages. Dark blue circles are arithmetic-mean moraine ages. (B) Rwenzori moraine ages as normalized probability (camel) plots with one-sigma, internal highlighted uncertainties in blue. (C) Recalculated tropical South American ^{10}Be ages (see supplemental material for details; number IDs in Figure 3.2. correspond with assigned IDs in site descriptions in supplementary material). Light green circles are individual ^{10}Be ages and dark green circles are arithmetic-mean moraine ages. For both the Rwenzori and tropical South American moraine chronologies, grey circles mark the outermost moraine in a given catchment, if dated. Red circles mark the onset of recession from or from near the LGM maximum ice extent in each catchment. (D) Arithmetic-mean moraine ages grouped by original study. The red-shaded interval highlights the onset of glacial recession in the Rwenzori and tropical South America. The gray bar indicates the timing of the CO_2 rise at ~ 18.2 ka (Marcott et al. 2014).



3.4. Discussion

The coincidence of tropical glacial maxima with a minimum in NH high-latitude summer insolation, high global ice-sheet volume, and low atmospheric GHG concentrations shows that tropical temperatures were sensitive to these global climate forcings during the LGM (Figure 3.3.). Milankovitch theory holds that low NH high-latitude summer insolation enabled the growth of NH ice sheets, which in turn cooled the planet via increased albedo (Milankovitch, 1941; Paillard, 2015). Because late Pleistocene sea-level changes largely reflect changes in NH ice sheets (Lambeck et al., 2014), we use sea level as a proxy for NH ice-sheet volume. By this metric, the period of most extensive NH ice sheets (~29-19 ka), and likely the period of greatest ice-sheet albedo forcing, is coincident with the time of expanded tropical glaciers. GHG radiative forcing was also low from ~34 to 18 ka (Bereiter et al., 2015; Rhodes et al., 2014; Ahn and Brook, 2008; Figure 3.3.), which presumably reinforced tropical cooling during the LGM (Lea et al., 2004), particularly at high altitudes (Loomis et al., 2017).

Although atmospheric GHG concentrations influenced tropical cooling during the LGM, the glacial chronologies presented here indicate that tropical warming began 'early' (i.e., at ~20-19 ka), prior to the rapid CO₂ rise at ~18.2 ka (Marcott et al., 2014) that is hypothesized to have influenced global deglaciation (e.g., Denton et al., 2010). GHG radiative forcing rose by ~0.5 W/m² between ~25 and 20 ka but stagnated or fell between ~20 and 18 ka, at a time when tropical glaciers receded (Figure 3.3.). In addition, mean-annual-equatorial insolation decreased by ~2.0 W/m² between ~30-16 ka. Although the rate and magnitude of equatorial insolation change was low, this trend would have presumably encouraged glacial advance rather than recession. Despite the

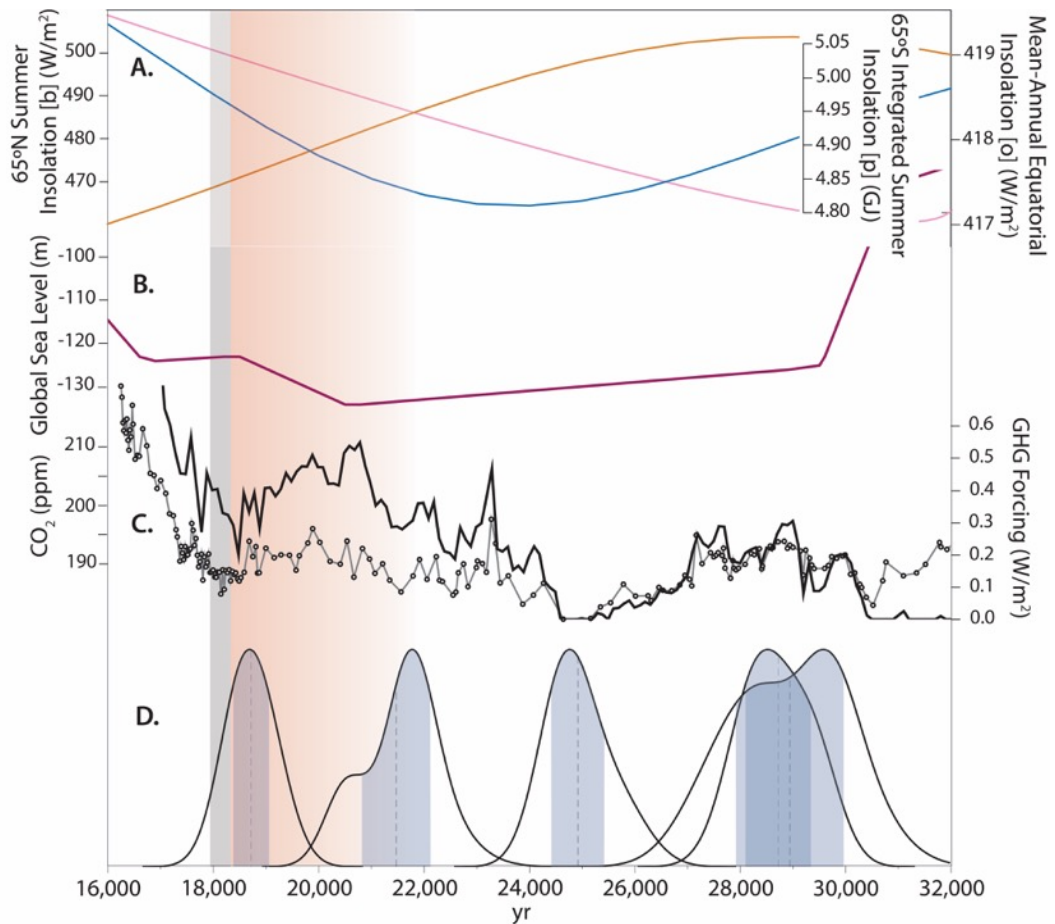


Figure 3.3. Global boundary conditions during the LGM including (A) NH high-latitude summer insolation [blue], mean-annual equatorial insolation [orange], and integrated SH high-latitude summer insolation [pink] (Berger and Loutre, 1991), (B) global sea level (Lambeck et al., 2014), and (C) normalized GHG forcing from CO₂, methane, and N₂O (Bereiter et al., 2015; Rhodes et al., 2014; Ahn and Brook, 2008). Atmospheric CO₂ concentration is also shown independently (linked black circles). (D) The Rwenzori glacial chronology (as in Figure 3.2) indicates expanded ice coincident with low values of each of the global boundary conditions (A-C). The red-shaded region and grey bar indicate the onset of tropical glacial recession and rapid atmospheric CO₂ rise, respectively, as in Figure 3.2.

trends in these forcings, the “early” warming registered by tropical glaciers is supported by temperature reconstructions from East African lake sediments that document the onset of deglacial warming at ~20 ka (Tierney et al., 2008, Loomis et al., 2012)(Figure 3.4.). Moreover, synthesized tropical sea surface temperature (SST) records (Shakun et al., 2012) indicate that warming was underway across the tropical ocean (30N-30S) by at least ~19 ka (Figure 3.4.).

Coincident with, or perhaps prior to, the tropical warming at ~20-19 ka, NH and SH high-latitude regions warmed. The Laurentide Ice Sheet began to retreat from or from near its maximum extents by at least ~20 ka (Balco et al., 2002; Ullman et al., 2014), driven by rising NH high-latitude summer insolation after ~24 ka (Ullman et al., 2014). Deglaciation on the Antarctic Peninsula (Weber et al., 2014) and the onset of warming in West Antarctica (Fudge et al., 2013) are dated to ~20 ka, and are attributed to increasing SH summer duration (Denton and Huybers, 2008; Weber et al., 2014). The rise in global sea level at ~21-19 ka (Lambeck et al., 2014) likely reflects the recession of these large polar ice sheets. Compilations of other northern high- and mid-latitude terrestrial and oceanic records likewise suggest warming was underway by ~20 ka; southern mid-latitude oceanic records (Shakun et al., 2012) show the onset of warming by ~21-20 ka.

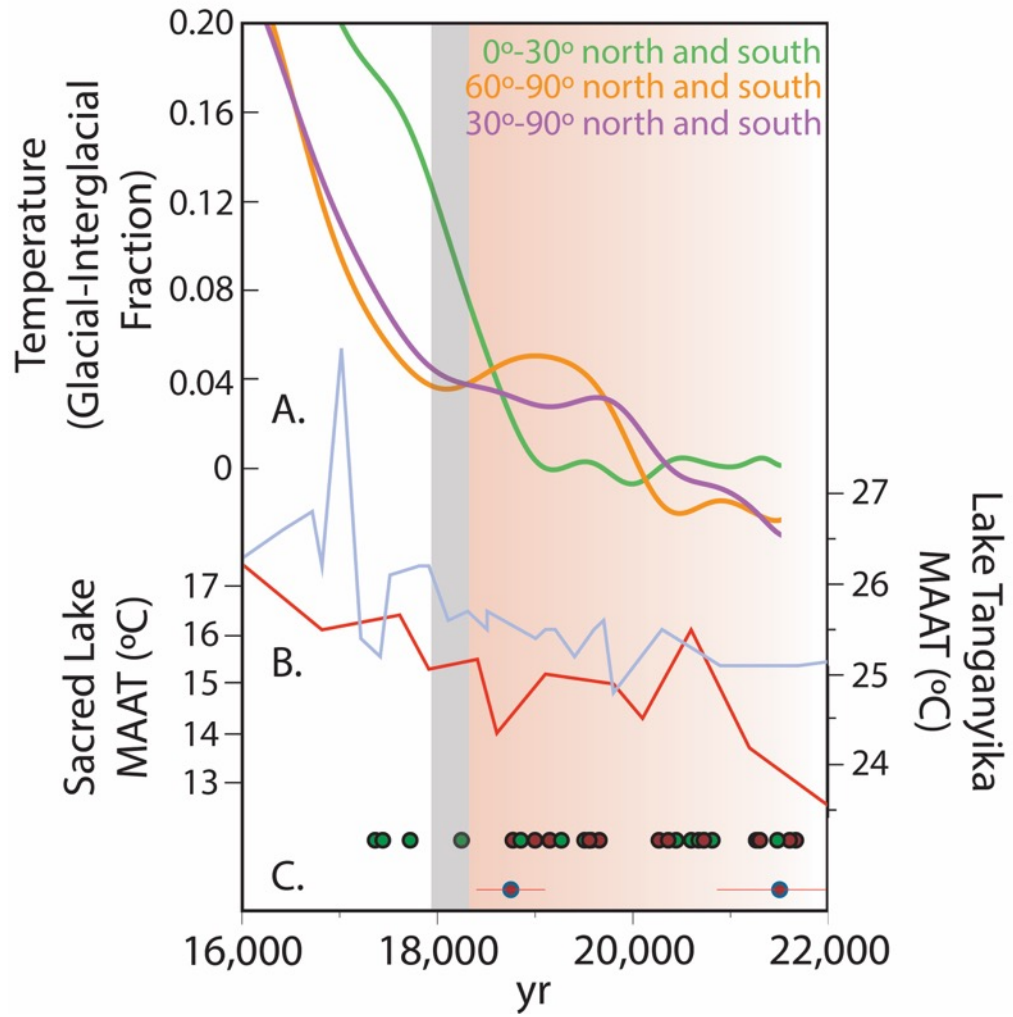
We suggest that the warming and deglaciation in high-latitude regions by ~20 ka led to a reduction of Earth’s meridional thermal gradient (Fudge et al., 2013), and that this reduced gradient influenced warming in the tropics (Figure 3.4.). The global atmosphere can be modeled as a ‘heat engine’, with net flow from warm ‘source’ regions at low latitudes to cool heat ‘sinks’ at high latitudes (Peixoto and Oort, 1992). The efficiency of heat flow is greatest when the temperature difference between source and

sink regions is large and decreases when the temperature gradient between these regions is reduced. The export of heat from the tropics is dominated by the Hadley circulation, the strength of which is positively related to the meridional thermal gradient (Held and Hou, 1980). This relationship is apparent in simulations of anthropogenic global warming that show decreased Hadley circulation strength as the thermal gradient between the tropics and the poles is reduced (Tanaka et al., 2005; Lu et al., 2007; Vecchi et al., 2007). By analogy, we infer that the insolation-induced warming of high-latitude regions marked by the recession of NH and SH ice sheets at ~21-20 ka influenced tropical warming through reducing the Hadley circulation strength and, thus, net tropical heat export. Slackened Hadley circulation also would have likely decreased poleward oceanic heat export by tropical surface currents (Boccaletti et al., 2004; Fedorov et al., 2015), further reinforcing tropical warming. Indeed, tropical SSTs likewise began to rise at or just before ~19 ka (Shakun et al., 2012; Figure 3.4.).

One hypothesis arising from this mechanism is that tropical glacial recession should have occurred nearly coincident with, or immediately after, increases in high-latitude temperatures. Tropical glacial recession was underway only after ~20-19 ka. In contrast, compilations of higher latitude temperature records suggest high-latitude warming initiated at ~21-20 ka (Figure 3.4.). Future work to test this hypothesis should focus on further high-resolution reconstructions of tropical temperatures, including dating of tropical glacial extents in Africa and elsewhere in the global tropics, which will reduce uncertainties in the precise phasing of high- and low-latitude glacial fluctuations during the LGM. Nevertheless, our results show that tropical temperatures respond to remote,

high-latitude climate forcing, and that climate models should account for warming prior to ~18 ka absent the influence of GHG forcing.

Figure 3.4. Longitudinal temperature changes at the onset of the last deglaciation from syntheses of global temperature records (Shakun et al., 2012). (A) Average NH and SH temperature changes relative to changes in the low latitudes. All values plotted versus the net fraction of glacial-interglacial temperature change, as in Shakun et al. (2012). (B) Organic geochemical temperature reconstructions from tropical African lakes Tanganyika (light blue; Tierney et al., 2008) and Sacred (red; Loomis et al., 2017), as plotted by Loomis et al. (2017). (C) Tropical moraine ages as in Figure 3.2., with tropical South American arithmetic-mean moraine ages at the top and Rwenzori moraine ages (with 1-sigma error) below.



3.5. Materials and Methods

3.5.1. Field Methodology

We conducted three field seasons in the Mubuku, Bujuku, and Moulyambouli valleys of the Rwenzori Mountains (~0.3°N, 30°E) between 2012 and 2016. We sampled large (2-4 m diameter) boulders on the crests of moraines that showed little or no sign of post-depositional movement or modification. We obtained ~0.5-1 kg pieces of the upper 3-5 cm of boulders using a hammer and chisel or a battery-powered hammer drill. We measured the surface dip of each sample using a handheld Suunto compass and measured any potential shielding by topography using a Suunto clinometer. Where possible, we sampled flat rock surfaces with no dip in order to minimize potential uncertainties in the shielding correction. We recorded the location and elevation of each sample at the time of collection using a handheld Garmin GPS. We averaged GPS measurements over the course of 2 to 5 minutes, sufficient to record ≥ 100 measurements. We then recorded the average location and elevation values for each sample (vertical error ± 3 m, horizontal error ± 1 m).

3.5.2. Lab Methodology

We measured the thickness of each sample to the nearest millimeter (± 1 mm) using calipers before crushing and milling the sample to the 210-750 μm grain-size. We then put the 210-750 μm grain-size fraction through a series of O-phosphoric acid, sodium hydroxide, and dilute hydrofluoric-nitric acid leaches to etch quartz and dissolve other minerals. Once we obtained pure quartz, we spiked each sample, as well as a process blank, with a known mass of ^9Be carrier and digested the sample in hydrofluoric

acid. The carrier used is a ^9Be carrier developed at Dartmouth from a deeply buried beryl crystal. For carrier concentrations see Table A1. We then used a modified version of the procedures described in Schaefer et al. (2009) to isolate beryllium from each sample and the process blank. $^{10}\text{Be}/^9\text{Be}$ ratios of samples were measured at the Center for Accelerator Mass Spectrometry at Lawrence Livermore National Laboratory and normalized to the 07KNST3110 standard (Nishiizumi et al., 2007). Once obtained, we subtracted the $^{10}\text{Be}/^9\text{Be}$ process blank ratio from the $^{10}\text{Be}/^9\text{Be}$ ratios of measured samples and used the blank-corrected sample ratios to determine the concentration of ^{10}Be in each sample per gram of quartz. For process blank ratios see Table A1.

3.5.3. ^{10}Be Age calculation

We calculated the Rwenzori ^{10}Be ages using Version 3 of the online exposure age calculator described by Balco et al. (2008) and subsequently updated (Balco et al., 2008) using a low-latitude, high-altitude ^{10}Be production rate (Kelly et al., 2015) and time-independent ("St") scaling (Lal, 1991; Stone, 2000; Nishiizumi et al., 1989)(Tables A1, A2; Figure A1). Two ^{10}Be production-rate calibrations from high-elevation sites in the tropics (both in South America; Blard et al., 2013; Kelly et al., 2015) yield the most robust calibration results when paired with the time-independent ("St") scaling, which suggests that this method may be most appropriate for sites such as the Rwenzori. We note that these ^{10}Be production-rate calibrations employ glacial deposits that date to ~13-11 kyr BP, younger than the Last Glacial Maximum (LGM).

Assuming that changes in the geomagnetic field influenced the cosmic ray flux and, thus, the cosmogenic ^{10}Be production rate during and since the LGM, an alternative,

time-dependent scheme may be more appropriate (i.e., "LSDn", Lifton et al., 2014). These alternative age calculations are shown in Table A2. However, because of the uncertainties of ^{10}Be production-rate variability and scaling frameworks in the low latitudes (Lifton, 2016) we choose to base our interpretations on ^{10}Be ages calculated using "St" scaling. Alternative scaling schemes "LSDn" and "Lm" (Balco et al., 2008) yield less accurate calibrations of the Kelly et al. (2015) dataset, with the "Lm" scaling scheme producing the greatest scatter within the resulting calibration data. Moreover, "Lm" scaling is based upon paleomagnetic models (Balco et al., 2008); because the theorized impacts of shifts in the magnetic field on nuclide production are greatest within the low latitude regions (Borchers et al., 2016), we suggest that the "Lm" scaling scheme is less appropriate than alternative scaling schemes in the tropics. "LSDn" scaling yields more accurate calibration results than the "Lm" scaling and is based upon cosmic-ray flux rather than magnetic field models (Lifton et al., 2014; Borchers et al., 2016). Although we use and discuss ^{10}Be ages calculated using "St" scaling within this study, our interpretations regarding the timing of tropical glaciation (during the global LGM) and onset of deglaciation (at ~20-19 ka) do not change with "LSDn"-based calculations.

We did not correct the Rwenzori ^{10}Be ages for the potential influence of boulder surface erosion. Although many samples showed evidence of surface erosion (e.g., exfoliation, raised quartz veins), ^{10}Be ages obtained from raised quartz veins are indistinguishable from those obtained from boulder surfaces. For example, on the Mahoma 4 moraine samples RZ-16-49 ($28,650 \pm 570$ yrs) and RZ-16-50 ($30,100 \pm 790$ yrs) are from raised quartz veins (1-3 cm above the boulder surface) on gneissic boulders. The other four samples from the Mahoma 4 moraine are from gneissic boulder surfaces

and yielded ages between ~29.9 and 27.5 ka. The arithmetic mean age of the Mahoma 4 moraine including these quartz-vein samples ($28,960 \pm 1020$ yrs) is statistically indistinguishable from the mean with these ages excluded ($28,750 \pm 1100$ yrs).

In addition, we did not correct the Rwenzori ^{10}Be ages for the influence of cover by snow/ice, soil or vegetation. We suggest that snow and ice do not persist on the ground for any length of time at the sample elevations (~2635-2990 m asl) due to the relatively warm temperatures and intense equatorial solar radiation. Although the majority of samples were covered by moss or soil and vegetation, we believe that the consistency of ^{10}Be ages on individual moraines indicates that any shielding by soil and vegetation was negligible.

The chi-squared (χ^2) value of each moraine, except for the Mahoma 3 moraine, is lower than the expected value (Table A3). This indicates that any age scatter between samples on individual landforms can be explained through analytical uncertainty alone rather than through any post-depositional processes or modification. We identified outliers within the dataset using Chauvenet's Criterion. After removing a single outlier (RZ-13-63) from the Mahoma 3 group, the χ^2 value of the Mahoma 3 moraine is lower than the expected χ^2 value. Sample RZ-13-63 from the Mahoma 3 moraine was the only sample identified as an outlier, and is not included within our interpretations or discussion.

Certain samples were measured multiple times (i.e., two separate quartz aliquots from the same rock sample were processed and measured) to check for internal sample age consistency. These samples are marked and all ^{10}Be ages are shown in Tables A1-A2. We use the secondary aliquot (aliquot 'a') measurements for our analysis of sample ages

from moraine Mahoma 0, as the original sample measurements returned abnormally low accelerator currents during measurement at LLNL. For this reason, we suggest that the ages from the duplicate run (aliquot a) are more robust. For all other sample ages we utilize the original age measurements, although we note that aliquot ‘a’ measurement ages for all other samples are within error of original measurements.

3.5.4. Recalculation of Pre-existing Tropical ^{10}Be datasets

We recalculated ^{10}Be ages from prior studies on tropical glaciers using the same methodology described above for the Rwenzori ^{10}Be ages. We provide a brief review of these “ ^{10}Be tropical data” below. Although we recalculated the ^{10}Be ages from the tropics using the St scaling scheme (Lal, 1991; Stone, 2000; Nishiizumi et al., 1989), we note that the differences in tropical ^{10}Be ages calculated using the Lm (Balco et al., 2008) and LSDn (Lifton et al., 2014) scaling schemes are similar to those for the Rwenzori (see Table A1).

For the purpose of making the most direct comparisons possible in the discussion of the paper, we chose to include only prior work that used ^{10}Be dating to develop glacial chronologies. Therefore, we do not include prior studies that used radiocarbon dating of organic material associated with moraines or surface exposure dating of moraines using other cosmogenic nuclides such as ^{36}Cl and ^3He . However, we note that these additional data neither alter nor counter our broader interpretations.

With the recalculated ^{10}Be ages from prior studies in the tropics, we assigned moraine ages at sites using the following methodology:

First, we excluded ^{10}Be ages identified as outliers by the original authors. We also excluded ^{10}Be ages that were not from moraines (i.e., ^{10}Be ages of bedrock surfaces or boulders on bedrock surfaces). We then plotted the locations of ^{10}Be ages in GoogleEarth and evaluated the glacial geologic contexts of the ages. We checked these locations against the original published maps of ^{10}Be ages and glacial geomorphology in order to ensure that samples plotted correctly as reported in the prior studies. We assigned each sample to a moraine based on the original authors' interpretations. However, where authors grouped ^{10}Be ages of multiple landforms into a single mean age or moraine group, we attempted to assign ^{10}Be ages to individual moraines using GoogleEarth. Once each ^{10}Be age was assigned to a moraine, we calculated the arithmetic-mean age of the moraine. Descriptions of the recalculated ^{10}Be datasets and assigned moraine ages are given below (see Tropical ^{10}Be Site Descriptions). Because our study focuses on the LGM and the onset of the last deglaciation, we excluded ^{10}Be ages >40 ka and arithmetic-mean moraine ages >30 ka, as well as ^{10}Be ages <17 ka from prior studies.

Where possible, we also assessed whether individual moraines mark the onset of recession from at or near the LGM maximum position of a given glacier. This was not always possible because at some sites only lateral, composite moraines are dated. We detail these classifications below. All data are recorded in Table A4.

3.6. Acknowledgements

We thank the Ugandan Wildlife Authority and the Uganda National Council on Science and Technology for their support of this project. We also thank Rwenzori Mountaineering

Services and Rwenzori Trekking Services for their logistical and safety support while in the field. This is LLNL-JRNL-759653.

Funding: This work was supported by grants from the National Science Foundation (EAR-1702293; GSS-1558358), National Geographic, and the Comer Family Foundation. Satellite imagery was granted by the Digital Globe Foundation and additional student field support came from Sigma Xi.

Author Contributions: MSJ, MAK, JRR, and AMD collected samples, analyzed results, wrote and edited the paper and figures. MSJ, JAH, and SHZ processed samples for analysis. DC collected and processed samples for analysis. SHZ analyzed samples. JWC and SHZ edited the paper and figures. MAK, JRR, and BN conceptualized the project. BN coordinated the project within Uganda.

Competing Interests: The authors declare no competing interests.

Data and Materials Availability: All data is available in the manuscript and supplementary and auxiliary materials.

CHAPTER 4
GLACIAL FLUCTUATIONS IN TROPICAL AFRICA DURING
THE LAST DEGLACIATION

M.S. Jackson¹, M.A. Kelly¹, J.M. Russell², A.M. Doughty³, J.A. Howley^{1^}, J. Chipman¹,
D.A. Cavagnaro¹, M.B. Baber¹, S.H. Zimmerman⁴, B. Nakileza⁵

¹*Department of Earth Sciences, Dartmouth College, Hanover, NH 03755.*

²*Department of Earth, Environmental, and Planetary Sciences, Brown University,
Providence, RI 02912.*

³*Geology Department, Bates College, Lewiston, ME 04240.*

⁴*Center for Accelerator Mass Spectrometry, Lawrence Livermore National Laboratory,
Livermore, CA 94550.*

⁵*Mountain Resource Centre, Makerere University, Kampala, Uganda.*

[^]*New Hampshire Department of Health and Human Services, Concord, NH 03301
(current address).*

4.1. Abstract

The tropics are a dynamic component of the global climate system and exert profound influence on modern inter-annual climate variability. Yet the role of the tropics in past climate changes, particularly in abrupt, millennial-scale climate events during the last deglaciation, is uncertain. This is due in part to the relative paucity of terrestrial temperature records in the tropics, which hinders efforts to understand the global pattern

and timing of deglacial warming and abrupt climate events. Glaciers in the tropics are sensitive to temperature. Mapping and dating past tropical glacial fluctuations therefore provides a record of past temperature changes in the low latitudes. We report a chronology of past glacial extents in the Rwenzori Mountains of Uganda (0.3°N, 30°E). The chronology includes 51 beryllium-10 (^{10}Be) surface-exposure ages from three separate glacier catchments. Results indicate that Rwenzori glaciers retreated during Heinrich Stadial 1 and were more extensive during the Antarctic Cold Reversal than during the subsequent Younger Dryas. Rwenzori glaciers retreated rapidly during the early Holocene, likely to within their late Holocene extents. The Rwenzori glacial chronology is similar to glacial chronologies from tropical South America. This similarity suggests coherent, tropics-wide temperature fluctuations during the last deglaciation. These results also indicate that tropical temperature changes were unique from high-latitude Northern and Southern Hemisphere patterns of deglacial warming. The Rwenzori glacial chronology therefore helps constrain the global footprint of abrupt climate events during the last deglaciation and the potential mechanisms that influenced tropical climate following the last ice age.

4.2. Introduction

The termination of the last ice age, known as Termination 1, represents the greatest natural climate warming of the last 100,000 years and is marked by distinct shifts in Earth's atmospheric and oceanic circulation (Broecker and Denton, 1989; Denton et al., 2010). The mechanisms which initiated and propagated deglacial warming around the globe, however, remain unresolved. While a period of significant global warming,

Termination 1 was also punctuated by abrupt climate events such as the Antarctic Cold Reversal (ACR; ~14.7-13.0 ka) and the Younger Dryas (YD; ~12.9-11.6 ka). Resolving the global pattern of deglacial climate change is crucial for understanding better the climate system, its response to rapid warming, and the mechanisms that influenced deglacial abrupt climate events. In some regions such as the tropics, however, there are few data with which to constrain paleoclimate conditions during Termination 1.

The tropics (23°N-23°S) comprise nearly half the Earth's surface and are the primary source of latent heat and water vapor to the global atmosphere (Pierrehumbert, 1999). Through phenomena such as the El Niño Southern Oscillation (ENSO) the tropics are also a dominant control on interannual climate variability (e.g., Sobel and Bretherton, 2000). The tropics therefore are a key, dynamic element of the global climate system. Yet records of past tropical climate conditions, particularly past temperatures in terrestrial tropical regions, are scarce. More records are needed to reconstruct past tropical climate conditions and understand tropical climate changes in a global context.

Glacial mass balance in the humid inner tropics (~10°N-10°S) is controlled primarily by temperature (Taylor et al., 2006; Kaser and Osmaston, 2002; Sagredo and Lowell, 2012; Rupper et al., 2008). Past tropical glacier extents therefore can provide a valuable proxy for low-latitude tropospheric temperatures. In recent decades cosmogenic nuclide surface-exposure dating has enabled the determination of ages of ancient glacial deposits and, thus, the reconstruction of past glacial fluctuations at sites around the globe. Surface-exposure chronologies from tropical South America suggest that glaciers there retreated during Heinrich Stadial 1 (HS1; ~18.0-14.6 ka)(e.g., Bromley et al., 2016; Mark et al., 2017) and were more extensive during the ACR than during the YD (Jomelli et al.,

2014; 2017; Mark et al., 2017). Due to a paucity of similar records from other terrestrial tropical regions it is unclear whether the wider tropics (i.e., regions outside of tropical South America) have a similar history. Thus, the spatial variability of past tropical temperature changes during Termination 1 remains enigmatic.

We report a new paleoclimate proxy record from an understudied region in tropical East Africa that spans from HS1 to the early Holocene. This record is based on a chronology of past glacial extents in the Rwenzori Mountains of Uganda (Figure 4.1.). The chronology consists of 51 beryllium-10 (^{10}Be) surface-exposure ages from three glacial catchments and includes samples from boulders on moraines as well as from perched boulders on bedrock. These data illuminate the timing and magnitude of glacial fluctuations in the Rwenzori during Termination 1. We then compare our results with similar ^{10}Be surface exposure chronologies of glacial extents from the tropical Andes to assess the potential uniformity of glacial and, thus, tropospheric temperature fluctuations across the low latitudes during Termination 1.

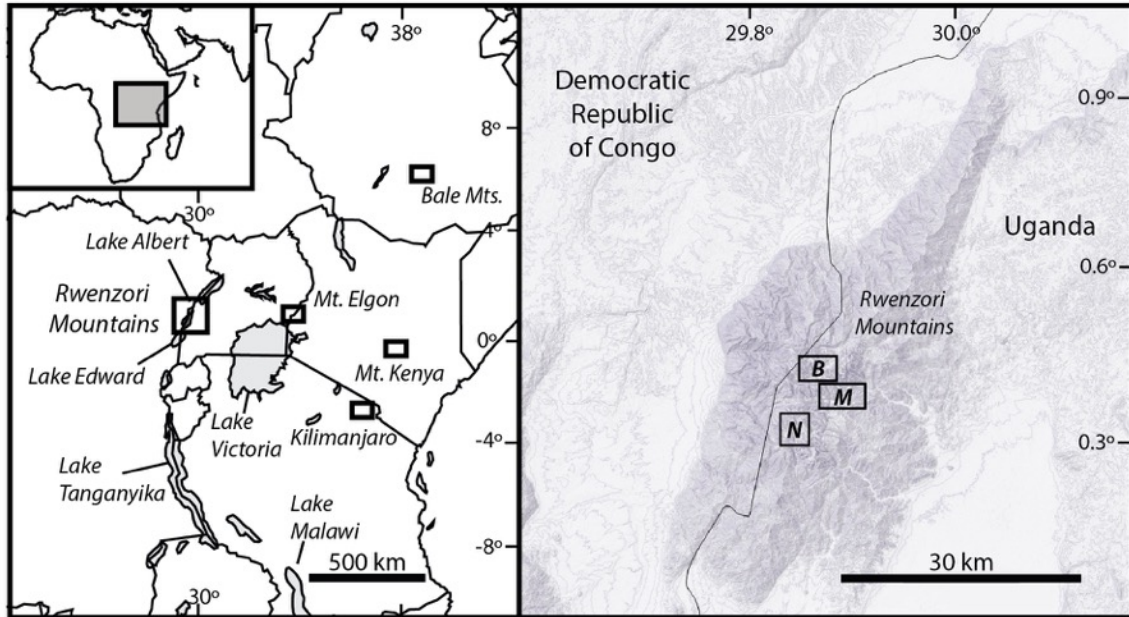


Figure 4.1. Map of East Africa and locations mentioned in the text (left). The Rwenzori Mountains are located on the border between Uganda and the Democratic Republic of Congo. Other glacialized or formerly glacialized sites in the region include Uganda's Mt. Elgon, Kilimanjaro in Tanzania, Mt. Kenya, and the Bale Mountains on the Ethiopian plateau. We targeted glacial deposits in three separate Rwenzori catchments (right): the Mubuku (M), Bujuku (B), and Nyamugasani (N) valleys. Boxed areas correspond to field areas detailed in Figures 4.4.-4.6.

4.3 Background

4.3.1. Geologic Setting and Previous Work

The Rwenzori Mountains (0.3°N, 30°E) are an uplifted horst of crystalline basement on the border between Uganda and the Democratic Republic of Congo (Figure 4.1.). The highest peak in the Rwenzori, Mt. Stanley, is 5109 m asl and stands roughly 360 m above the modern freezing level of ~4750 m asl (Lentini et al., 2011). The slopes of the

Rwenzori receive up to ~2.0-2.7 m precipitation each year with two distinct wet seasons during the boreal spring and autumn (Osmaston, 1989). Evergreen afro-alpine and montane vegetation dominate in the Rwenzori, with a marked altitudinal zonation in vegetation (Foster, 2001). Bare bedrock exposure is limited mostly to areas above 4000 m asl. Below this elevation glacial and landslide deposits are covered by moss and vegetation (Bauer et al., 2010).

The first reported observations of glacial extents in the Rwenzori were made in 1906 CE by the Duke of Abruzzi (Abruzzi, 1907). Rwenzori glaciers have since shrunk from an estimated area of ~6.5 km² in 1906 CE to ~0.96 km² in 2003 CE (Kaser and Noggler, 1996; Taylor et al., 2006). Clastic sediment inputs in Rwenzori lakes suggest that modern glacial retreat was likely underway by 1870 CE (Russell et al., 2009). Today glaciers persist in the Rwenzori only above ~4400 m asl on the slopes of Mt. Stanley, Mt. Baker, and Mt. Speke (Kaser and Osmaston, 2002; Taylor et al., 2006); these remaining glaciers are predicted to disappear within decades (Taylor et al., 2006).

Osmaston (1965) conducted extensive glacial-geomorphic mapping in the Rwenzori and, from this work, classified glacial moraines into five distinct stages based upon their inferred relative ages. These stages, from the youngest to oldest, include the Katarua, Rwimi, Lake Mahoma, Omurubaho, and Lac Gris, and were formed by glacial fluctuations that occurred prior to the Last Glacial Maximum (LGM; ~26.5-19 ka) to historical time. The Katarua and Rwimi stage moraines represent the most extensive preserved glacial extents in the Rwenzori and were estimated to pre-date the LGM. The Lake Mahoma stage moraines are high-relief (30-100 m high) ridges, including many well-preserved lateral moraines, that extend as low as ~2000 m asl. Osmaston (1989)

estimated the Lake Mahoma stage moraines to be at least ~15 ka in age and perhaps to correspond to the LGM. The Omurubaho stage moraines are lower relief (3-30 m high), occur at elevations ~3600-400 m asl, and are stratigraphically inboard of Lake Mahoma stage moraines. Although estimated to have formed during the Holocene, Osmaston (1989) refrained from placing more certain age constraint on the Omurubaho stage moraines. The Lac Gris stage moraines mark near-historical ice margins and are within 90-100 m of reported 1906 CE glacial extents (Osmaston, 1989). Osmaston (1989) estimated Lac Gris stage moraines to be ~700-100 years in age. Bergström (1955) used lichenometry to estimate that Lac Gris stage moraines near the margin of Elena Glacier on Mt. Stanley were deposited at ~1750 CE, although the rate at which lichen colonizes such deposits in the Rwenzori is unconstrained (Osmaston, 1989).

Until recently the only numerical age control on Rwenzori deglaciation was from two radiocarbon ages from high alpine lake sediments. At Lake Mahoma (~3000 m asl), Livingstone (1962) reported a bulk radiocarbon age of ~17.5 ka from the bottom 20 cm of organic-rich sediments which overlie inorganic silts. This age provides a minimum-limiting age on deglaciation from the Lake Mahoma stage moraines in the lower Mubuku valley. In the Butahu valley, basal sediments from Upper Lake Kitandara (~4000 m asl) yield a radiocarbon age of ~7.7 ka and provide similar minimum-limiting age control on deglaciation (Livingstone, 1967). Unlike Lake Mahoma, Upper Lake Kitandara is not directly associated with moraines. Recent applications of ^{10}Be surface-exposure dating (hereinafter ^{10}Be dating) have shown this method to be useful to date Rwenzori glacial deposits. Eight ^{10}Be ages of boulders on two Lake Mahoma stage moraines in the lower Mubuku valley indicate deposition at ~21.5 and ~24.9 ka, during the global LGM (Kelly

et al., 2014). More detailed mapping and dating of these moraines indicates expanded glaciers from ~29.0 ka to 21.5 ka in Mubuku valley and until ~18.9 ka in the more southern Moulyambouli valley (Chapter 3). The timing and extent of glacial fluctuations in the Rwenzori following the LGM, however, remain unresolved (Taylor and Osmaston, 2002).

Paleotemperature records constructed using branched glycerol dialkyl glycerol tetraethers (brGDGTs) in tropical African lake sediments indicate the region warmed throughout HS1 (Weijers et al., 2007; Loomis et al., 2017). However, these records do not show a unified signal of regional ACR or YD cooling. Certain records suggest that regional temperatures plateaued through much of the ACR and YD (Weijers et al., 2007), whereas others indicate relatively cool conditions during the YD interval (Loomis et al., 2012; 2017). In contrast, paleoprecipitation records show evidence for marked millennial-scale changes in regional hydrology following the LGM. A synthesis of East African lake sediment records by Gasse (2000) indicates that intense aridity during HS1 rapidly gave way to wetter conditions at ~15.0-14.5 ka, near the start of the ACR. Wet conditions persisted until ~12.5 ka, during the YD.

Relative aridity during the latter portion of the YD was followed by a rapid return to wet conditions at ~11.6 ka. This transition also marks the onset of the African Humid Period (AHP), an interval of increased precipitation across the African tropics that lasted until ~5 ka (deMenocal et al., 2000; Garcin et al., 2007). Complementing the Gasse (2000) synthesis, records from Lake Albert, north of the Rwenzori, indicate more arid conditions in the region between ~13.5 and 11.2 ka (Beuning et al., 1998; Berke et al., 2014).

4.3.2. Study Sites

We focused our study on three Rwenzori catchments: the Mubuku, Bujuku, and Nyamugasani valleys, each of which contain glacial deposits amenable for ^{10}Be dating (Figure 4.1.).

Mubuku valley

The eastern flank of Mt. Baker marks the head of the Mubuku valley. The valley trends east-west and its upper reaches are bounded by steep, faulted bedrock walls composed of strongly foliated gneisses (McConnell, 1959)(Figure 4.2.). The lower Mubuku valley is marked by large (>100 m high) Lake Mahoma stage lateral moraines (Osmaston, 1989) dated to ~29.0-21.5 ka (Kelly et al., 2014; Chapter 3). Deglaciation from the LGM maximum extent was underway by ~21.5 ka (Chapter 3). Inboard of these LGM deposits, additional lower-relief (10-30 m) moraines occur along the valley floor up to an elevation of ~3000 m asl. Many of these moraines are bisected by the Mubuku river and all are classified as Lake Mahoma stage deposits by Osmaston (1989). No Omurubaho stage moraines occur up valley of the Lake Mahoma stage moraines.

Bujuku valley

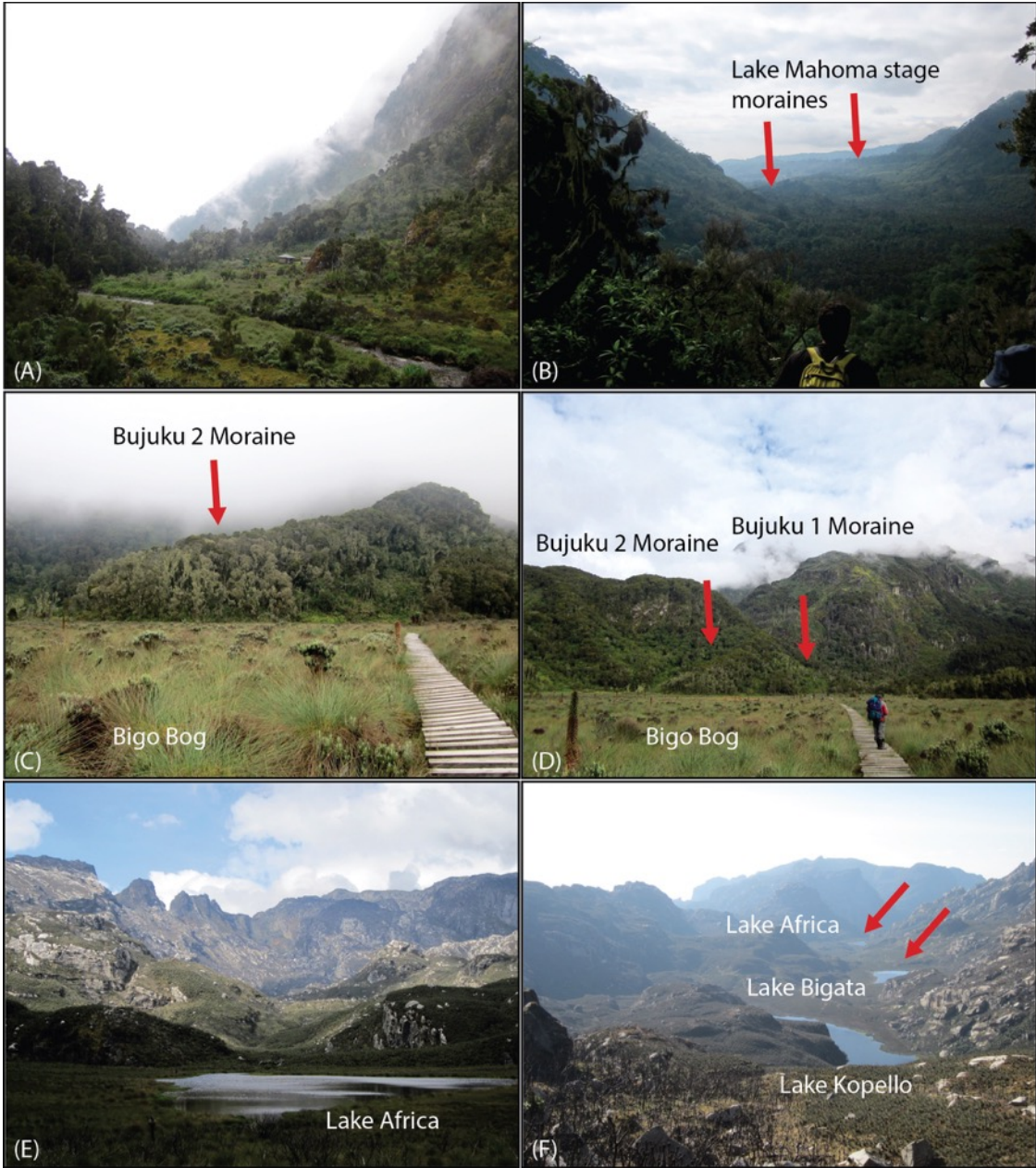
The Bujuku valley trends eastward from the Rwenzori high peaks before turning southeast toward the Mubuku-Bujuku rivers' confluence. The valley is underlain by migmatic gneisses and amphibolite. The southern side of the valley floor is composed primarily of volcanic lithologies whereas the northern valley walls, especially the slopes of Mt. Speke, are predominantly gneissic (McConnell, 1959). The valley walls are steep

and, in the upper valley near Lake Bujuku, they are obscured by active slope processes and rockfalls (Figure 4.2.). Where unobscured by vegetation, glacial molding and striations are visible on the bedrock valley walls and floor. Above the Mubuku-Bujuku rivers' confluence are a set of Lake Mahoma stage moraines deposited on steep valley walls (Osmaston, 1989). Eight km up valley from the Mubuku-Bujuku rivers' confluence a large (~kilometer wide) wetland occurs. This area is known as Bigo Bog and marks an infilled reach of the valley at the confluence of multiple catchments (Osmaston, 1989) (Figure 4.2.). The bog is bounded on both its up-valley and down-valley sides by Omurubaho stage moraines (Osmaston, 1989). Additional Omurubaho stage moraines occur ~1.5 km up valley of Bigo Bog. No additional moraines are preserved between these Omurubaho deposits and the presumed historical Lac Gris stage deposits on the slopes of Mt. Speke and Mt. Baker (Osmaston, 1989).

Nyamugasani valley

The southward trending Nyamugasani valley extends from Mt. Weisman to the southern edge of the Rwenzori massif, where prominent but undated Lake Mahoma stage moraines rise at least 100 m above the Nyamugasani river. The valley is underlain by migmatic gneiss and granite with some areas of amphibolite (McConnell et al., 1959). The upper reach of the Nyamugasani valley contains numerous lakes, some of which are dammed by bedrock and some by Omurubaho-stage moraines (Figure 4.2.). The upper Nyamugasani valley walls are less steep than those in the Mubuku and Bujuku valleys. Exposed, molded bedrock is readily visible, although the valley floor is infilled with lakes and wetlands and may be over-deepened in certain locations.

Figure 4.2. (A) The Guy Yeomen hut is in the upper reach of the Mubuku valley, which is bounded by steep, faulted bedrock walls. (B) The Mubuku valley floor contains numerous moraine forms, though it is primarily infilled by wetland. View is toward the southeast. (C) View toward the east from the Bigo Bog. Moraines, as seen here, trend from the Bujuku valley and abut the modern bog. (D) The Bigo Bog marks the confluence of multiple catchments, and is bounded by steep, gneissic bedrock walls. (E) In the upper Nyamugasani valley, Lake Africa (foreground) is one of two moraine dammed lakes. The peak of Mt. Weisman (distance) marks the head of the valley. View is to the north. (F). The Nyamugasani valley, with view to the south. Lake Kopello, dammed by bedrock, is visible in the foreground, with the moraine dammed Lakes Bigata and Africa in the distance. Moraines are highlighted by red arrows.



4.4. Methodology

Fieldwork took place over four field seasons between 2009 and 2016. While in the field we identified and classified glacial-geomorphic features based upon their morphology, weathering characteristics, and relative (stratigraphic) position. We also utilized 0.5-m resolution WorldView-1 satellite imagery to aid in identifying and contextualizing glacial features. We used these data to construct detailed glacial-geomorphic maps of the field area. All maps are drawn onto a 30-m resolution digital elevation model of the Rwenzori massif.

We collected samples for ^{10}Be dating from the uppermost surfaces (≤ 5 cm) of boulders on moraines and perched boulders on bedrock using a hammer and chisel or the “drill-and-blast” method of Kelly (2003). We selected boulders that showed no indication of post-depositional movement or alteration and recorded the location and elevation of each boulder using a handheld GPS (± 3 m vertical, ± 1 m horizontal). We sampled flat rock surfaces with no surface dip wherever possible in order to minimize potential uncertainties in the ultimate shielding correction. Where necessary, we measured the surface dip and dip direction of samples using a handheld compass. When weather permitted, we recorded topographic shielding using a handheld clinometer. Where low clouds prevented the measurement of topographic shielding in the field, we estimated shielding values later using a 30-m digital elevation model of the Rwenzori. This method yielded shielding values similar to (within $\sim 1\%$) those based upon field determined measurements.

We crushed the rock samples to a known grain size (210-750 μm) and used a series of paired $\text{H}_3\text{O}_4\text{P}/\text{NaOH}$ and HF/HNO_3 leaches to extract and clean quartz from the

bulk sample. We spiked each sample and process blank with a known amount of beryllium-9 (Table B3) made from a deeply buried beryl crystal and used a modified version of the methods described in Schaefer et al. (2009) to isolate beryllium from each sample and a process blank (Table B2, B3). All beryllium ratios were measured at the Lawrence Livermore National Laboratory Center for Accelerator Mass Spectrometry (CAMS) and normalized to the 07KNST3110 standard (Nishiizumi et al., 2007).

We calculated the Rwenzori ^{10}Be ages using a high-elevation, low-latitude production rate (Kelly et al., 2015), time-invariant scaling (“St” scaling; Lal, 1991; Stone, 2000), and version 3 of the online exposure age calculator described by Balco et al. (2008 and subsequently updated). Two ^{10}Be production rate calibration datasets from high-elevation, low-latitude sites (Blard et al., 2013; Kelly et al., 2015) yield the most accurate and precise results (lowest uncertainty by total scatter; Balco et al., 2008) when paired with time-independent scaling after Lal (1991) and Stone (2001)(i.e., “St” scaling). ^{10}Be ages calculated with this methodology are in Table B1. We also report ^{10}Be ages calculated using an alternative, time-dependent scaling framework (“LSDn”, Lifton et al., 2014) in Table B1. There is a maximum ~4.5% difference in the ^{10}Be ages calculated with these two methodologies. The choice of scaling framework employed does not change our overall interpretations.

We measured certain samples multiple times (that is, we isolated beryllium from two separate quartz aliquots from the same original rock sample) in order to check for sample consistency. These duplicate sample measurements (aliquot ‘x’) are reported in Table 1 but we do not include these data within our discussion or analysis, save for samples RZ-16-41x, RZ-16-43x, and RZ-16-44x. The initial measurements of these three

samples returned particularly low measurement current values (16, 25, and 14 microAmps on the third laser ablation, respectively), whereas the second ('x' aliquot) measurements were more robust (20, 19, and 22 microAmps on third laser ablation). For this reason, we utilize the 'x' aliquots in our discussion of these samples.

In addition to individual ^{10}Be ages and uncertainties we also report arithmetic mean moraine ages with the associated standard error and standard deviation for each landform with more than one representative ^{10}Be age (Table B1). We consider these mean moraine ages as indicative of the onset of ice recession following a glacial readvance or stillstand (i.e. the cessation of sediment deposition on the moraine). We do not report mean ages for perched boulder populations, which we interpret to indicate the timing of ice thinning or retreat past a given position rather than the age of a discrete landform. Instead we consider these ^{10}Be ages individually. Where ^{10}Be ages of landforms are out of stratigraphic order with other dated deposits up or down valley or do not yield a discrete age population, we report individual ^{10}Be ages rather than an arithmetic mean moraine age.

We did not correct the ^{10}Be ages for the potential influence of boulder surface erosion or cover by snow. Snow does not likely persist for a considerable length of time at the sample sites due to the intense equatorial solar radiation and warm daytime temperatures. Many boulders featured granular surface textures and, in some cases, showed evidence of exfoliation. The apparent degree of weathering, however, was variable between individual boulders and between lithologies. Prior work using ^{10}Be dating in the Rwenzori showed that raised quartz veins and boulder surfaces on the same moraine yield statistically similar ages (for LGM-age deposits). Due to the uncertainty in

erosion rates and the apparently negligible influence of erosion on ^{10}Be ages of LGM moraines, we refrain from correcting the ^{10}Be ages for erosion.

We also did not correct the ^{10}Be ages for cover by vegetation, but we describe its occurrence and potential influence in more detail here because most Rwenzori boulders sampled have or are surrounded by a thick vegetation or forest cover. The moraines in the Mubuku and Bujuku valleys are located in Montane Forest (1500-2500 m asl), Bamboo (2500-3000 m asl), and Heather/Rapanea (3000-4000 m asl) vegetation zones (Osmaston, 2006). Moraines in the Nyamugasani valley are located in the Heather/Rapanea (3000-4000 m asl) and Alpine (3800-4500 m asl) vegetation zones (Osmaston, 2006). In general, sampled boulders were covered by moss that was ~1-15 cm thick. In some cases boulders were covered by small shrubs (~1-1.5 m high) and trees (~10-40 cm diameter). In all three valleys the timing and pattern of forest succession since deglaciation from the LGM is uncertain and the types and thicknesses of vegetation cover on the boulders likely changed over time due to changes in climate. Plots of ^{10}Be ages with vegetation thickness on the sampled boulders show that there is no clear pattern of younger ages with thicker vegetation cover, suggesting that vegetation does not have a significant impact on the ^{10}Be ages. (Figure 4.3.).

Prior work has estimated the impact of vegetation cover on surface-exposure ages using a 'shredded biomass' model that assumes a uniform thickness and density of vegetation over a rock surface (Plug et al., 2007; Dunai et al., 2010). The average biomass of mosses in the Rwenzori Montane Forest zone is 0.004-0.25 g/cm² (Pentecost, 1998; Osmaston, 2006). We sampled the vegetation cover atop a boulder on the Mahoma 8 moraine (~2650 m asl) in Bujuku valley and determined a dry weight vegetation

density of $\sim 0.02\text{-}0.20\text{ g/cm}^3$. Using the ‘shredded biomass’ model, a vegetation thickness of 0-15 cm and density $0.02\text{-}0.25\text{ g/cm}^2$ atop a boulder would require a reduction of the ^{10}Be age of $\sim 0\text{-}3\%$ (Plug et al., 2007; Dunai et al., 2010). The modeled impact of temperate boreal or rainforest vegetation on the incoming cosmic ray flux suggests that nuclide production rates may be reduced by $\sim 2\text{-}7\%$ in areas of dense forest cover (Plug et al., 2007). The majority of this amelioration is caused by tree stems, although some also comes from shielding by the tree canopy. Due to the uncertainty of vegetation type and thickness over time, we refrain from correcting the Rwenzori ^{10}Be ages for the potential impacts of vegetation cover. However, based on prior work modeling the influence of vegetation cover, we suggest that any correction would likely reduce the ^{10}Be ages by only a few percent and, therefore, would not alter our overall interpretations.

All sampled moraines (except those in the Mubuku valley and in the Bujuku valley near the Mubuku-Bujuku rivers’ confluence) were originally classified as Omurubaho stage deposits by Osmaston (1989), who employed a moraine identification scheme by which each Rwenzori moraine was assigned a discrete numerical ID regardless of catchment or location. We choose to use a different terminology to clarify the stratigraphic relationship between moraines within each valley. Here we identify each moraine by the name of the valley in which it occurs and number each moraine based upon its stratigraphic position relative to other currently dated moraines in the valley. The innermost (most up valley) ^{10}Be -dated moraine in any catchment is denoted as moraine ‘0’.

To compare the timing of glacial events in the Rwenzori with tropical South American glacial chronologies we compiled ^{10}Be ages of 74 moraines (296 total ^{10}Be

ages) from sites that span from 6°N to 17°S in the South American Andes (Bromley et al., 2016, Jomelli et al., 2014, Glasser et al., 2009, Jomelli et al., 2011; Zech et al., 2010; Licciardi et al., 2009; Hall et al., 2009; Stansell et al., 2015; Carcaillet et al., 2013; Stansell et al., 2017; Smith et al., 2011). We calculate the ^{10}Be ages from tropical South America using the same production rate and scaling framework as is used for the Rwenzori data (i.e., the ^{10}Be production rate of Kelly et al., 2015 and time-invariant “St” scaling (Lal, 1991; Stone, 2000)). We assigned the ^{10}Be ages of samples to individual moraines based upon the interpretations of the original authors. We omitted outliers as identified by authors in the original publications. We do not include ^{10}Be ages from perched boulders on bedrock or from bedrock surfaces.

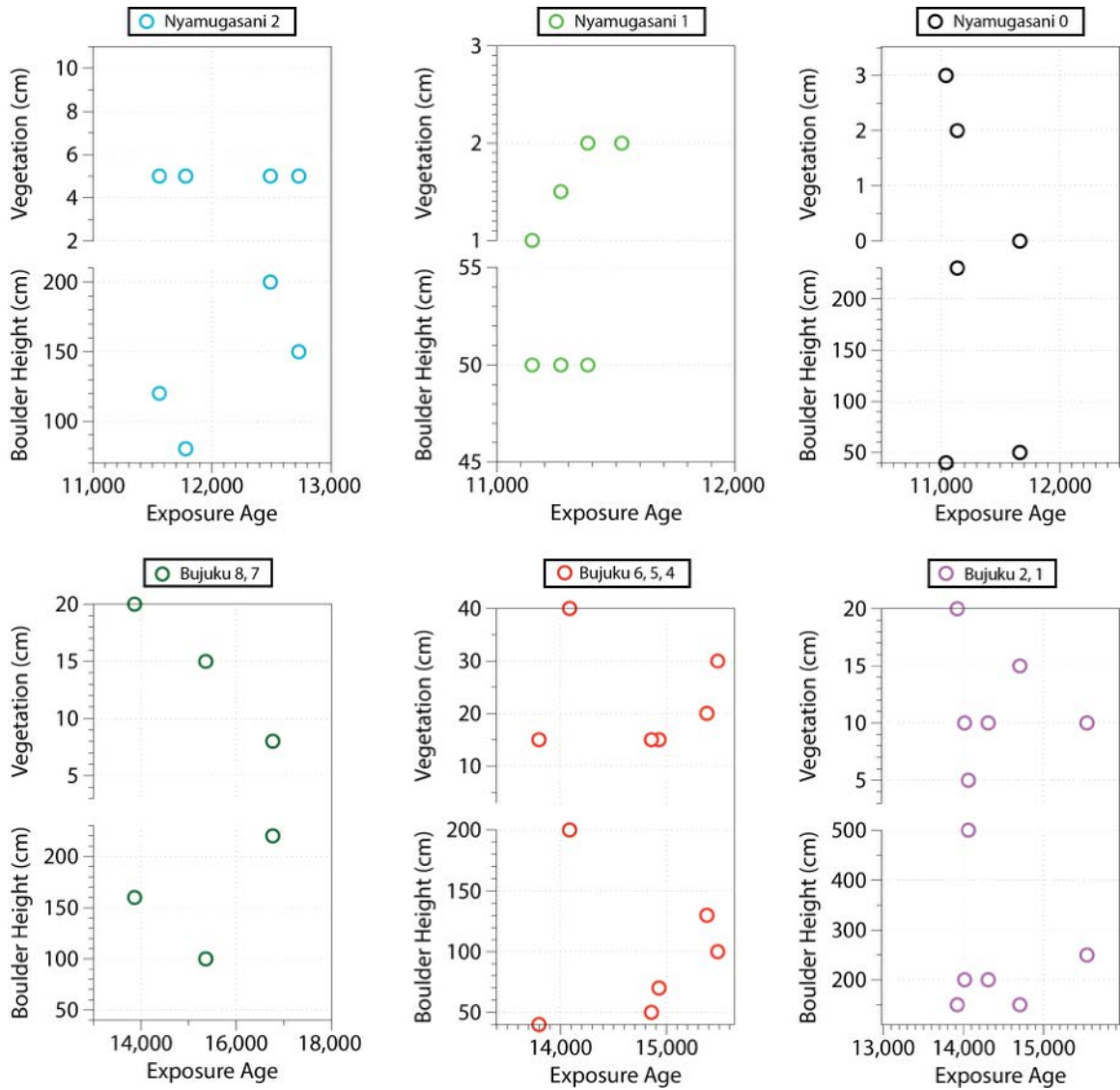


Figure 4.3. Individual beryllium-10 ages from Rwenzori moraines plotted versus vegetation thickness in cm (top) and boulder height (bottom). All data are color coded by individual moraines or, where moraines are in close geographic proximity, by moraine group.

4.5. Results

4.5.1. Mubuku valley

The left-lateral Mubuku 0 moraine occurs ~2.5 km up-valley of the Mubuku and Bujuku rivers' confluence, and is the innermost moraine within a sequence of moraine ridges in the Mubuku valley (Figure 4.4.). The crest of the moraine is well-defined, undulatory, and has roughly 10 m relief above the valley floor. The ice-contact moraine slope is particularly steep and may have been partially eroded by the Mubuku river. Three samples collected from the Mubuku 0 moraine yield ^{10}Be ages of 11.2 ± 0.3 , 13.8 ± 0.3 , and 12.6 ± 0.3 ka (RZ-16-41x, 43x, 44x). No moraines are preserved up valley of the Mubuku 0 moraine.

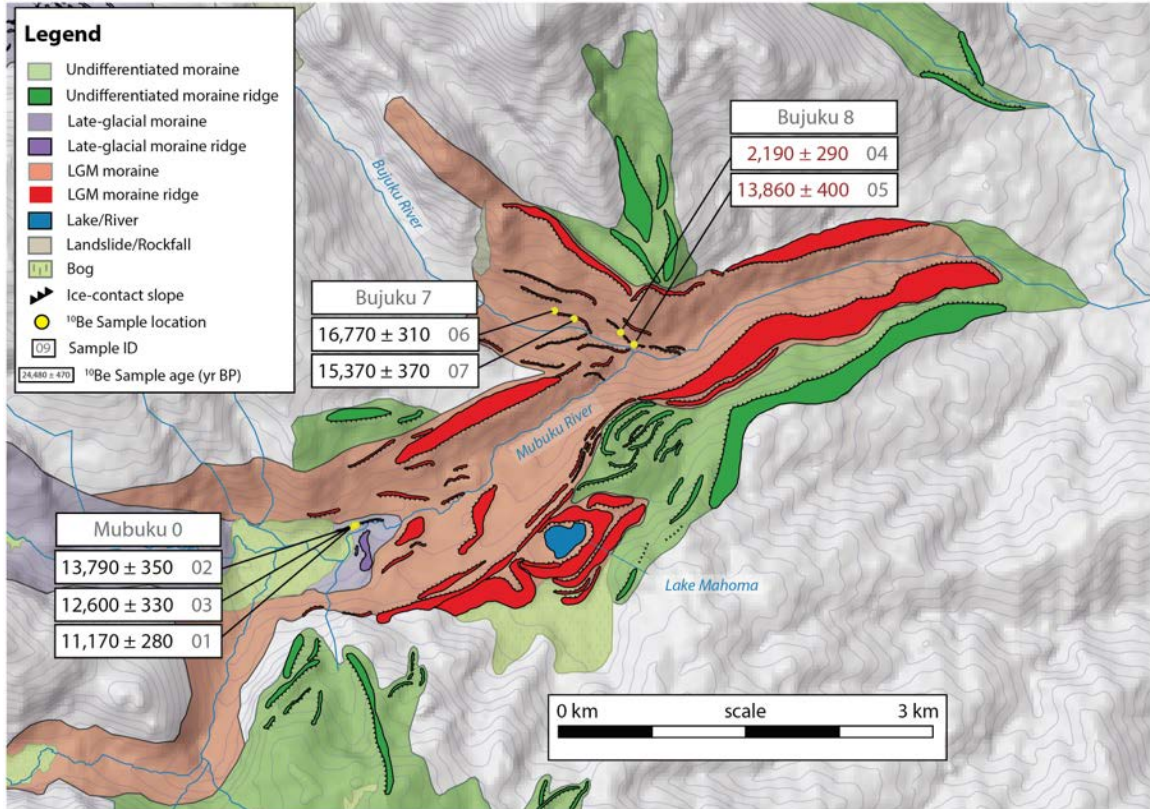


Figure 4.4. Glacial-geomorphic map of the Mubuku and lower Bujuku valleys with ^{10}Be ages as reported in Table B1. Ages we consider to be affected by post-depositional processes are shown in red. Sample ID numbers as in Table B1-B3 are in grey.

4.5.2. Bujuku valley

In the Bujuku valley, two left-lateral moraine segments, Bujuku 8 and Bujuku 7, occur ~100-300 m up-valley of the Mubuku-Bujuku rivers' confluence (Figure 4.3.) and mark the former extent of ice after it had separated from the once-joined Mubuku-Bujuku glacier. The moraine crests vary along their length from sharp and well-defined to rounded and less distinct. The moraines have ~1-5 m relief above the valley wall upon which they occur, and are located ~30-50 m above the Bujuku river, which has incised the valley floor. Two samples from the more down valley Bujuku 8 moraine yield ^{10}Be ages of 13.9 ± 0.4 ka (RZ-16-08) and 2.1 ± 0.3 ka (RZ-16-07). Immediately up valley, two samples from the Bujuku 7 moraine yield ^{10}Be ages of 15.4 ± 0.4 ka (RZ-16-03) and 16.8 ± 0.3 ka (RZ-16-02).

A large (0.25 km²) wetland known as Bigo Bog occurs ~8 km up valley from the Mubuku-Bujuku rivers' confluence (Figure 4.4.). The Bujuku river flows through the bog, and the area surrounding Bigo Bog is blanketed by drift. This deposit, which we term the Bigo drift, is identifiable in aerial imagery as a distinct change in vegetation, presumably due to differences in subsurface drainage, and on the ground through the appearance of large (1-3 m tall) boulders on the valley floor and walls. Three samples from boulders atop the outermost, down-valley limit of the Bigo drift yield ^{10}Be ages of 22.4 ± 0.5 , 15.9 ± 0.5 , and 11.1 ± 0.3 ka (RZ-16-13, 11, 09).

Up valley from the Bigo drift limit, the Bigo Bog is bounded by a series of tightly spaced moraines that converge toward the bog's down valley outlet where the Bujuku river emerges and flows down valley. We term these, from the outermost to the innermost, the Bujuku 6 to Bujuku 1 moraines. The Bujuku moraines feature sharp ridge

crests, and have ~10-20 m relief above the bog surface. Two samples from the outermost moraine, Bujuku 6, yield ^{10}Be ages of 13.6 ± 0.4 (RZ-16-25) and 9.3 ± 0.3 ka (RZ-16-24). Immediately inboard of Bujuku 6, two samples from the Bujuku 5 moraine yield a mean age of 15.0 ± 0.4 ka (RZ-16-21, 26). Inboard of the Bujuku 5 moraine, two samples from the Bujuku 4 moraine yield a mean age of 14.9 ± 0.4 ka (RZ-16-17, 18). A single sample from a dissected ridge segment on the Bujuku 3 moraine dates to 13.9 ± 0.4 ka (RZ-16-14).

A bedrock knob bisects the valley floor on the western, up valley edge of Bigo Bog. Right-lateral moraines on the northern flank of the knob both abut and plunge into the modern bog surface; these ridges mark the former position of a glacier which flowed from the upper Bujuku valley. Three samples from one of these lateral moraine ridges (Bujuku 2) yield a mean age of 14.7 ± 0.5 ka (RZ-12-11, 12, 13). Approximately 30 m below the Bujuku 2 moraine, three samples from the lateral Bujuku 1 moraine yields a mean age of 14.1 ± 0.1 ka (RZ-12-14, 15, 16). The next preserved moraines in the Bujuku valley occur ~1.5 km up valley from Bigo Bog, where a cluster of partially-preserved lateral moraine ridges mark the most up valley position of ice in the area surrounding Bigo Bog. Three samples from a right-lateral (Bujuku 0) moraine yield a mean age of $\sim 11.7 \pm 0.1$ ka (RZ-12-17, 18, RZ-16-31) We note that no additional moraines occur between the Bujuku 0 moraine and the Lac Gris stage (estimated historical-age; Osmaston, 1989) moraines on the slopes of Mt. Speke and Mt. Stanley.

In addition to boulders on moraine ridges, we dated three boulders on the toe of a landslide deposit near the outlet of Lake Bujuku, roughly two km up valley from the Bujuku 0 moraine. Two of these samples yield ^{10}Be ages of 11.0 ± 0.2 ka (both RZ-16-36

and 39). The third yields a ^{10}Be age of 12.4 ± 0.2 ka (RZ-16-35), which we interpret to reflect the influence of inherited ^{10}Be in the boulder surface. Because the valley floor must have been ice free at the time the landslide was emplaced, we consider ~ 11.0 ka as a minimum age for glacial recession past this site.

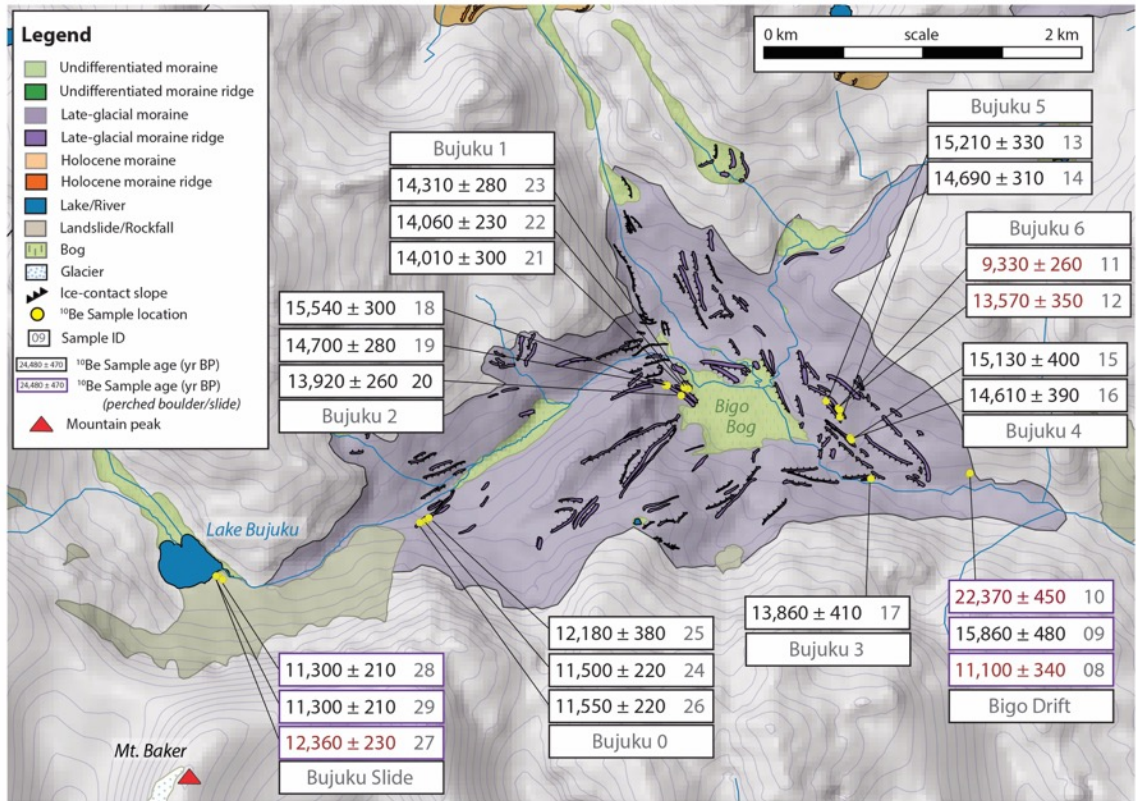


Figure 4.5. Glacial geomorphic map of the Bujuku valley. The area surrounding Bigo Bog is bounded by moraine ridges that delineate the former extent of glaciers fed from multiple catchments. ^{10}Be ages are as reported in Table B1 and include boulders on moraines (boxed in black) and perched boulders on bedrock (boxed in purple). Three samples from the toe of a landslide at the outlet of Lake Bujuku are also included (boxed in purple). Ages we consider to be affected by post-depositional processes or to contain inherited ^{10}Be are shown in red. Sample ID numbers as in Table B1-B3 are in grey.

4.5.3. Nyamugasani valley

In the Nyamugasani valley, two perched boulders on a bedrock rise that dams Lake Katunda yield ^{10}Be ages of 14.1 ± 0.3 (RZ-15-05) and 13.8 ± 0.3 ka (RZ-15-06) (Figure 4.5.). Approximately two km up valley from Lake Katunda, the upper Nyamugasani valley features a sequence of moraine ridges, two of which dam Lakes Africa and Bigata. Numerous perched boulders occur on the valley floor between the moraines. Lake Africa is dammed by the most down valley of these moraines, which we term the Nyamugasani 2 moraine. This moraine is $\sim 1\text{-}2$ m high above the valley floor and has a rounded crest. Four samples from the moraine yield ^{10}Be ages of 11.6 ± 0.2 , (both LA-2 and LA-5), 12.7 ± 0.3 (LA-1) and 12.5 ± 0.3 ka (LA-3). This moraine ridge occurs at a constriction in the valley and does not have multiple crests, although the population of ages from sampled boulders appears bi-modal. These ages provide an arithmetic mean moraine age of ~ 12.1 ka.

Roughly one kilometer up valley from the Nyamugasani 2 moraine, the Nyamugasani 1 moraine has relief of ~ 5 m above the valley floor and features a sharp crest. Four samples from this moraine ridge yield a mean age of 11.3 ± 0.1 ka (RZ-12-33, 34, 36, 37). Inboard of the Nyamugasani 1 moraine, Lake Bigata is dammed by the Nyamugasani 0 moraine. The Nyamugasani 0 moraine is similar in form to the Nyamugasani 1 moraine, with ~ 5 m relief above the valley floor. Four samples from the Nyamugasani 0 moraine crest yield a mean age of 11.2 ± 0.2 ka (RZ-12-38, 39, 41, 44). There are no additional moraines preserved up valley of the Nyamugasani 0 moraine, although numerous perched boulders occur on the valley floor.

Approximately 0.5 km up valley from Lake Bigata, Lake Kopello is dammed by a bedrock rise that transits the valley floor. Four samples collected from perched boulders on the crest of this bedrock rise yield ^{10}Be ages of 10.5 ± 0.3 (KOP-1), 11.8 ± 0.3 (KOP-2), 12.1 ± 0.3 (KOP-4A), and 11.0 ± 0.2 ka (RZ-15-12). Some ages of perched boulders (KOP-2, KOP-4A) are older than the ~ 11.2 ka age of the Nyamugasani 0 moraine and we suggest that these older ages are due to inherited ^{10}Be in sample surfaces. A fifth sample from the eastern end of the ridge where it intersects the valley wall yielded a ^{10}Be age of 8.3 ± 0.2 ka (KOP-5). We suggest that this age reflects post-depositional boulder movement or exhumation.

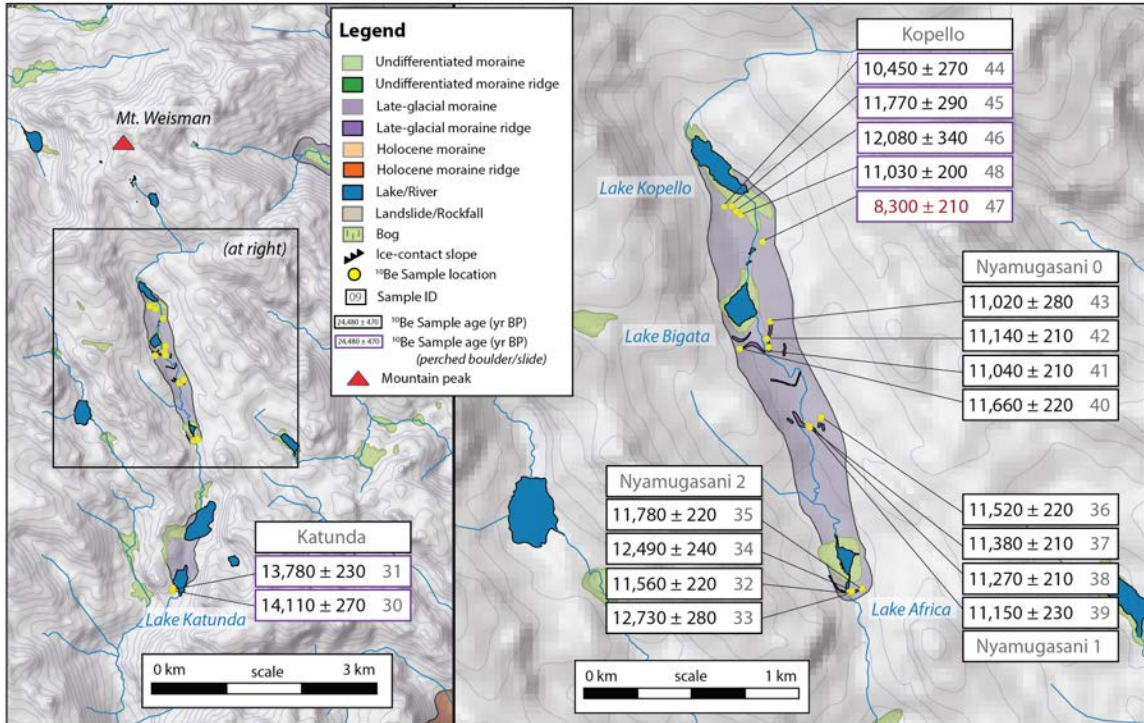


Figure 4.6. Glacial geomorphic map of the Nyamugasani valley and ^{10}Be ages as reported in Table B1. The valley trends southward from the peak of Mt. Weisman (left). In the upper reach of the valley are numerous lakes, some of which are dammed by moraines (right). Samples from the Nyamugasani valley include boulders on moraines (boxed in black) and perched boulders on bedrock (boxed in purple). Ages we consider to be affected by post-depositional processes are presented in red. Sample ID numbers as in Table B1-B3 are in grey.

4.6. Discussion

4.6.1. Rwenzori Ice Extents During Termination 1

Deglaciation in the Rwenzori was underway by ~21.5 ka and formerly conjoined ice from the Mubuku and Bujuku catchments separated by at least ~17.9 ka (Chapter 3). In the Mubuku valley, the Mubuku 0 moraine indicates that ice retreated at least an additional kilometer up valley from its ~17.9 ka extent by ~14-11 ka. This is equivalent to an ~45% reduction in the Mubuku glacier's length relative to its LGM maximum position (Figure 4.7.). In the Bujuku valley, ice retreated ~300 m up valley of the Mubuku-Bujuku rivers' confluence by ~16.8-15.4 ka, as indicated by ages of the left-lateral Bujuku 7 moraine and its projection toward the valley floor. Ice retreated an additional ~8 km up valley to the position of Bigo Bog by ~15.0 ka. Ice remained in Bigo Bog until ~14.1 ka before retreating up valley. Together, these ages indicate that between ~21.5 and ~15.0 ka the Bujuku valley glacier retreated ~8 km, an ~54% reduction in the Bujuku glacier's length relative to its LGM maximum position. Whether the pause in glacial retreat in Bigo Bog at ~15-14 ka was influenced in part by topography is unclear. Bigo Bog is a depression at the confluence of multiple catchments that was likely over-deepened by glacial erosion. It is possible that the over-deepened reach may have encouraged stagnation of the ice margin as it retreated. Although the position of the Bujuku glacier terminus in Bigo Bog at ~15-14 ka is uncertain because the dated lateral moraines plunge into the modern bog, the Bujuku 2 and 1 moraine ages indicate the glacier thinned between ~15 and 14 ka and retreated from the bog at ~14 ka.

There are no moraines preserved between the Bujuku 1 moraine (~14.1 ka) and the Bujuku 0 moraine (~11.7 ka), located ~1.5 km up valley. After ~11.7 ka glacial

recession is constrained by the occurrence of an undisturbed rockfall deposit that transits the valley floor and dates to ~11.0 ka. The lobate form of the rockfall suggests that the sediments associated with the event were free to travel across the valley floor unimpeded by a valley glacier. Based on this, we suggest that the rockfall site must have been ice free at the time of emplacement. Thus, the Bujuku glacier was up valley of the rockfall site by at least ~11.0 ka.

In the Nyamugasani valley, two perched boulders on bedrock near the outlet of Lake Katunda indicate deglaciation at ~14 ka, coincident with the timing of glacial retreat from Bigo Bog. This Lake Katunda bedrock is ~6.8 km up valley from outermost mapped (but not dated) Lake Mahoma stage moraines and so represents an ~54% reduction of the glacier's length between the (presumed) end of the LGM and ~14 ka (Figure 4.6.). The bi-modal age population of the Nyamugasani 2 moraine makes finer correlation of the deposit a challenge. It is possible that the two older ^{10}Be ages (~12.7 and 12.5 ka) are a result of inherited ^{10}Be in the sample surfaces, although the similarity of these ages (within internal measurement error) make this unlikely. The two younger ^{10}Be ages (~11.8 and 11.6 ka) may reflect post-depositional exhumation the landform or erosion of the boulder surfaces. Again, the similarity of these ages argues against such a scenario. It is possible that the moraine was initially abandoned at ~12.6 ka and then later re-occupied by a readvance, but there is no geomorphic evidence of glacial readvance at this site. Conservatively, we suggest that ice was at the Nyamugasani 2 moraine (~2 km inboard of its ~14 ka extent) by ~12.6 ka and that ice abandoned the moraine by ~11.6 ka. After ~11.6 ka ice retreated, depositing moraines 1-2 km up valley at ~11.3 and ~11.2 ka. After ~11.2 ka moraine deposition in the Nyamugasani valley ceased. The perched

boulders on the bedrock ridge that dams Lake Kopello indicate continued thinning or recession of ice past this location after ~11.2 ka.

We suggest that the stratigraphy and relatively small moraines emplaced after ~12 ka indicate that these represent only brief pauses in a larger pattern of ice retreat. The ~11.7 ka Bujuku 0 moraine is the only moraine in the valley younger than ~12 ka, and no additional moraines occur up valley. In the Nyamugasani valley, three moraines date to ~12-11 ka, yet these are low relief (~1-5 m) and show no indication of overriding previously emplaced glacial features. That moraine deposition occurred in the Nyamugasani but not the Bujuku valley may be due to differences in sediment supply or geometry between the valleys. Glaciers in both valleys retreated after ~11.6 ka and no moraines were deposited after ~11 ka until the late Holocene.

Overall the Rwenzori glacial chronology indicates significant post-LGM ice recession in multiple valleys. Deglaciation was underway by ~21-19 ka (Chapter 3). In the Bujuku and Nyamugasani valleys, glaciers shrank by ~54% between the end of the LGM and ~15-14 ka. After ~14 ka, glaciers again retreated. This second stage of recession was punctuated by brief pauses at ~11.6 -11 ka. After ~11 ka, glaciers retreated in all catchments. A primary implication of these results is that Rwenzori glaciers retreated during HS1 and were more extensive during the earliest ACR period than during the YD.

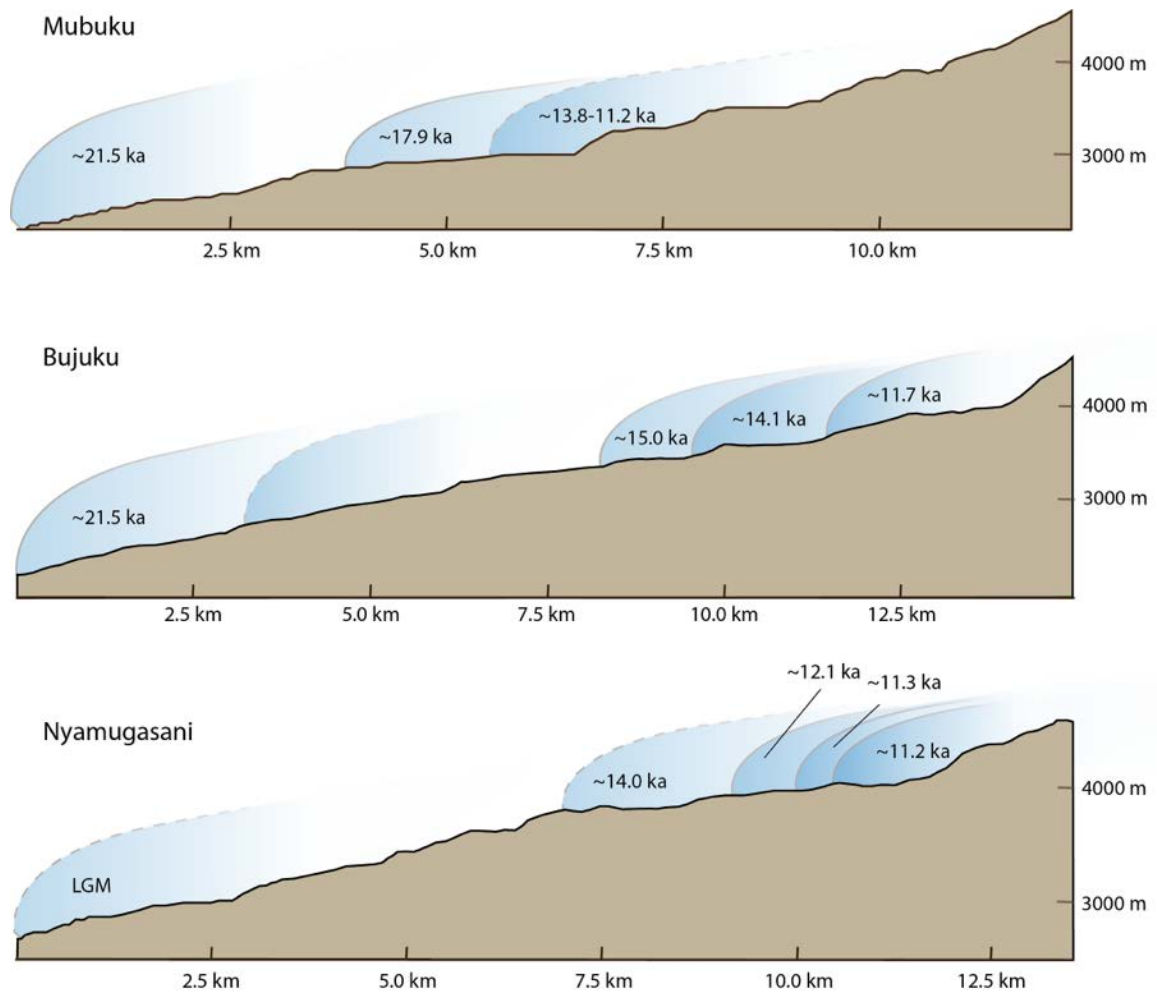


Figure 4.7. Changes in glacial extents in three Rwenzori during Termination 1. Dashed lines indicate inferred ice extents where ^{10}Be ages of a moraine have scatter (e.g., on the Mubuku 0 moraine) or are of perched boulders (e.g., in the Nyamugasani valley). Distance down valley is plotted relative to the dated or inferred LGM maximum position and measured along the (inferred) central glacier flowline and drawn onto a 30-m DEM. Elevation (m asl) is given individually for every valley on the right-hand side of each plot.

4.6.2. Glacial Fluctuations in East Africa

Elsewhere in tropical East Africa, sediments from Lake Garba Guracha (~3,950 m asl) in the Bale Mountains of Ethiopia indicate that glacial recession following the LGM was underway by at least ~17 ka (Tiercelin et al., 2008). The glacially-fed Lake Garba Gaucha registers high sedimentation rates between ~13.4 and 12.5 ka, which are interpreted as reflecting increased glacial melt (or, alternatively, readvance), although this signal may be complicated by bank or slope destabilization or changes in vegetation. Glacier-derived sediment input to the lake decreased after ~12.5 ka and the catchment was ice free by ~11.8 ka (Tiercelin et al., 2008). At Mt. Bada, Ethiopia, a minimum-limiting radiocarbon age from a bog at ~4130 m asl indicates glacial recession prior to ~13.3 ka (Hamilton, 1982). At Mt. Elgon, Uganda, two radiocarbon ages from Lake Kilimili (4,150 m asl) indicate glacial recession prior to ~12.9-12.6 ka (Hamilton and Perrott, 1978).

Chlorine-36 (^{36}Cl) surface-exposure dating of glacial deposits on Kilimanjaro and Mount Kenya yields information on the timing and magnitude of glacial recession at both sites (Shanahan and Zreda, 2000). On Kilimanjaro, ^{36}Cl ages from a left-lateral moraine on the south-facing slope of Mawenzi peak yield a mean age of 17.3 ± 2.9 ka ($n = 7$). Inboard of this moraine a suite of 3-4 nested moraines yield a mean age of 15.8 ± 2.5 ka ($n = 12$). A second group of samples from a lateral moraine on the eastern flank of Kibo peak are dated at 13.9 ± 2.3 ka ($n = 4$). On Mt. Kenya, two samples from a lateral moraine in the lower Gorges Valley yield a mean age of 14.7 ± 1.1 ka, and three samples up valley yield a mean age of 13.0 ± 1.9 ka. In contrast to the ^{36}Cl ages on Mt. Kenya, minimum-limiting radiocarbon ages of these moraines indicate deposition by 15.2 ± 1.2

ka (Mahaney, 1981). In summary, the glacial extent records from a wider East African region indicate recession from the LGM by ~17 and glacial readvances or standstills between ~15 and 12 ka, however the data are not of sufficient resolution to resolve the precise timings of changes in glacial extent. With an understanding of the differences in resolution, we suggest that the Rwenzori glacial chronology presented here is in general consistent with the prior work on past extents of East African glaciers during Termination 1.

4.6.3. Glacial Fluctuations in South America

Prior work synthesizing tropical South American glacial extents indicates deglaciation in the region initiated at ~20-19 ka and was followed by marked retreat of glaciers across the region during HS1 (Shakun et al., 2015; Bromley et al., 2016; Mark et al., 2017). Glacial recession was interrupted at ~16 ka, as indicated by moraine deposition at sites in Venezuela's Sierra Nevada (Carcaillet et al., 2013), the Cordillera Blanca, Cordillera Huayhuash, and Cordillera Oriental in Peru (Glasser et al., 2009; Hall et al., 2009; Bromley et al., 2016), and in Bolivia's Cordillera Cochabamba, (Zech et al., 2010). Following this pause, glacial recession continued until ice readvances or stillstands culminated at ~14.1-13.8 ka (e.g., Mark et al., 2017). Moraines dated to ~14 ka occur at sites in the Sierra Nevada de Cocoy in Colombia (Jomelli et al., 2014), in the central and southern Peruvian Andes (Glasser et al., 2009; Hall et al., 2009; Stansell et al., 2015), and in Bolivia (Zech et al., 2010). At and immediately following ~12 ka, moraine deposition at multiple sites in Colombia and Peru indicate glacial recession (Jomelli et al., 2014; Licciardi et al., 2009; Hall et al., 2009; Carcaillet et al., 2013;

Stansell et al., 2017). After ~11-10 ka, glaciers at most sites retreated rapidly to near their late Holocene extents, with few or no moraines deposited between early Holocene ice extents and (presumed) late Holocene moraines (Jomelli et al., 2014).

The tropical South American surface-exposure chronologies suggest that by ~15-14 ka glacial lengths were reduced by ~30-60% relative to their LGM maximum positions (e.g., Bromley et al., 2016) (Figure 4.8.). Between ~14 and 12 ka glaciers continued to retreat, but at a slower net rate. This period of more static glacial margins was followed by more rapid recession after ~12-11 ka, with many glaciers near or inboard of their late Holocene moraines by early Holocene time.

4.6.4. Controls on Tropical Glacial Mass Balance During Deglaciation

There are strong similarities between the Rwenzori and tropical South American glacial chronologies. In both regions recession from the LGM initiated by ~20-19 ka and continued during HS1, with glaciers shrinking by ~30-60% of their maximum LGM positions by ~14 ka. There are few moraines dated to the period between ~14 and ~12 ka, and net glacial recession slowed during this interval relative to the rate of net recession between the LGM and ~14 ka. Although glaciers did not retreat markedly between ~14 and 12 ka (Figure 4.8.), glaciers in both regions were more extensive during the ACR than during the YD. After ~12-11.6 ka, glaciers receded more rapidly to within late Holocene ice extents.

The regional coherence of tropical South American glacial fluctuations during the last deglaciation has been noted by previous studies (e.g., Mark et al., 2017) and used to argue for temperature as a primary control on tropical glacial mass balance (Jomelli et al.,

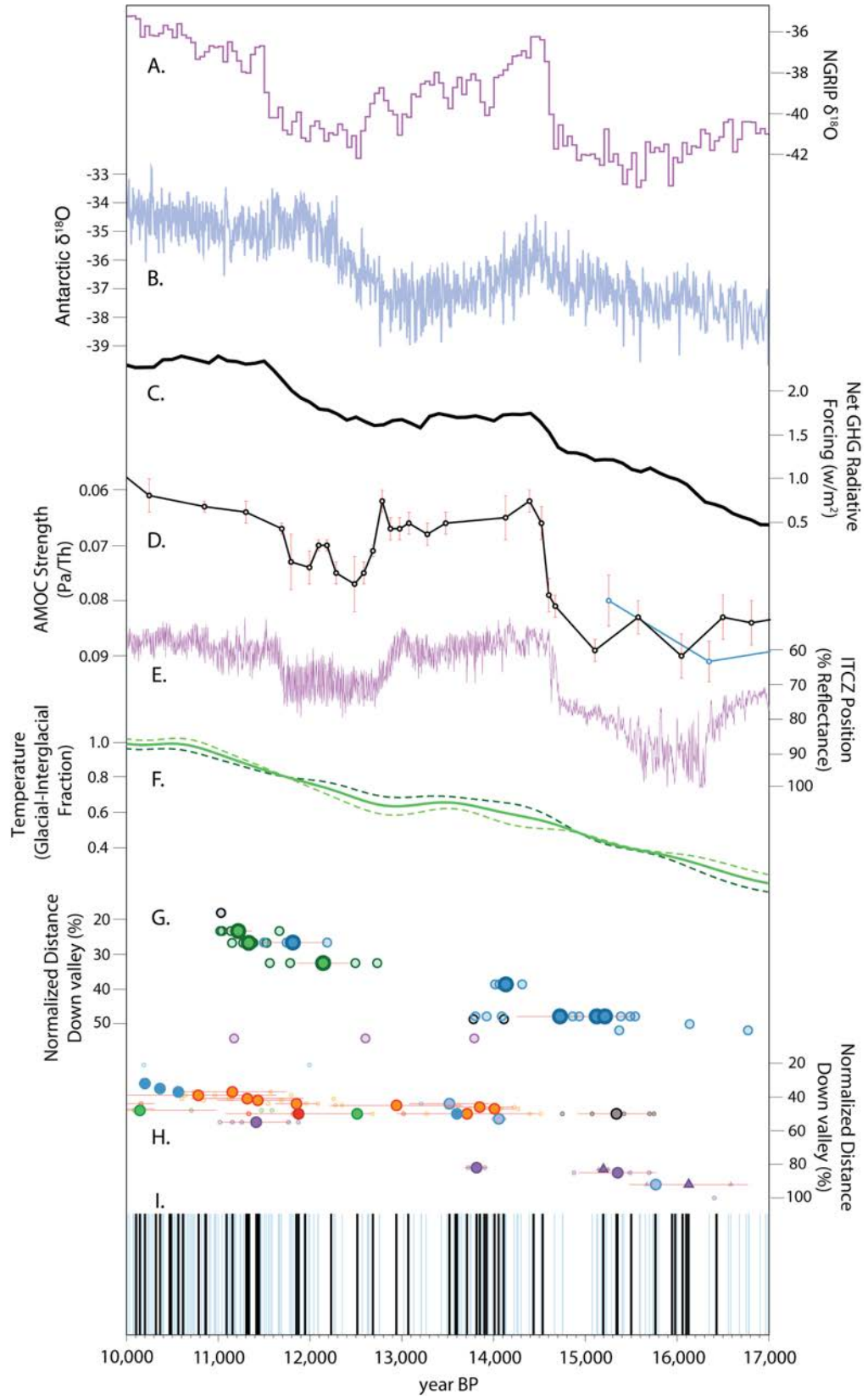
2014; Bromley et al., 2016). Based on the coherence of glacial fluctuations in the Rwenzori and tropical South America we suggest that tropical glaciers on both continents responded primarily to changes in low-latitude temperature during Termination 1. Precipitation varied distinctly between the northern and southern tropical Andes during deglaciation (Jomelli et al., 2014; Bromley et al., 2016; Novello et al., 2017) and these precipitation patterns are in turn unique from the pattern of precipitation change recorded in the African tropics (e.g., Gasse, 2000). Therefore, if precipitation were a primary control on tropical glacial mass balance we would expect glacial fluctuations in the Rwenzori and the northern and southern tropical Andes to have occurred at different times.

Two newly produced temperature reconstructions based on branched glycerol dialkyl glycerol tetraethers (brGDGTs) from alpine lakes on Mt. Kenya provide a direct comparison of changes in Rwenzori glacial extents with records of regional high-elevation temperature. The brGDGT records indicate marked warming during HS1 followed by more subdued warming after ~15-14 ka (Loomis et al., 2017). They also suggest that regional temperatures increased ~2°C between ~14 and 11 ka, with temperatures at ~11 ka only slightly below pre-industrial values (Loomis et al., 2017). Wider tropical temperature syntheses from low-elevation sites (both marine and lacustrine) records likewise suggest marked warming throughout HS1, with more static temperatures between ~14.0-12.5 ka (Shakun et al., 2012)(Figure 4.8.). The tropical glacial chronologies discussed here contribute to a global picture of tropical terrestrial temperatures during Termination 1 and can be used to investigate the possible mechanisms that initiated deglacial warming and abrupt climate events.

4.6.5. Potential Controls on Tropical Temperatures Following the LGM

Atmospheric greenhouse gases (GHGs), particularly CO₂, are a primary control on tropical temperatures over glacial-interglacial cycles (Lea, 2004), and are potential drivers of millennial-scale temperature changes during Termination 1. However, a comparison of the tropical glacial chronologies with global paleoclimate records shows that tropical glaciers receded (and, thus, tropical tropospheric temperatures increased) prior to the onset of rapid CO₂ rise at ~18.2 ka (Shakun et al., 2015; Bromley et al., 2016; Chapter 3). Moreover, the timing of subsequent GHG changes do not align with the timing of tropical temperature changes inferred from glacial fluctuations. For example, net radiative GHG forcing was stagnant between ~14.5 and 12.0 ka (Marcott et al., 2013; Ahn and Brook, 2008; Rhodes et al., 2014), with no decrease prior to or after ~14 ka. In contrast, tropical glaciers retreated between ~14 and 12, albeit at a slower net rate than during HS1. Net GHG forcing increased by ~12 ka, coincident with tropical warming inferred from glacial recession. This coincidence may indicate that changes in GHG concentrations contributed to the tropical warming. However, net GHG forcing was stable or perhaps decreasing during much of this interval (~14.5-12.5 ka), suggesting an additional mechanism influenced glacial recession – and tropical temperatures – during this time.

Figure 4.8. Global and tropical climate during the last deglaciation. (A) $\delta^{18}O$ from Greenland Ice Cores (NGRIP, 2004) and (B) West Antarctica (Fudge et al., 2013) indicate abrupt millennial-scale climate during Termination 1. (C) Net GHG forcing from CO_2 , CH_4 , and N_2O . (D) Changes in the strength of Atlantic Meridional Overturning Circulation (AMOC) strength (McManus et al., 2004; Böhm et al., 2015). (E) Position of the Intertropical Convergence Zone (ITCZ) reconstructed from terrestrial runoff in Venezuela (Deplazes et al., 2013). (F) Tropical temperature changes plotted as a fraction of net glacial-interglacial temperature change. Records from 0-30°N (dashed dark green) and 0-30°S (dashed light green) and the average value of all tropical records (30°N-30°S) plotted together (solid green line) as in Shakun et al. (2012). (G) Rwenzori moraine ages plotted versus the normalized glacier extent down valley relative to the LGM maximum position, as in Figure 4.6. Each circle represents a single moraine age and position, color coded by valley (blue = Bujuku; green = Nyamugasani). (H) Moraine ages from eight previously published studies of tropical South American glacial extents. All data are plotted as for the Rwenzori and color coded by study. (I) South American ^{10}Be ages from nine separate studies. Individual ^{10}Be sample ages are represented by blue bars. Arithmetic mean ^{10}Be moraine ages are represented by black bars.



An alternative hypothesis for tropical climate change during Termination 1 is that tropical temperatures were forced via hemispherically anti-phased, high-latitude abrupt climate events such as the ACR and the YD. During these climate events, the mean annual position of the Intertropical Convergence Zone (ITCZ) shifted towards the ‘warmer’ hemisphere (Deplazes et al., 2013) and may have influenced tropical temperatures. For example, a more southerly ITCZ during the YD would have forced cool and dry northern hemisphere air farther south, encouraging cooling and drying in the northern tropics. However, the timing of the tropical glacial fluctuations does not adhere to a canonical ACR or YD pattern (Figure 4.8.). This suggests that tropical temperatures were not necessarily coupled to the high-latitude processes that influenced the events.

A second, related hypothesis for tropical climate change during Termination 1 suggests that hemispherically anti-phased abrupt warming and cooling (i.e., during the ACR and YD) were ameliorated through increased heat export from the tropics to the ‘cooler’ hemisphere (Weijers et al., 2007). Under this scenario, relatively stable tropical temperatures at ~15-11 ka as inferred from tropical glacial extents may be explained by the atmospheric integration of the hemispherically anti-phased cooling and warming associated with the ACR in the southern hemisphere and contemporaneous Bolling/Allerod period in the northern hemisphere. Although the amelioration of hemispherically anti-phased temperatures by the tropical atmosphere is an intriguing possibility, the expected timing and expression of such a homogenized temperature signal in the tropics is unclear. In addition, evidence that the YD may have been a time of marked seasonality rather than persistent cool conditions in the Northern Hemisphere (Denton et al., 2005; Bromley et al., 2018; Young et al., 2019) further complicates the interpretation of an

‘expected’ tropical temperature signal. Further work is required to test this hypothesis with high-resolution glacial chronologies.

Tropical sea-surface temperatures (SSTs), particularly within the Pacific Ocean, are a primary control on tropical tropospheric temperatures and interannual temperature variability (Sobel et al., 2002) and so may provide another possible explanation for the pattern of tropical temperature changes registered by glacial fluctuations. Glaciers in tropical south America today respond rapidly to shifts in Pacific SSTs (Favier et al., 2004). The Rwenzori are influenced predominantly by air masses sourced from the western Indian Ocean, although the eastern tropical Atlantic exerts an influence on the Rwenzori climate in the Boreal winter (Singerayer et al., 2015). Compilations of low-latitude (30°N-30°S) SSTs indicate warming in the tropical oceans was underway by at least ~19 ka and continued through HS1 before pausing during much of the ACR and YD (Shakun et al., 2012). Tropical SSTs increased throughout HS1 in the eastern Atlantic (Weldeab et al., 2005); eastern and western Indian (Mohtadhi et al., 2014; Romahn et al., 2014; Rippert et al., 2015), and the eastern and western Pacific Oceans (Koutavas et al., 2012). However the magnitude and timing of ACR cooling varies between these sites, as does the onset of post-ACR warming. Moreover, the resolution of many SST records is insufficient to determine the relative timing of tropical glacial fluctuations and tropical SST changes. Although tropical SSTs likely impacted tropospheric temperatures throughout Termination 1, it is not possible to link millennial-scale glacial fluctuations more definitively with tropical SST records at this time.

4.7. Conclusions

A ^{10}Be chronology of glacial extents in the Rwenzori Mountains registers ice retreat during HS1 and ice stabilization before ~15-14 ka, coincident with the early part of the ACR. Recession with intermittent moraine deposition after ~12 ka was followed by rapid retreat of glaciers in multiple catchments during the early Holocene. The Rwenzori glacial chronology is similar to glacial records reported from tropical South America. The similarity of glacial fluctuations across the wider tropics (i.e., tropical South American and Africa) supports the interpretation that temperature was a primary control on tropical glacial mass balance. The tropical glacial chronologies presented and discussed here do not align with high-latitude temperature records, suggesting that tropical temperature changes did not followed a ‘northern’ or ‘southern’ pattern of deglacial warming. Instead the tropics appear to have undergone a unique pattern of deglacial warming. The tropical temperature signal inferred from tropical glacial extent records likely reflects the impacts of multiple factors, including both GHG as well as atmospheric and oceanic forcing. Although the relative influences of these forcing mechanisms on past tropical temperatures is uncertain, the tropical glacial chronology provides important information on the global footprint of deglacial warming and abrupt climate events such as HS1, the ACR, and YD. Future work to elucidate further the timing and magnitude of tropical warming will improve our understanding of the tropics within the wider global climate system and the mechanisms that impact a dynamic source of modern climate variability.

4.8. Acknowledgements

We thank the Uganda National Council on Science and Technology and the Uganda Wildlife Authority for their support of and assistance with this project. We also thank Rwenzori Trekking Services and Rwenzori Mountaineering Services for their safety and logistical support while in the field. This project was supported by grants from the National Science Foundation (EAR-1702293; GSS-1558358), National Geographic Society, the Comer Family Foundation, and Sigma Xi. Satellite imagery was granted by the DigitalGlobe Foundation. This is LLNL-JRNL-XXXX.

CHAPTER 5

¹⁰BE AGES OF GLACIAL EXTENTS IN THE RWENZORI MOUNTAINS AND THEIR IMPLICATIONS FOR HOLOCENE CLIMATE IN EAST AFRICA

M.S. Jackson¹, M.A. Kelly¹, J.M. Russell², A.M. Doughty³, J.A. Howley^{1^}, B. Nakileza⁴,
J.W. Chipman¹, D.A. Cavagnaro¹, and S.H. Zimmerman⁵

¹*Department of Earth Sciences, Dartmouth College, Hanover, NH 03755.*

²*Department of Earth, Environmental, and Planetary Sciences, Brown University,
Providence, RI 02912.*

³*Geology Department, Bates College, Lewiston, ME 04240.*

⁴*Mountain Resource Centre, Makerere University, Kampala, Uganda.*

⁵*Center for Accelerator Mass Spectrometry, Lawrence Livermore National Laboratory,
Livermore, CA 94550.*

[^]*New Hampshire Department of Health and Human Services, Concord, NH 03301
(current address).*

5.1. Abstract

Tropical glaciers are retreating rapidly, threatening freshwater reserves and alpine ecosystems across the low latitudes. Understanding how tropical glaciers responded to past periods of warming is crucial for predicting and adapting to future glacial change, yet relatively little is known about past glacial fluctuations in tropical regions. This is particularly true in the African tropics, where temperatures were as warm as or warmer

than today during the middle Holocene but data regarding the timing and magnitude of Holocene glacial fluctuations in the region are sparse. Here we present twelve new beryllium-10 surface-exposure ages that constrain Holocene glacial extents in the equatorial Rwenzori Mountains, Uganda. These results document rapid early Holocene glacial retreat in two separate Rwenzori catchments, and show that late Holocene deposits mark the greatest expansion of glaciers during the last ~11 ka. Holocene glacial fluctuations elsewhere in tropical Africa and in tropical South America are broadly similar to those in the Rwenzori, with most tropical glaciers retreating rapidly during the early Holocene and remaining near or inboard of their late Holocene positions through much of Holocene time. The coherence of Holocene glacial fluctuations across the tropics implies that low-latitude temperatures responded to a common forcing mechanism, most likely temperature. Tropical sea-surface temperatures and greenhouse gas forcing changes do not align with terrestrial temperature changes during the Holocene. Northern hemisphere summer insolation changes are coherent with changes in tropical glacial extents, but do not align with organic geochemical reconstructions of tropical African temperature. Seasonal changes in equatorial insolation, however, do align with reconstructed temperatures and restricted (i.e., smaller than late Holocene maxima) glacial extents, and may in part explain the patterns of tropical Holocene climate change.

5.2. Introduction

The modern retreat of tropical glaciers is contemporaneous with glacial recession around the globe (Solomina et al., 2015) and is considered emblematic of anthropogenic global warming. This includes glaciers in the African tropics, where ice on the region's

still glacierized Kilimanjaro, Mt. Kenya, and Rwenzori Mountains is in rapid decline (Hastenrath, 1995; Kaser and Osmaston, 2002; Taylor et al., 2006; Thompson et al., 2009; Cullen et al., 2013). The ongoing, coherent recession of glaciers worldwide is apparently unique during the Holocene Epoch (~11.7 ka-present; Walker et al., 2012) (e.g., Solomina et al., 2015). Yet the response of glaciers to prior periods of warming, such as during early Holocene (~11.7-8.2 ka) and middle Holocene (~8.2-4.2 ka) times (Walker et al., 2012), is unresolved, particularly for glaciers in tropical regions. Determining the response of tropical glaciers to past incidences of Holocene warming provides valuable information for assessing whether, or for how long, tropical glaciers may survive under projected future warming scenarios (e.g., Stocker et al., 2013). The sensitivity of tropical glaciers to a warming climate has direct ramifications for the billions of people who live in low-latitude regions and depend upon glacial melt for drinking water and irrigation (Bradley et al., 2006). Understanding the response of these glaciers to past climate regimes is therefore crucial for future climate change mitigation and adaptation efforts.

We present new data that constrain Holocene glacial extents in the Rwenzori Mountains in Uganda (~0.3°N, 30°E; Figure 5.1.). These data comprise glacial geomorphic mapping and twelve beryllium-10 (^{10}Be) surface-exposure ages of glacial landforms in two separate valleys in the Rwenzori Mountains. We compare the Rwenzori glacial extents with records of Holocene glaciation elsewhere in the African and South American tropics in order to assess the potential coherence of regional and wider tropical glacial fluctuations. We also compare these records with local and regional paleoclimate proxy records and assess the potential drivers of past climate changes.

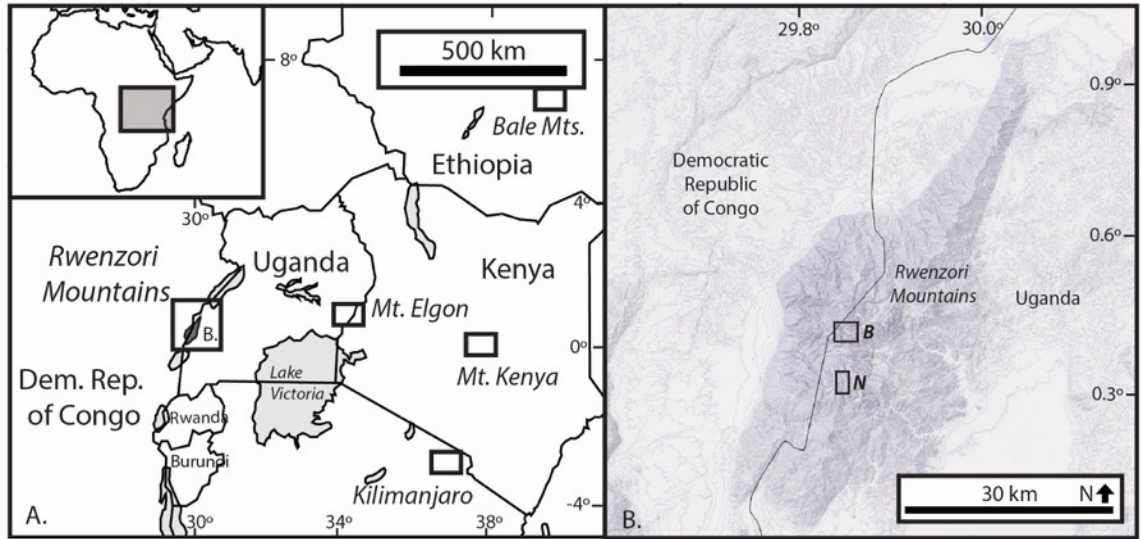


Figure 5.1. (A) Map of East Africa and locations mentioned in the text. (B) The Rwenzori Mountains (right) are on the border between Uganda and the Democratic Republic of Congo. (Right) The Rwenzori Mountains. The Bujuku valley (B) and Nyamugasani valley (N) field sites are boxed in black.

5.3. Prior Work on Tropical African Holocene Glacial Extents

Kenya - Mt. Kenya

Mt. Kenya ($\sim 0^\circ$ N, 37° E, highest peak 5200 m asl; Figures 5.1, 5.2) is perhaps the most well-studied glacial environment in Africa. An extinct volcano and still glacierized today, Mt. Kenya features numerous glacial deposits that range in age from pre-last glaciation to historical time (e.g., Shanahan and Zreda, 2000). The first reported observations of glacial extents on Mt. Kenya are from the late 19th century when glaciers were at or near their late Holocene (~ 4 ka-present) maxima (Gregory, 1894). Between ~ 1900 and 2004 CE the total surface area of glaciers on Mt. Kenya decreased from ~ 1.6 to 0.3 km² (Prinz et al., 2012). Lewis Glacier, the largest remaining ice mass on the peak,

lost ~79% of its total area between 1934 and 2010 CE (Prinz et al., 2012). If ice loss continues at this rate, the Lewis Glacier is predicted to disappear completely by 2030 CE.

Records of earlier Holocene glaciation on Mt. Kenya are based on radiocarbon dating of lake sediments and surface-exposure dating of glacial deposits. In the eastward trending Hogley Valley, bracketing radiocarbon ages of sediments in a core from the moraine-dammed Thomson Tarn (4260 m asl) indicate that the moraine dam was formed between ~7.1 and 6.2 cal yr BP (Perrott, 1982). In the southward trending Teleki Valley, radiocarbon ages of sediments in a core from the moraine-dammed Naro Moru Tarn (4200 m asl) provide a minimum-limiting age of ~4.7 cal kyr BP for the moraine dam (Johansson and Holmgren, 1985). In the same core, another radiocarbon age of organic material from a gravel-rich horizon stratigraphically below the sediment dated at ~4.7 cal kyr BP is ~6.9 cal kyr BP. If correlative with the moraine dam, the older age may provide a maximum-limiting age for the moraine dam (Johansson and Holmgren, 1985).

Karlen et al. (1999) analyzed sediment cores from Naro Moru Tarn and Hausberg Tarn (4370 m asl; Hausberg Valley). Using the radiocarbon ages from Johansson and Holmgren (1985) and the amounts of clastic sediment input to Hausberg Tarn, Karlen et al. (1999) argued for expanded glaciers on Mt. Kenya before ~5.7 cal kyr BP. Karlen et al. (1999) also suggested that glaciers on Mt. Kenya were dynamic during the middle and late Holocene, with multiple periods of advance and retreat over the last ~5 ka. In contrast, Mahaney (1989) used analyses of soil facies to argue that multiple presumed-Holocene moraines on the flanks of Mt. Kenya, including the moraine that dams Naro Moru Tarn, reflect standstills during overall Holocene glacial retreat rather than significant readvances. Based on these interpretations, Mahaney (1989) suggested a

largely ice-free Mt. Kenya for most of the Holocene with only minor late Holocene fluctuations after ~1 ka.

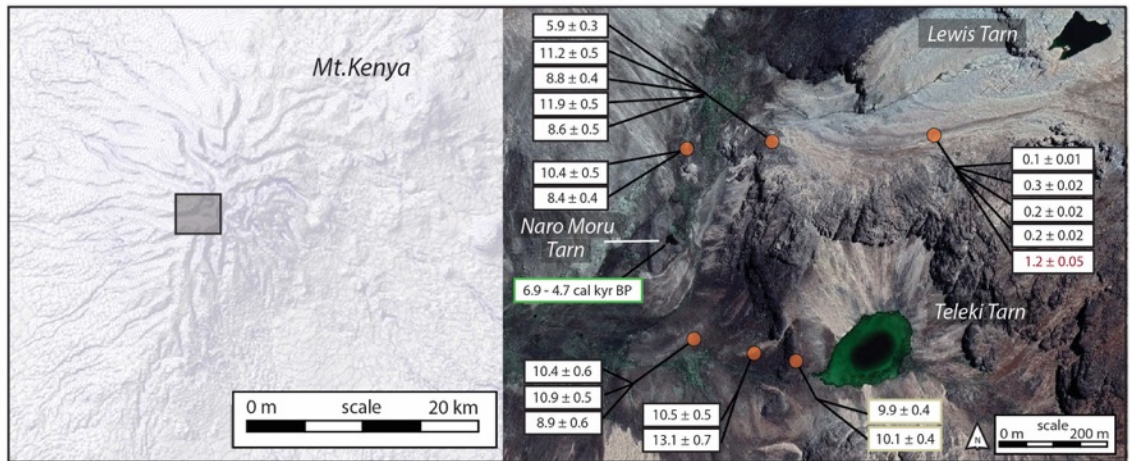


Figure 5.2. Evidence for Holocene glaciation on Mt. Kenya. Black boxes denote ^{36}Cl ages of boulders on moraines. Beige boxes are ^{36}Cl exposure ages of bedrock (all ^{36}Cl ages are from Shanahan and Zreda, 2000). Bracketing radiocarbon ages from Naro Moru Tarn are boxed in green (Johanssen and Holmgren, 1985).

Shanahan and Zreda (2000) used chlorine-36 (^{36}Cl) surface-exposure dating to date directly moraines on Mt. Kenya. However, uncertainties in the ^{36}Cl production rate and large standard deviations of the ^{36}Cl ages make interpretations of this dataset challenging. In general, the ^{36}Cl ages of moraines suggest restricted (i.e., smaller than late Holocene maxima) glacial extents during much of the Holocene. Two Holocene moraines immediately outboard of Teleki Tarn (~4300 m asl) contains ^{36}Cl concentrations equivalent to ~10 ka of exposure (Figure 5.2.). Two moraines immediately outboard of the Teleki Tarn bedrock date to ~ 10 ka. In a separate catchment, two lateral moraines (Liki III deposits) are dated to ~10 ka. Both moraines were deposited by ice fed partially

by an expanded Lewis Glacier. Up valley of these moraine ridges, four ^{36}Cl ages of boulders on a lateral moraine deposited by the Lewis Glacier yield an arithmetic mean age of 0.21 ± 0.1 ka. The Naro Moru Tarn occurs between the Liki III deposits and the ~ 0.21 ka moraine. However, the moraines that dam the Naro Moru and Thomson Tarns (Perrott, 1982) are not dated directly using surface-exposure dating.

Tanzania - Kilimanjaro

Kilimanjaro ($\sim 3^\circ\text{S}$, 37°E , highest peak 5900 m asl; Figure 5.1.) is an extinct volcano and features glacial deposits that range in age from LGM to historical time (Shanahan and Zreda, 2000). The areal extent of ice on Kilimanjaro decreased from ~ 12.1 km² in 1912 CE to ~ 1.9 km² in 2007 CE, a loss of $\sim 85\%$ of the mountain's ice cover (Thompson et al., 2009). If this rate of ice loss continues, Kilimanjaro glaciers may disappear entirely by 2030 CE (Thompson et al., 2009), although some suggest that ice may persist until 2060 CE (Cullen et al., 2013). There are no radiocarbon or surface-exposure ages of Holocene glacial extents on Kilimanjaro. Although multiple studies show that Kilimanjaro's ice cap has become less extensive over the last ~ 1.0 ka, the duration of ice cover on the mountain is debated (Kaser et al., 2010; Thompson et al., 2011; Noell et al., 2014). Based on a comparison of the Kilimanjaro ice core $\delta^{18}\text{O}$ record with $\delta^{18}\text{O}$ records from eastern Mediterranean speleothems (Bar-Matthews et al., 1999), Thompson et al. (2002) suggest an ice-cap age of at least ~ 11.7 ka. This would imply that the ice cap persisted throughout the Holocene (Thompson et al., 2002). In contrast, other studies argue that the ice cap disappeared and re-nucleated multiple times during the Holocene. Kaser et al. (2010) used modern mass balance observations to suggest that

the modern ice cap formed only at ~0.8 ka. Radiocarbon ages of soils and dust in and near Kilimanjaro's Northern Ice Field are interpreted as indicating that the margins of the modern ice cap formed recently (~1.0 ka) and that ice on the central plateau may be much older (Noell et al., 2014). Subsequent radiocarbon dating of dust horizons in the Northern Ice Field suggests that the ice cap has accumulated mass for the last ~4 ka, with at least some period of net ablation prior to this time and net ablation underway today (Gabielli et al., 2014).

Ethiopia

A radiocarbon age of bog sediments at ~4130 m asl on Mt. Bada in the Ethiopian Arsi Mountains (7°N, 39°E; 4195 m asl) indicates that ice retreated up valley of the bog by ~13.3 cal kyr BP (Hamilton, 1982). Similarly, in Ethiopia's Bale Mountains (6°N, 39°E; highest peak 4,377 m asl), radiocarbon ages of sediment cores from the formerly glacially fed Lake Garba Guracha (~3,950 m asl) near the peak of Mt. Batu (~4,370 m asl) indicate the catchment was likely ice free by ~11.8 cal kyr BP and remained so throughout the Holocene (Tiercelin et al., 2008).

Uganda

Mt. Elgon

The timing and rate of post-LGM deglaciation of Mt. Elgon (~1°N, 34°E, 4,321 m asl), in eastern Uganda, is not known (Kaser and Osmaston, 2002). Two radiocarbon ages of sediments in cores from Lake Kilimilli (4,150 m asl) indicate that ice had retreated

upslope on Mt. Elgon by at least ~12.9-12.6 cal kyr BP (Hamilton and Perrott, 1978). No further data exists regarding Holocene ice extents on the peak.

Rwenzori Mountains

The Rwenzori Mountains (~0°N, 30°E, highest peak 5109 m asl) are an uplifted horst of crystalline bedrock that occur on the border between Uganda and the Democratic Republic of Congo (Figure 5.1). The first quantitative observations of glacial extents in the Rwenzori were made in the early 20th century by the Duke of Abruzzi (Abuzzi, 1907). The glaciers have since undergone marked retreat, with a decrease in area from ~6.5 to 0.96 km² between 1906 and 2003 CE, and an estimated 50% loss in the areal ice extent between 1987 and 2003 CE (Taylor et al., 2006). Clastic sediment input to Rwenzori lakes indicates that the recent glacial recession was underway by at least 1870 CE (Russell et al., 2009). Today glaciers occur above ~4400 m asl on the slopes of Mt. Stanley, Mt. Baker, and Mt. Speke. These glaciers are predicted to disappear within the coming decades (Kaser and Osmaston, 2002; Taylor et al., 2006).

Records of earlier Holocene glacial extents in the Rwenzori Mountains are based on relative age dating and lichenometry (Osmaston, 1989; Bergström, 1955), as well as on radiocarbon ages of lake sediments (Livingstone, 1967). Osmaston (1989) classified moraines into distinct glacial stages based on their relative weathering and morphology. The so-termed Lac Gris stage moraines are predominantly low-relief (~1-2 m high) features that occur within ~100 m of the 1906 CE ice extents and are estimated to be ~700-100 years in age (Osmaston, 1989). Bergström (1955) used lichenometry to estimate that Lac Gris moraines near the margin of Elena Glacier on Mt. Stanley date to

~1750 CE. However, the rate at which lichen colonizes rock surfaces in the Rwenzori is unconstrained (Osmaston, 1989). In the Butahu valley, a radiocarbon age of the lowermost organic sediments in a core from Upper Lake Kitandara (~4000 m asl) is ~7.7 cal yr BP (Livingstone, 1967) provides a minimum-limiting age for deglaciation of the lake basin. In the Bujuku valley, one radiocarbon age of gravel-rich peat in a core from Lake Bujuku (3,920 m asl) provides a minimum-limiting age (~3.1 cal yr BP) of ice recession (Livingstone et al., 1967). However this radiocarbon age is not a basal age of the lake and, therefore, the age likely underestimates the time of deglaciation past this site. Later surface-exposure dating of a landslide deposit that dams the outlet of Lake Bujuku indicates that the landslide was emplaced at ~11.0 ka (Chapter 4), suggesting that ice had receded up valley of Lake Bujuku by at least ~11.0 ka.

Outboard of Lac Gris stage deposits are Omurabaho stage moraines. These moraines are ~3-30 m in relief above the valley floors and occur at elevations ~3600-4000 m asl (Osmaston, 1989). The quartz-bearing lithology of the Rwenzori is unique among the glaciated mountains of tropical Africa (Kaser and Osmaston, 2002) and enables the application of surface-exposure dating using the cosmogenic nuclide beryllium-10 (hereinafter ^{10}Be dating). ^{10}Be dating of Omurabaho stage moraines in the Bujuku and Nyamugasani valleys indicates that these deposits are late glacial and early Holocene in age (~15-11 ka, Chapter 4).



Figure 5.3. (top) The three still glacierized peaks in the Rwenzori Mountains. Photo taken from the peak of Mt. Weisman at the head of the Nyamugasani valley, view is to the north. (lower left) The unoccupied cirque floor at the head of the Nyamugasani valley, with a view to the south and the lower reach of the valley. (lower right) The right-lateral rampart moraine in the upper Bujuku valley on the southern slope of Mt. Speke. View is to the west.

Summary of Tropical African Holocene Glacial Extents

As a whole, evidence from tropical Africa suggests restricted glaciers during much of the Holocene. Radiocarbon ages from lake sediments in the Ethiopian Highlands and on Mt. Elgon indicate that glaciers were either very small or had disappeared completely by the earliest Holocene (Hamilton and Perrot, 1982; Tiercelin et al., 2008). In Tanzania, ice-core analyses and radiocarbon dating suggest a period of net ablation of Kilimanjaro's ice cap prior to ~4 ka, followed by accumulation during the late Holocene (Gabrielli et al, 2014).

In contrast, data from Mt. Kenya have been interpreted to show evidence for a significant (i.e., larger than late Holocene maxima) glacial advance during middle Holocene time. ^{36}Cl ages of moraines on Mt. Kenya indicate that glaciers in the Teleki Valley retreated from their early Holocene maxima by ~10 ka and that Lewis Glacier reached a late Holocene maximum ~200 years ago (Shanahan and Zreda, 2000). However, bracketing radiocarbon ages of the Naro Moru Tarn moraine dam, inboard of the ~10 ka ice position and ~250 m down valley from the ~200 year old Lewis Glacier moraine, suggest that the moraine dam was emplaced between ~6.9 and 4.7 cal kyr BP (Johansson and Holmgren, 1985; Karlen et al., 1999). Although disputed (i.e., Mahaney, 1989), these data suggest a middle Holocene glacial advance occurred in the Teleki Valley that extended ~420 m down valley from the late Holocene ice extent. In addition, radiocarbon ages from Thomson Tarn in the Hogley Valley indicate a glacial advance at some time between ~7.1-6.2 cal kyr BP (Perrot, 1982).

Recent work mapping and dating glacial extents in the Rwenzori Mountains has yielded important information on the timing of glacial fluctuations during the LGM and

subsequent deglaciation (Kelly et al., 2014; Jackson et al., submitted), but little is known about Holocene glacial extents. Inboard of ^{10}Be dated Omurabaho moraines (~15-11 ka; Jackson et al., in prep), the radiocarbon ages from Upper Lake Kitandara (~7.7 cal yr BP, Livingstone, 1967) and Lake Bujuku (~3.1 cal yr BP, Livingstone, 1967) are the only numerical ages that constrain Holocene glacial retreat prior to the first recorded observations of Rwenzori glaciers in the early 20th century. Whether Rwenzori glaciers were within their late Holocene extents by early Holocene time or, instead, if they experienced significant readvances prior to late Holocene time is unknown. This study aims to establish the timing of changes in glacial extents in the Rwenzori and to compare this pattern with Holocene glacial extents elsewhere in tropical Africa and in tropical South America.

5.4. Study Sites

We focused our investigation on glacial extents in the Bujuku and Nyamugasani valleys, two independent catchments in the Rwenzori (Figures 5.1, 5.3).

Bujuku Valley

Lac Gris stage deposits occur at the head of the Bujuku valley at ~4000-4500 m asl on the southern slope of Mt. Speke (Osmaston, 1989), one of three still-glacierized peaks in the Rwenzori. Scrub vegetation and bare bedrock dominate in the Rwenzori above ~4000 m asl (Osmaston, 2006; Bauer, 2010), and much of Mt. Speke is free of vegetation above this elevation save for patchy mosses and lichens that cling to bedrock surfaces. Speke Glacier occupies the south-facing peak of Mt. Speke. Although today the

glacier terminus occurs at ~4600 m asl, in 1958 CE the glacier extended down slope to an elevation of ~4350 m asl (Whittow et al., 1963) (Figure 5.4). An unoccupied Lac Gris stage moraine occurs ~300 m downslope (~4040 m asl) from the 1958 CE glacial extent. Although the age of this moraine is unknown, the moraine had been abandoned by ice prior to 1906 CE (Abruzzi, 1907).

Down valley from the Lac Gris stage moraines, Omurabaho stage moraines occur between ~3400 and 3700 m asl. ^{10}Be dating of these moraines shows that the innermost moraine is ~11.7 ka ('Bujuku 0' moraine; Jackson et al., in prep). No moraines occur between the ~11.7 ka moraine and the Lac Gris stage deposits. As described above, a radiocarbon age of Lake Bujuku sediments indicates that the lake was ice-free by at least ~3.1 cal kyr BP (Livingstone, 1967). However, the age is not from basal sediments and is significantly younger than ^{10}Be ages of boulders on a landslide deposit (~11.0 ka) near the outlet of the lake (Chapter 4). Because the landslide shows no evidence of having been impeded or reworked by ice, it must have been emplaced after the former Bujuku glacier retreated from this portion of the valley. For this reason, it is likely that the radiocarbon age from Lake Bujuku underestimates the timing of ice recession past this site.

Nyamugasani Valley

Mt. Weisman, located at the head of the Nyamugasani valley, is not currently glacierized but aerial photography and observations show that the peak was ice covered until the middle 20th century by the former Thomson Glacier (Meader, 1934; Osmaston, 1965). Omurabaho stage moraines occur down valley between ~3800 and 4000 m asl and

some of these moraines dam lakes. The innermost moraine dams Lake Bigata and is ^{10}Be dated to ~ 11.2 ka ('Nyamugasani 0' moraine; Chapter 4). No moraines occur inboard of the ~ 11.2 ka moraine, although perched boulders are ubiquitous on the valley floor inboard of the Omurabaho stage moraines. Inboard of the ~ 11.2 ka moraine, the Nyamugasani valley branches into two distinct reaches. The more western reach is blanketed by scrub vegetation and is bounded by steep, faulted bedrock walls. The eastern reach is less vegetated and bare bedrock dominates the valley floor.

5.5. Methods

We conducted fieldwork during three expeditions in the Rwenzori during the summers of 2012 and 2016 and winter of 2015. In the field we classified glacial-geomorphic features based on their degree of weathering and morphology and mapped these features onto WorldView-1 0.5 m resolution satellite imagery. We collected samples for ^{10}Be dating from boulders on moraines, perched boulders, and bedrock using a hammer and chisel and the drill-and-blast method of Kelly (2003). We took care to sample boulders that were not influenced by post-depositional movement and, where possible, surfaces with no dip in order to minimize topographic shielding correction uncertainties. We recorded sample locations with a handheld GPS (± 3 m vertical, ± 1 m horizontal), determined topographic shielding using a clinometer and measured sample surface dip and dip direction with a compass.

After measuring the thickness of each sample, we crushed the samples and used the 250-710 micron size fraction for beryllium chemistry. We isolated beryllium from each whole-rock fraction and associated process blanks using a modified version of the

methods described in Schaefer et al. (2009). All $^{10}\text{Be}/^9\text{Be}$ ratios were measured at the Lawrence Livermore National Laboratory Center for Accelerator Mass Spectrometry (LLNL CAMS) and normalized to the 07KNST3110 standard (Nishiizumi et al., 2007). ^{10}Be ages presented here are calculated using version 3 of the online calculator described by Balco et al. (2008 and subsequently updated) with a high-altitude, low-latitude production rate (Kelly et al., 2015) and time-invariant scaling framework (“St” scaling; Lal, 1991; Stone, 2000)(Table C1). We also present ^{10}Be ages calculated using alternative scaling frameworks (Table C1), although we note that our choice of scaling framework does not alter our overall interpretations.

We did not correct ^{10}Be ages for the potential impacts of vegetation or snow cover. Vegetation in the Rwenzori Mountains is sparse above ~4000 m asl (Foster et al. 2001; Bauer et al., 2010). Some samples had a patchy cover of lichen or moss (≤ 2 cm thick) and we avoided this where possible. Snow does not persist for any length of time at the sample elevations due to warm daytime temperatures and intense solar radiation. We also did not correct ^{10}Be ages for the potential influence of erosion as samples did not feature raised quartz veins or other evidence that could be used to estimate rock surface erosion rates. Previous applications of ^{10}Be dating in the Rwenzori suggests that raised quartz veins and rock surfaces on single moraine crests yield statistically similar ages (Chapter 3).

5.6. Results

Our results include twelve new ^{10}Be ages of glacial features in the Bujuku and Nyamugasani valleys (Table C1). The ages are of boulders on moraines, perched boulders on bedrock, and glacially-scoured bedrock.

Bujuku valley

In order to assess Holocene ice extents in the Bujuku valley, we ^{10}Be dated the first glacial deposit located up valley of the late-glacial-age (i.e., 11.7 ka) Bujuku 0 moraine (Chapter 4). This glacial deposit is a Lac Gris stage rampart moraine on the south-facing slope of Mt. Speke, ~2.5 km up valley of the Bujuku 0 moraine and previously described by Whittow (1963) and Osmaston (1989). We term this Lac Gris stage moraine a “rampart” moraine because it has steep ice-contact slopes and more gently sloping, fan-like, ice-distal slopes. The right- and left-lateral rampart moraines are well preserved and, together, these outline a nearly continuous former ice margin that is dissected by a small stream. The rampart moraine likely formed as rock-fall debris from the steep slopes of Mt. Speke was deposited on the surface of the former Speke Glacier and transported to the ice margin. The existing hollow up slope of the moraine marks the former down-slope extent of Speke Glacier. Four samples from the crest of the right-lateral moraine yield ^{10}Be ages between ~0.45 and 0.27 ka (RZ-12-21, 22, 24, 25).

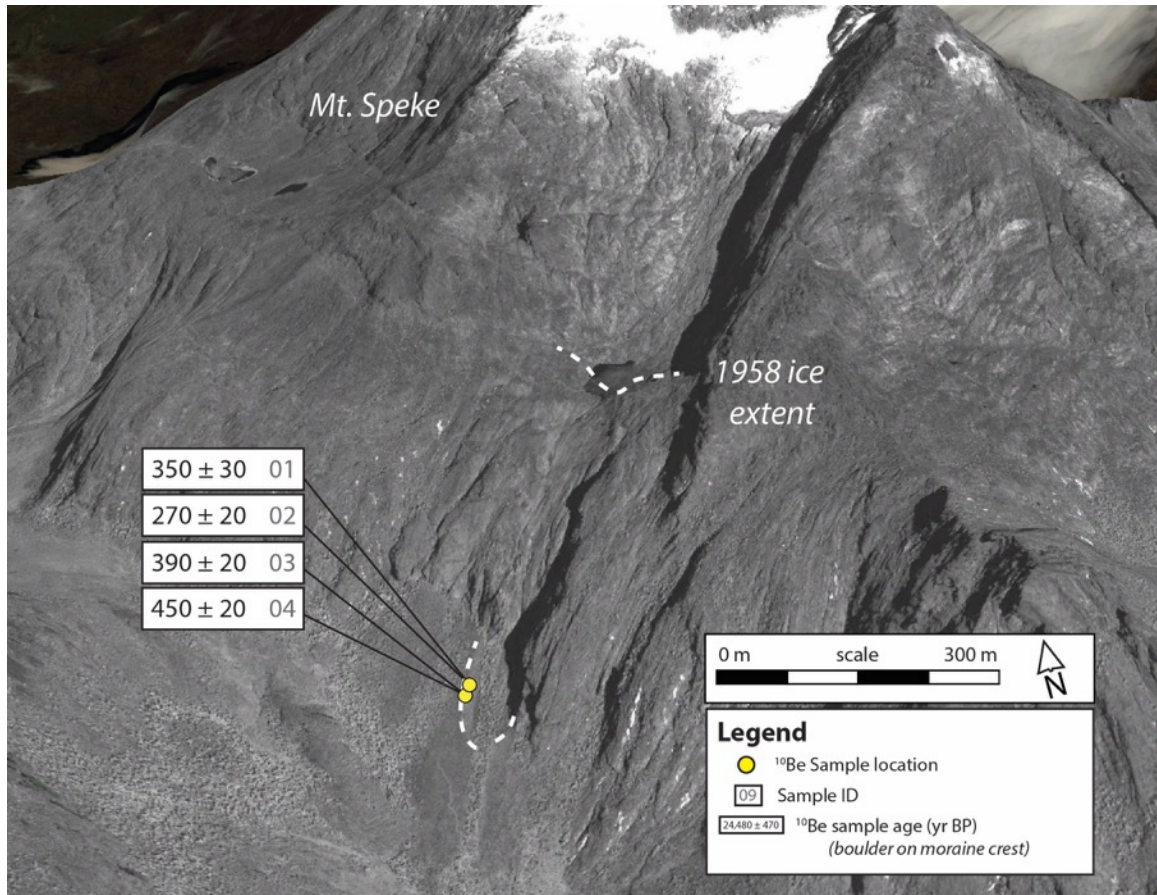


Figure 5.4. ¹⁰Be ages of the rampart moraine on the south-facing slope of Mt. Speke at the head of the Bujuku valley. Ice extent in 1958 is dashed (Whittow, 1963), and the rampart moraine crest is highlighted in dashed white. Map image is a 0.5 m-resolution Worldview-1 satellite image draped over a 30 m digital elevation model.

Nyamugasani valley

In order to assess the timing of ice recession in the Nyamugasani valley up valley of the early Holocene-age (i.e., ~11.2 ka) Nyamugasani 0 moraine (Chapter 4), we sampled perched boulders on bedrock and bedrock along a transect that extends from 4397 to 4536 m asl on the south-facing slope of Mt. Weisman in the upper eastern reach of the valley (Figures 5.5a, 5.5b). We were careful to avoid areas where boulders may have been deposited on the valley floor by rockfall. We also did not sample boulders on steep slopes that could have enabled post-depositional rolling or downslope movement of the boulders.

The two most down-valley samples yield ^{10}Be ages of 12.1 ± 0.1 ka (RZ-15-10) and 11.4 ± 0.1 ka (RZ-15-11). A third sample ~170 m up valley (+30 m elevation) dates to 10.9 ± 0.1 ka (RZ-15-09). One quarter kilometer up valley (+60-70 m elevation) from sample RZ-15-09, two perched boulders on bedrock knobs yield ages of 4.5 ± 0.0 ka (RZ-15-07) and 6.5 ± 0.1 ka (RZ-15-08), respectively. Three bedrock samples from the floor of a cirque below Mt. Weisman (~4500 m asl) contain ^{10}Be concentrations that range between 1.66 and 1.89×10^5 atoms/gram (quartz), equivalent to ~5.0-5.7 thousand years of exposure (RZ-15-01, 02, 03; Table C1).

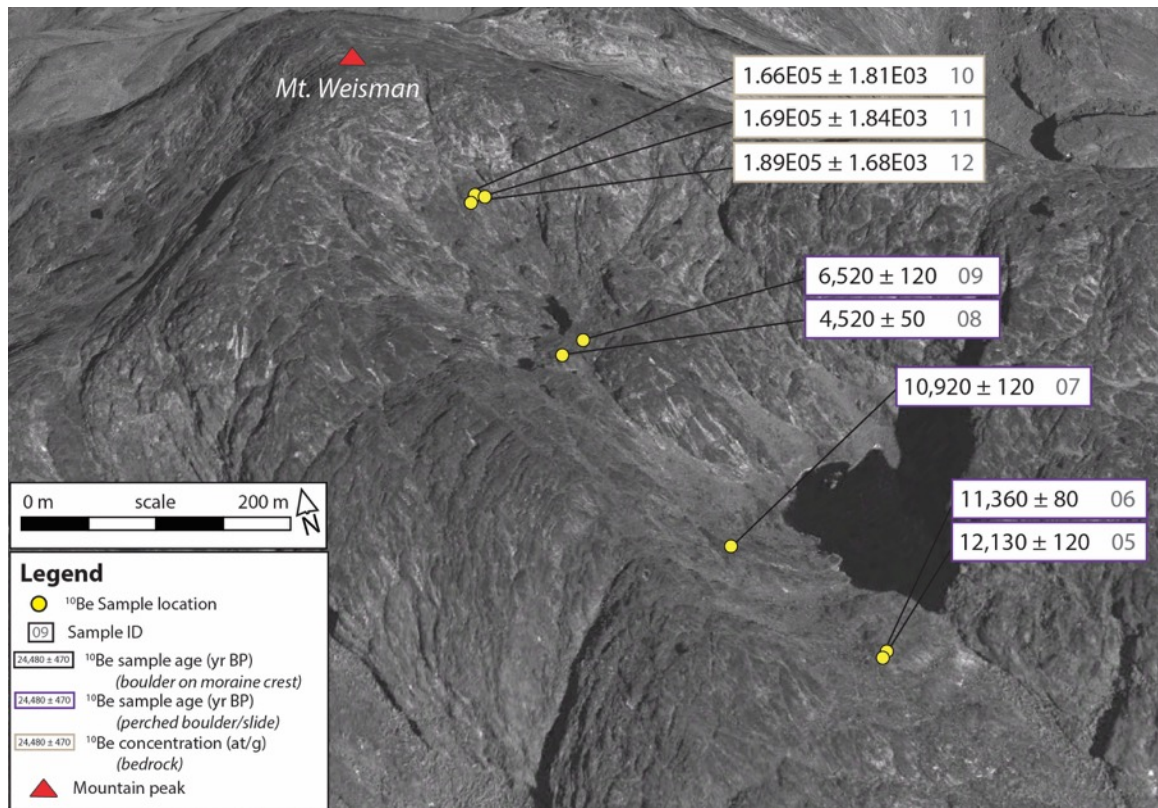


Figure 5.5a. ¹⁰Be ages in the Nyamugasani valley. Ages of perched boulders (samples RWZ-15-07, 08, 09, 10, 11) are boxed in purple. Samples RWZ-15-01, 02, 03 (boxed in beige) are bedrock samples presented as ¹⁰Be concentrations (atoms/gram quartz) accrued over multiple periods of exposure when the site was ice free during the Holocene. Map image is a 0.5 m-resolution Worldview-1 satellite image draped over a 30 m digital elevation model.

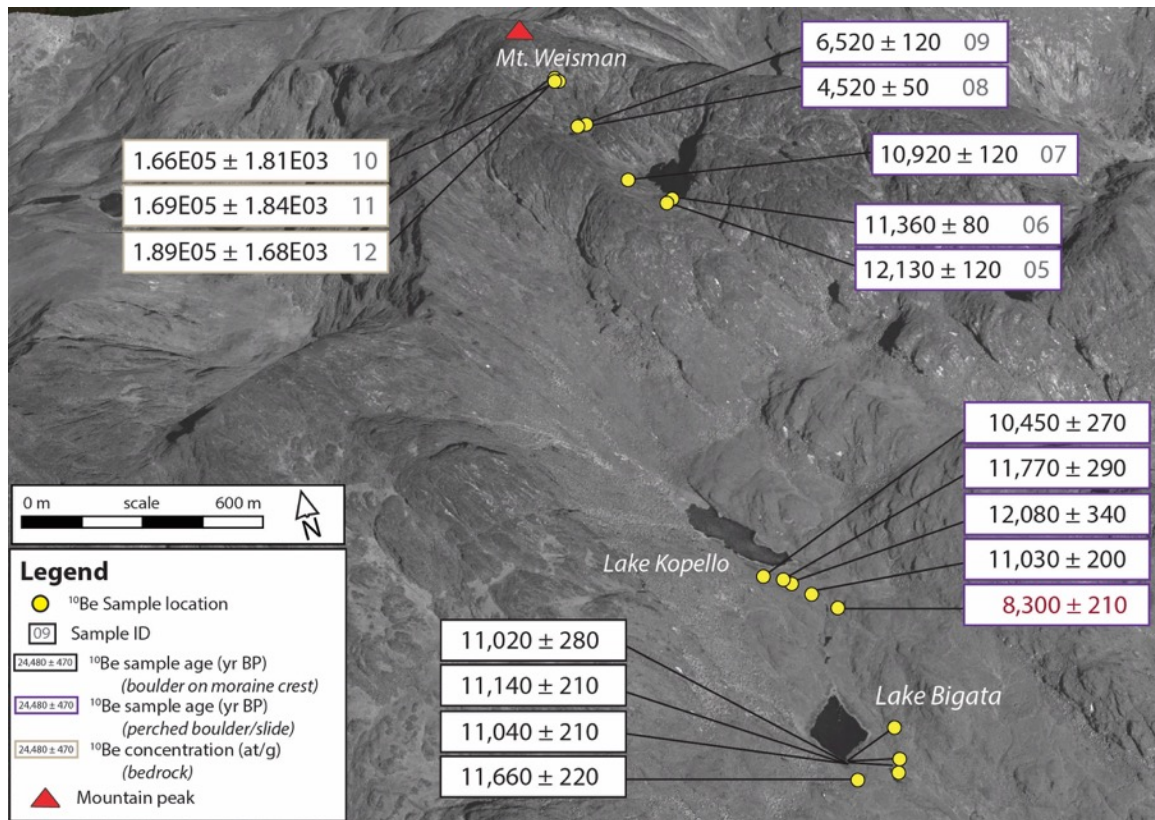


Figure 5.5b. ¹⁰Be ages in the Nyamugasani valley, including previously reported ages from the Nyamugasani 0 moraine that dams Lake Bigata and from perched boulders near Lake Kopello (Chapter 4). ¹⁰Be ages of perched boulders (samples RWZ-15-07, 08, 09, 10, 11) are boxed in purple. Bedrock samples RWZ-15-01, 02, 03) are boxed in beige and presented as ¹⁰Be concentrations (atoms/gram quartz) accrued over multiple periods of exposure when the site was ice free during the Holocene. Gray text denotes the sample ID number listed in Tables 1-3. Map image is a 0.5-m resolution Worldview-1 satellite image draped over a 30 m digital elevation model.

5.7. Discussion

5.7.1. Rwenzori Glacial Extents During the Holocene

Ice retreated rapidly up the Bujuku valley after depositing the Bujuku 0 moraine at ~11.7 ka (Chapter 4.). This rapid ice retreat is supported by ^{10}Be ages (~11.0 ka) of boulders on a landslide that dams the modern Lake Bujuku located ~1.5 km up valley from the ~11.7 ka moraine. No moraines occur between the landslide and the Lac Gris stage rampart moraine on the south-facing slope of Mt. Speke. There is no evidence for glacial reworking this or other rockfall deposits on the valley floor between Lake Bujuku and the Lac Gris stage rampart moraine. However, it is possible that glacial deposits on the valley floor were covered by younger rockfall deposits and, therefore, are not included in our surficial mapping.

The ^{10}Be ages of the Lac Gris stage rampart moraine indicate that the Speke glacier reached its maximum late Holocene extent during the last ~500 years. The older ^{10}Be ages (450 and 390 yrs ago) may reflect the presence of ^{10}Be produced during prior periods of exposure (i.e., inherited ^{10}Be) in the boulder surfaces. The rampart moraine is outboard of the 1906 CE glacial extent which occurs ~300 m upslope (Abruzzi, 1907). Photos taken in 1906 CE show a small accumulation of snow or ice in the uppermost portion of the depression upslope of the rampart moraine, which may have been snow or ice (avalanche) from the above-lying steep slopes or Speke Glacier. Photos of the rampart moraine taken in 1958 CE show no such snow accumulation (Whittow et al., 1963).

Ice retreated rapidly up the Nyamugasani valley after depositing the ~11.2 ka Nyamugasani 0 moraine (Chapter 4) as documented by ^{10}Be ages of perched boulders atop a bedrock ridge near the outlet of Lake Kopello (~12.1-10.5 ka; located at ~4020 m

asl; Jackson et al., in prep.) and from the lowest elevation part of the transect below Mt. Wiseman (~12.1-10.9 ka, located at ~4400-4430 m asl). Some of these ^{10}Be ages are older than the ^{10}Be ages of well-dated moraines down valley (Chapter 4) and, thus, are out of stratigraphic order. We suggest that these perched boulder surfaces likely contain inherited ^{10}Be . Because the glacier was relatively small and thin, and the boulders transported only short distances (< 1.7 km), there may have been insufficient sub-glacial erosion to remove pre-existing ^{10}Be in boulder. Therefore, the youngest ^{10}Be ages (~11.4 and 10.9 ka) are most representative of the timing of ice recession. These ages show that the upper reach of the valley (at least to ~4430 m asl) was ice free by early Holocene time.

Farther up the valley (at ~4490 m asl), two ^{10}Be ages of perched boulders are ~4.5 and ~6.5 ka. These ages may indicate that ice persisted at this elevation until the middle Holocene or, perhaps, that ice readvanced to this location during middle Holocene time. Because the ^{10}Be ages of the perched boulders are similar to the cirque bedrock ^{10}Be exposure-age equivalents (~5.0-5.7 ka), we suggest that the ~4.5 and ~6.5 ka boulders may contain inherited ^{10}Be . In this scenario, the boulders would have been plucked from or from near the cirque floor and transported and deposited by Thompson Glacier with little-to-no boulder surface erosion during the late Holocene. Due to the uncertain transport and depositional history of these samples, we refrain from drawing conclusions using their ^{10}Be ages.

Roughly 10-20 m above the perched boulders, three samples of bedrock on the cirque floor yield ^{10}Be concentrations of $1.66\text{-}1.89 \times 10^5$ atoms/gram of quartz. These ^{10}Be concentrations are equivalent to ~5.0-5.7 ka of exposure. Based on the aerial

photography of Meader (1937) and direct observations of the former Thomson Glacier (e.g., Whittow, 1963), the cirque floor was covered by ice or snow until at least the late 1930s (Figure 5.6). Therefore, we suggest that the ^{10}Be concentrations in the bedrock register the time of exposure since the last time the bedrock surfaces were eroded sufficiently to remove inherited ^{10}Be . It is likely that ice cover during the LGM and late-glacial time was thick and erosive enough to have removed all ^{10}Be from the bedrock surfaces. Therefore, the ^{10}Be concentrations reflect the total period of exposure and any erosion of the bedrock surfaces subsequent to ~ 11.2 ka.

Overall the ^{10}Be ages from the Bujuku and Nyamugasani valleys provide evidence for rapid ice retreat during the early Holocene. Subsequent to this, ice remained at or inboard of its early 20th century extent until latest Holocene time (i.e., the Lac Gris stage moraine dated at ~ 0.46 and 0.27 ka; ~ 1560 - 1750 CE). The results do not preclude that glaciers on the high Rwenzori peaks persisted throughout Holocene time. However, they indicate that glaciers in the Bujuku and Nyamugasani valleys did not experience a significant readvance (i.e., beyond the late Holocene ice extent) during early or middle Holocene time.

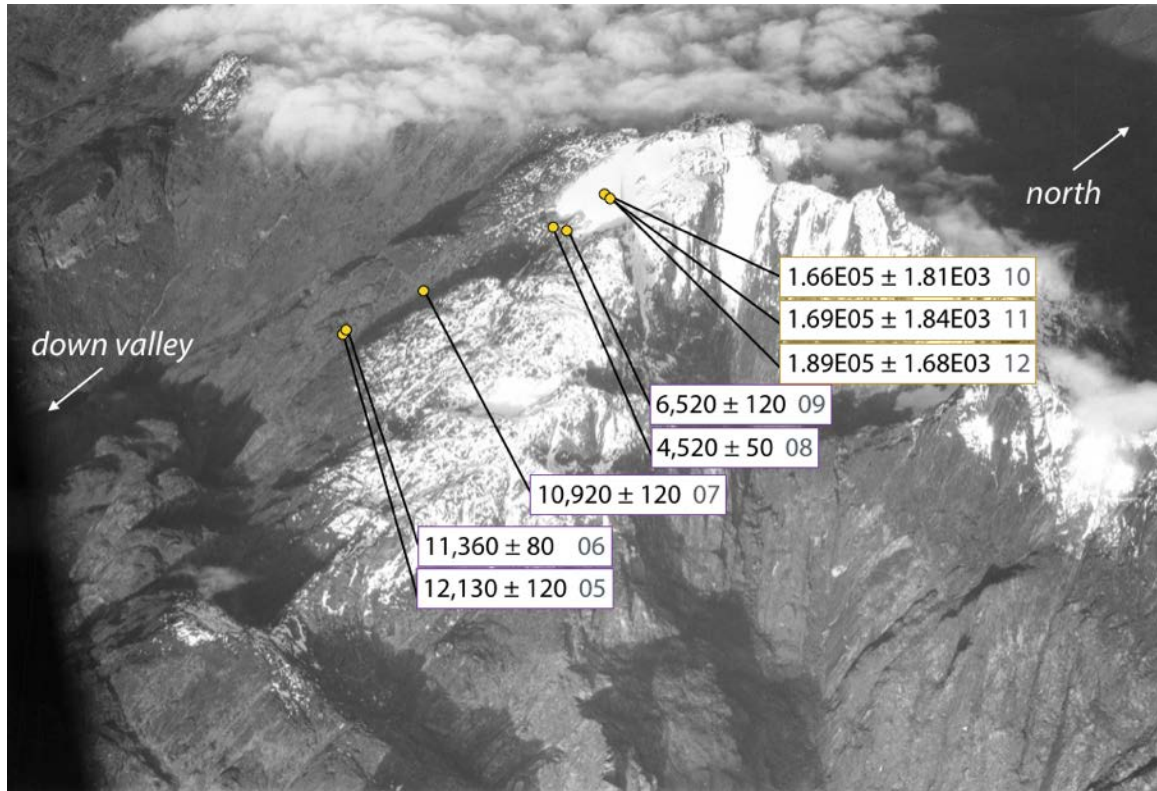


Figure 5.6. Aerial photo of Mt. Weisman and the former Thomson glacier in 1937. Locations of samples and ^{10}Be ages of perched boulders (outlined in purple) and ^{10}Be concentrations from bedrock (outlined in beige) are plotted on the image. The location of the three bedrock samples (RZ-15-01, 02, 03) from the cirque floor are covered by snow or ice. Photo is by Mary Meader, 1937, from the American Geographical Society Library, University of Wisconsin-Milwaukee.

5.7.2. Holocene Glacial Fluctuations Across the Global Tropics

The pattern of Holocene glacial extents in the Rwenzori documented here is generally consistent with glacial histories elsewhere in East Africa. In Ethiopia, Tanzania, Uganda, and Kenya, glaciers retreated either during or prior to the early Holocene. At sites where glaciers persisted through the Holocene, ice remained near or inboard of its late Holocene extent. Although there is evidence for middle Holocene glacial readvances on Mt. Kenya (at ~7.1-6.2 and ~6.9-4.7 cal kyr BP; Perrot, 1982; Johansson and Holmgren, 1985), there is no evidence for such readvances elsewhere in the region. After ~5 ka, increased clastic sediment input to glacially fed lakes on Mt. Kenya suggests dynamic glacier margins during middle and late Holocene time (Karlen et al., 1999), although ice remained inboard of its late Holocene extent.

Holocene tropical South American glacial chronologies are remarkably similar to those from tropical Africa. In the northern and southern tropical Andes, glaciers retreated from their early Holocene positions by at least ~10 ka (e.g., Jomelli et al., 2014). Glaciers then remained near or within their late Holocene extents throughout the majority of Holocene time. ¹⁰Be ages of boulders on moraines indicate that tropical Andean glaciers advanced after ~2-1 ka (Solomina et al., 2015), although many glaciers reached their late Holocene maximum positions in the last ~700-500 years (Smith et al., 2011; Jomelli et al., 2014; Licciardi et al., 2009; Stansell et al., 2017; Stansell et al., 2015). Analyses and radiocarbon dating of clastic sediment in glacially fed lakes, however, indicate that tropical Andean glaciers fluctuated throughout the Holocene, and were particularly dynamic after ~5 ka (e.g., Rodbell et al., 2008). For example, lake sediment records from sites in the Eastern Cordillera and Cordillera Blanca of Peru indicate that glaciers

advanced and retreated multiple times over the last ~10 ka, with more advanced glacial positions at ~4-2 ka (Stansell et al., 2015; 2017). ^{10}Be ages and geomorphic mapping of moraines from these same sites suggest that glaciers generally remained inboard of their late Holocene maxima until at least ~1 ka (Stansell et al., 2015; 2017). Altogether these data suggest that, after a period of early Holocene retreat, tropical South American glaciers were dynamic after ~5 ka but did not extend past their late Holocene maximum positions until the last ~1 ka.

5.7.3. Drivers of Tropical Glaciation During the Holocene

The similarity of Holocene glacial fluctuations across the tropics is consistent with the hypothesis that a pan-tropical forcing mechanism or mechanisms influenced the glacial extents. Although tropical glaciers are sensitive to various factors including precipitation, humidity, aspect, and hypsometry, glaciers in the ‘humid’ inner tropics (~10°N-10°S), such as those in the Rwenzori, are primarily influenced by temperature (e.g., Taylor et al., 2006; Sagredo et al., 2014). This interpretation is supported by a comparison of the Holocene Rwenzori glacial fluctuations with temperature records from four tropical African lakes and the Congo River (e.g., Ivory et al., 2017) as well as precipitation records from Lakes Victoria and Tanganyika and the Nile River Delta (e.g., Tierney et al., 2008; Berke et al., 2012; Weldeab et al., 2014)(Figure 5.7.). The temperature records show warming between ~12 and 5 ka, with peak Holocene warmth at ~6-5 ka. This time period overlaps with the African Humid Period (AHP; ~11.6-5.0 ka), when precipitation in tropical Africa was very high (Garcin et al., 2007). That Rwenzori glaciers retreated during the early Holocene and were restricted during the middle

Holocene suggests that they were more sensitive to temperature than precipitation, or that temperatures were high enough to dominate glacial mass balance during this time. The inferred middle Holocene readvance of glaciers on Mt. Kenya is anomalous in tropical Africa, but it is possible that high precipitation events such as that at ~6.3 ka recorded in Nile River outflow (Weldeab et al., 2014) may have caused a localized glacial readvance on Mt. Kenya. Cooler temperatures between ~5 ka and ~200-150 years ago were coeval with late Holocene glacial advances in the Rwenzori as well as elsewhere in the tropics.

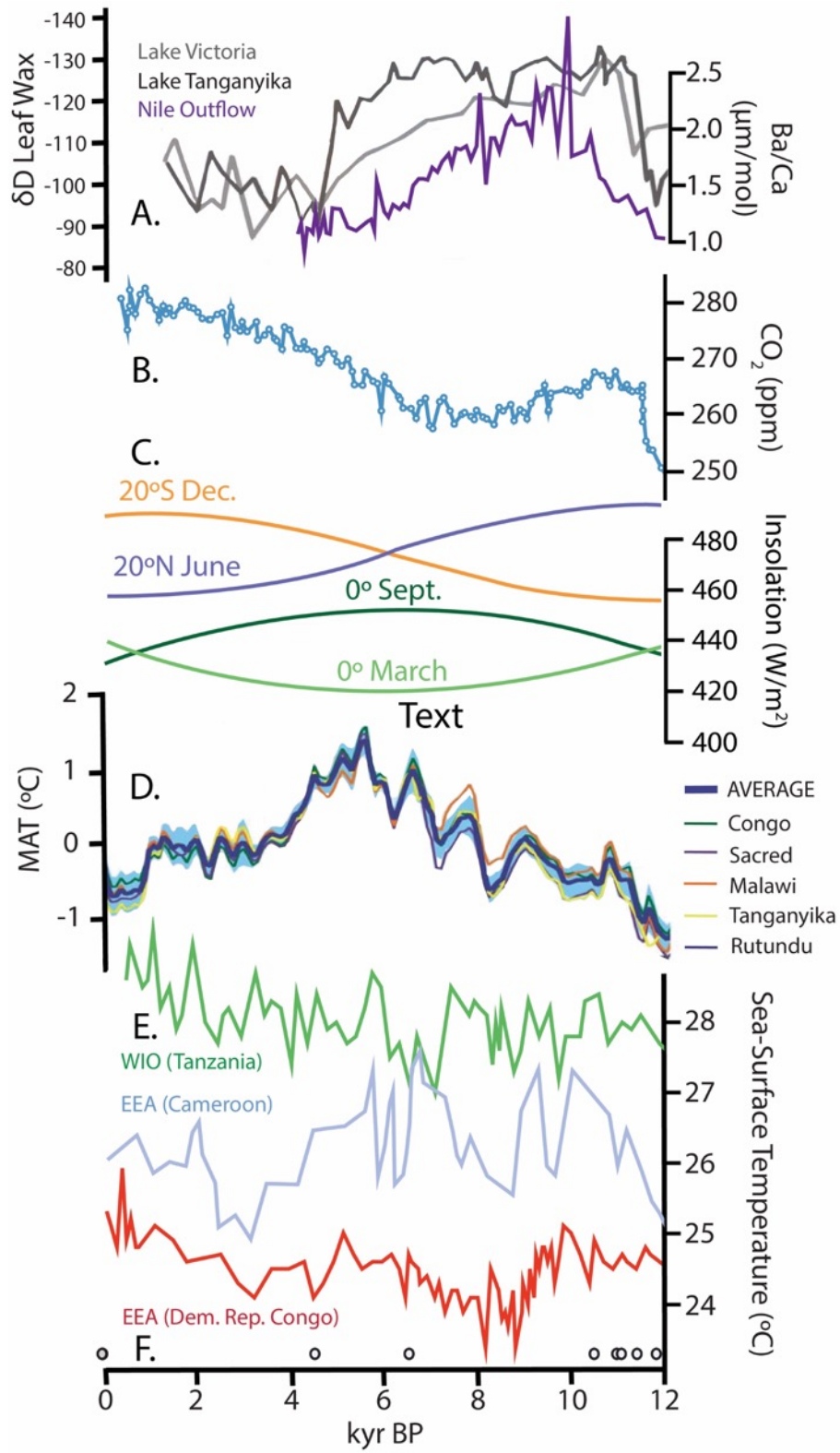
The mechanisms that drove terrestrial temperature changes in the tropics during the Holocene, however, are unclear. Greenhouse gas forcing and tropical sea-surface temperatures (SSTs) both are commonly invoked to explain changes in tropical temperature, but these forcings do not correspond with glacial extents or reconstructed air temperatures. Atmospheric CO₂ is coupled with tropical temperatures over glacial-interglacial timescales (Lea, 2004), yet CO₂ has a pattern of change that is dissimilar to tropical African terrestrial temperatures during the Holocene (Figure 5.7.). Because SSTs influence the temperature of air masses advected over land, tropical SSTs might be expected to show a pattern of warming similar to that of the terrestrial tropics. The Rwenzori are generally influenced by air masses sourced from the western Indian Ocean (Kaser and Osmaston, 2002; Singerayer et al., 2015), although eastern Atlantic Ocean-sourced air masses may reach the Rwenzori during the boreal winter (Singerayer et al., 2015). However, the patterns of Holocene SSTs in the western Indian Ocean and eastern Atlantic Ocean are not apparently correspond with tropical African temperatures (Figure 5.7). Similarly, Eastern Pacific and western Atlantic Ocean SSTs are commonly invoked as potential drivers of Holocene glacial fluctuations in tropical South America (Solomina

et al., 2015; Stansell et al., 2017), but tropical South American glacial extents are not well correlated with tropical SSTs (Stansell et al., 2017).

One potential mechanism to explain the pattern of tropical African terrestrial temperatures during the Holocene is changes in insolation. There are similarities between Northern Hemisphere insolation during the Holocene (i.e., high during the early Holocene and decreasing to a low during the late Holocene) and the pattern of tropical glacial fluctuations described above. However, Northern Hemisphere insolation decreased while tropical African glaciers were restricted and as tropical African terrestrial temperatures peaked at ~ 6-5 ka. Another possibility is that changes in equatorial rather than higher latitude insolation influenced tropical African terrestrial temperatures. The sun passes directly over the equator twice a year in September and March. High September or March insolation has been linked with changes in African monsoon strength and precipitation (McIntyre and Molino, 1996; Verschuren et al., 2009) and holds the potential to influence low latitude climate (Berger and Loutre, 2006), although the sensitivity of tropical terrestrial temperatures to low latitude insolation change is uncertain. Equatorial September insolation peaked at ~7-6 ka, just prior to the middle Holocene African terrestrial temperature peak at ~6-5 ka, and decreased after ~5 ka as glaciers began to re-nucleate or advance during the late Holocene (Figure 5.7.). Although changes in tropical glacial extents is coherent with shifts in equatorial insolation, the magnitude of expected temperature change induced by seasonal insolation change in the low latitudes is uncertain. Moreover the coupled influence of equatorial insolation change with other forcing mechanisms, such as atmospheric greenhouse gas changes, are not

clear. More work is needed to assess the possible influence of low latitude insolation on African tropical terrestrial temperatures and, thus, glacial extents.

Figure 5.7. East African climate during the Holocene. (A) Precipitation (δD leaf wax) records from Lakes Victoria (gray) and Tanganyika (black) and East Asian monsoon intensity (purple; Ba/Ca) from the Nile Delta (Tierney et al., 2008; Berke et al., 2012; Weldeab et al., 2014); (B) Atmospheric CO₂ (Monnin et al., 2004); (C) Tropical Holocene insolation at 20°N (June; blue), 20° S (Dec.; orange), and 0° (Sept. (dark green) and March (light green)); (D) Compiled Holocene terrestrial temperatures reconstructed from organic lacustrine sediments, plotted as anomaly versus the mean value over the last 2 ka (Ivory et al., 2017); (E) SST records from the equatorial Western Indian Ocean (WIO; green) and the Eastern Atlantic (EEA; light blue (Weldeab et al., 2005), red (Schefuß et al., 2005)); (F) ¹⁰Be ages from the Nyamugasani and Bujuku valleys that constrain Holocene glacial extents in the Rwenzori.



5.8. Conclusions

Twelve new ^{10}Be ages of glacial deposits in the Rwenzori Mountains suggest that glaciers retreated rapidly during the early Holocene and remained at or within their late Holocene maximum positions during much of the Holocene Epoch. These results are comparable to chronologies of past glacial extents elsewhere in tropical Africa, although glaciers on Mt. Kenya may have advanced down valley of their late Holocene maxima during the middle Holocene. Glacial chronologies in the tropical Andes suggest similar glacial fluctuations during Holocene time, with rapid glacial recession during the early Holocene followed by restricted ice margins until ~ 1 ka. The similarity between tropical African and South American glacial extents, as well as a comparison with tropical African terrestrial temperatures registered by organic sediments, indicates a common control on tropical glacial extents during the Holocene that was likely temperature. We suggest that low latitude insolation may have acted as a control on terrestrial temperatures and, thus, tropical glacial extents during the Holocene. However more work is needed to assess the sensitivity of tropical temperatures and glaciers to low latitude insolation.

5.9 Acknowledgements

We thank the Uganda Wildlife Authority and the Uganda National Council on Science and Technology for their support of and assistance with this project. We also thank Rwenzori Mountaineering Services and Rwenzori Trekking Services for their logistical support while in the field. Laura Hutchinson and David Cavagnaro helped process samples. This project was supported by the National Science Foundation (EAR-1702293), National Geographic, Comer Family Foundation, and Sigma Xi. Satellite imagery was granted by the DigitalGlobe Foundation. This is LLNL-JRNL-XXXX.

CHAPTER 6

CONCLUSIONS

6.1. Summary of Results

My dissertation research provides new constraints on glacial extents in the Rwenzori Mountains from the Last Glacial Maximum (LGM; ~26.5-19 ka) through historical time. Here I review briefly the Rwenzori glacial chronology, comparisons of this chronology with other glacial and climate records, and hypotheses regarding the possible forcing mechanisms that may have influenced glacial fluctuations in the Rwenzori Mountains and elsewhere in the tropics.

Glaciers in the Rwenzori reached their maximum LGM extent at ~21.5 ka. In the Mubuku valley ice was extensive from at least ~28 to ~21.5 ka, while in the more southern Moulyambouli valley ice remained extensive until ~18.8 ka. By ~18.8 ka recession was underway in both valleys. The post-LGM retreat of Rwenzori glaciers predates the onset of Termination 1 (~18.2 ka) as defined by abrupt shifts in global wind belts and the onset of rapid atmospheric CO₂ rise (Anderson et al., 2009; Denton et al., 2010), but is concurrent with higher-latitude ice sheet retreat (Chapter 3).

Rwenzori glaciers retreated during Heinrich Stadial 1 (HS1; ~18-15 ka) but the rate of retreat decreased during late-glacial time (~15-11 ka). Rwenzori glaciers were more extensive during the Antarctic Cold Reversal (ACR; ~14.7-13.0 ka) than the Younger Dryas (YD; ~12.9-11.7 ka), as evidenced by ¹⁰Be dated moraines and perched boulders in the Mubuku, Bujuku and Nyamugasani valleys (Chapter 4). However, the

Rwenzori glacial chronology suggests periods of relative cooling culminated at ~14 ka and ~ 12 ka, out of step with the timing of the ACR and YD as canonically defined.

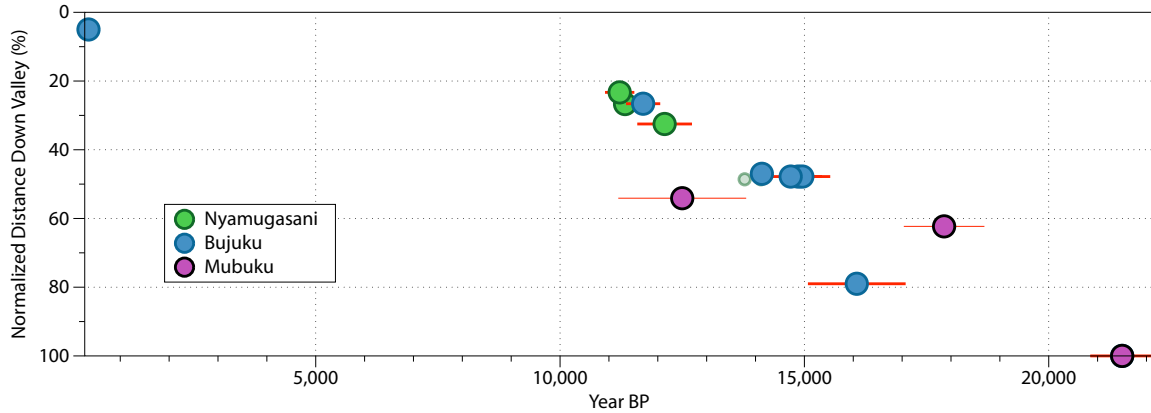


Figure 6.1. Rwenzori glacial chronology showing arithmetic mean moraine ages in three catchments. ^{10}Be ages are shown as a function of normalized distance down valley (in % of the maximum LGM position). Moraines are color coded by valley.

During the early Holocene (~11.6-8 ka), Rwenzori glaciers retreated rapidly in multiple valleys to near or within their late-Holocene (~4 ka-present) maximum positions (Chapter 5). ^{10}Be ages of perched boulders and ^{10}Be concentrations of glacially scoured bedrock indicate that ice in the Bujuku and Nyamugasani valleys remained at or inboard of their late-Holocene (~4 ka-present) extent through much of Holocene time.

The Rwenzori glacial chronology (Figure 6.1.) is similar to ^{10}Be dated glacial moraines in the tropical South American Andes. In both regions glaciers retreated from their LGM extents prior to the onset of Termination 1 at ~18 ka and retreated during HS1 (Shakun et al., 2015; Bromley et al., 2016). After HS1 the net rate of retreat of glaciers in the South American tropics slowed. Glaciers in the tropical Andes were more extensive

during the ACR than the YD (Jomelli et al., 2014; 2017; Mark et al., 2017) and retreated rapidly during the early Holocene. Tropical Andean glaciers remained near or within their late-Holocene maximum extents through much of Holocene time (Jomelli et al., 2014; Solomina et al., 2015). Records of clastic sediment input from tropical Andean glacial lakes suggest that glaciers in the South American tropics fluctuated during middle- and late-Holocene time even though they were located inboard of their late-Holocene extents (Rodbell et al., 2008). Sediment records from high-alpine lakes on Mt. Kenya likewise show evidence for middle and late-Holocene glacial fluctuations, with evidence for middle-Holocene readvance of ice in the Teleki and Hogley Valleys (Perrott et al., 1982; Johansson and Holmgren, 1985; Karlen et al., 1999). It is possible that glaciers in the Rwenzori likewise fluctuated throughout the Holocene, although they remained inboard of their late Holocene maximum extent throughout the Epoch.

The similarity of Rwenzori and South American glacial fluctuations suggests that glaciers across the tropics responded to a common driver over the last ~25 ka. Because precipitation varied distinctly between the Africa and South American tropics (Gasse, 2000; Novello et al., 2017), I suggest that a common pan-tropical temperature signal acted as a primary influence on tropical glacial extents. This is supported by studies of modern (e.g., Taylor et al., 2006; Sagredo and Lowell, 2012) and past tropical glaciers (Jomelli et al., 2014; Kelly et al., 2014), which suggest that low-latitude glaciers are more sensitive to temperature than to hydroclimate conditions (i.e., precipitation, humidity and cloudiness). The tropical troposphere is thermally homogenous (Pierrehumbert et al., 1995), which may help explain the coherence of past temperatures, and thus glacial fluctuations, across the tropics since the LGM.

If temperature has controlled tropical glacial fluctuations since the LGM, then what controlled tropical temperatures? Changes in insolation, atmospheric greenhouse gas (GHG) concentrations, changes in atmospheric and oceanic circulation, and tropical sea-surface temperatures (SSTs) all may have influenced tropical temperatures both during and after the LGM. In my research papers presented here (Chapters 3, 4, 5) I make detailed comparisons of the Rwenzori and tropical South American glacial chronologies with global climate proxy data to infer the possible influences of these various mechanisms. In Chapter 3, I suggest that the “early” retreat of tropical glaciers at the end of the LGM (i.e., prior to Termination 1 at ~18 ka) was influenced by rising summer insolation in the Northern Hemisphere (and increasing summer duration in the Southern Hemisphere) after ~24 ka. The insolation-driving warming at high latitudes would have decreased the interhemispheric thermal gradient and thus reduced the net export of heat from the tropics towards the high latitudes. As less heat was advected from the low latitudes, tropical temperatures rose.

The late-glacial millennial-scale fluctuations of tropical glaciers I describe in Chapter 4 indicate pan-tropical glacial recession during HS1 as well as more extensive glaciers during the ACR than during the YD. While atmospheric GHG concentrations and atmospheric and oceanic circulation are marked by abrupt changes throughout deglaciation, the timing of these abrupt shifts do not align with the timing of tropical glacial fluctuations (Chapter 4). For example, a period of tropical cooling culminated at ~14 ka, during the ACR. However, GHG forcing was unchanging at this time, and neither oceanic nor atmospheric circulation changed at ~ 14 ka. Although the ultimate driver of tropical temperatures during deglaciation remains uncertain, it is likely that temperatures

were influenced by multiple factors. The tropical glacial chronologies presented in Chapter 4 therefore reflect the additive effects of GHG forcing, atmospheric circulation shifts, and low-latitude SSTs.

Glaciers in the Rwenzori and elsewhere in the African tropics retreated rapidly during the Holocene and remained inboard of their late Holocene extents during much of Holocene time (Chapter 5). Glaciers in the South American Andes behaved similarly, remaining inboard of their late Holocene extents through much of the Epoch (Solomina et al., 2015). Lake-sediment-derived records of Holocene temperature in the African tropics indicate warm conditions during much of the early and middle Holocene, coherent with restricted glacial extents across the low latitudes. Clastic sediment records from glacially influenced lakes in both the African and South American tropics indicate that the margins of tropical glaciers fluctuated through much of the Holocene while remaining inboard of their late-Holocene maxima. Thus, while glaciers remained restricted through much of the Holocene they maintained dynamic margins during at least the middle and late Holocene (Karlen et al., 1999; Solomina et al., 2015). Tropical SSTs are considered a potential influence on low-latitude temperature fluctuations during the Holocene, but the relative strength of different ocean basins on pan-tropical temperatures remains uncertain (e.g., Stansell et al., 2017) and SSTs did not mirror atmospheric temperatures through Holocene time (Ivory et al., 2017; Weijers et al., 2007). Similarly, atmospheric CO₂ levels did not act as a primary driver of temperatures and glacial extents. One potential driver of Holocene temperature is the strength of equatorial insolation, which followed a pattern similar to that of reconstructed tropical African temperature. Additional work is required,

however, to assess the potential sensitivity of low latitude terrestrial temperatures to equatorial insolation.

The results presented within this dissertation make explicit the coherent pattern of glacial fluctuations across the tropics during and since the LGM. Although the precise mechanisms that drove past changes in tropical temperature, and thus tropical glacial extents, since the LGM remain unresolved, the Rwenzori chronology provides valuable benchmark data for climate models and for the assessment of potential forcing mechanisms of past tropical climate change.

6.2. Future Work

The Rwenzori glacial chronology presented here describes only a fraction of the many glacial features in the Rwenzori. Undated moraines occur in valleys across the massif; future mapping and dating of these features will establish more firmly the timing of past Rwenzori glacial fluctuations. One potential target is the northward trending Lamia valley, which contains deposits that range in (estimated) age from the pre-LGM to the Holocene. Whereas valleys such as the Bujuku and Nyamugasani feature complicated geometries and are fed by multiple catchments the Lamia valley features a relatively simple geometry. This helps simplify efforts to model former Lamia valley glacier dynamics and may help reduce uncertainties regarding the relative impacts of valley topography and climate on glacial fluctuations.

There are also numerous undated moraines within valleys for which age constraint already exists, including presumed LGM moraines in the Nyamugasani

valley and potential pre-LGM deposits in the Mubuku valley. Accessing these moraines for ^{10}Be dating is made difficult, however, by the dense montane forest vegetation at elevations where LGM deposits occur (~2000-3500 m asl). The glacial deposits described in this dissertation are largely those within an easy distance of existing hiking trail networks. Late-Holocene deposits in the Rwenzori occur above treeline (≥ 4000 m asl) on the slopes of the high peaks. These features are more readily accessible than deposits in area of dense forest cover and represent another avenue for investigation.

The Rwenzori also contain numerous high-alpine lakes, records from which may provide continuous data on local climate through preserved pollen and trace element concentrations. In glacially influenced lakes, records of clastic sediment input may reveal information regarding the fluctuations of past ice margins during periods for which no moraine record occurs. One such record from the Rwenzori (Russell et al., 2009) spans only the last few centuries, yet provides valuable information regarding the onset of recent glacial recession in the late 19th century. Collecting and analyzing lake sediment cores of ages which span into the late-glacial period could provide data to assess directly the magnitude and timing of past glacial recession and provide greater context for the ^{10}Be chronologies.

In addition to providing valuable paleoclimate data, these same lake cores could be used to establish a local ^{10}Be production rate. Current uncertainties in cosmogenic nuclide production are greatest within the low-latitudes where the impact of magnetic field change on incoming cosmic ray flux is greatest (Lifton,

2016). I used a high-altitude, low-latitude ^{10}Be production rate from the tropical Andes (Kelly et al., 2015) for all Rwenzori age calculations presented in this thesis. However error is introduced for all ^{10}Be age calculations for which the calibration site is non-local, as it must then be mathematically ‘scaled’ to account for differences in latitude and elevation on nuclide production between the calibration and target sample locations (Gosse and Phillips, 2001). Additional error comes from temporal ‘scaling’, which involves estimating the impact of changing magnetic field strength on the rate of nuclide production over time. This scenario is of particular concern when applying a ^{10}Be production rate to date features that are significantly older or younger than the original calibration time period (Gosse and Phillips, 2001; Dunai et al., 2010). Using bracketing basal radiocarbon ages from moraine-dammed lakes in the Rwenzori to establish a local production rate would reduce the uncertainty currently attached to surface-exposure ages from the massif.

APPENDIX A

SUPPLEMENTARY MATERIALS TO CHAPTER 3

A.1. Tropical ^{10}Be Site Descriptions

Sierra Nevada, Venezuela (8°N) - Wesnousky et al., 2012

Wesnousky et al. (2012) dated a series of moraines, terraces, and faulted features to assess the timing of regional glaciation and faulting. We recalculated the ^{10}Be ages from four moraines in three separate catchments. In two catchments, ice retreated from its LGM maximum extents by ~ 19.0 ka. The third catchment may indicate recession after ~ 17.7 ka.

La Victoria Moraine (one moraine)

Four samples (VEN19, -20, -21, -23) date the La Victoria moraine and yield a mean age of ~ 19.0 ka. In GoogleEarth, we observed two or three additional moraines distal to the La Victoria ridge. There are no ^{10}Be ages from these moraines.

Los Zerpas Moraines (two moraines)

Six samples (VEN25, -26, -27, -28; LZ09-01, -02) date the right-lateral and left-lateral Los Zerpas moraines and yield arithmetic-mean moraine ages of ~ 25.2 and 17.7 ka, respectively. For our analysis, we used one ^{10}Be age of the right-lateral moraine (VEN25, 20.5 ± 1.6 ka) and three ^{10}Be ages of the left-lateral moraine (VEN26-28, mean age ~ 19.2 ka). We excluded sample LZ09-02 (15.1 ± 1.1 ka) from the right-lateral moraine and sample LZ09-01 (16.8 ± 1.6 ka) from the left-lateral moraine because they

are apparently young. These ^{10}Be ages were not identified as outliers by the original authors. We also excluded sample VEN24 (47.0 ± 4.5 ka) from the left-lateral moraine. This ^{10}Be age was considered an outlier by Wesnousky et al. (2012). In GoogleEarth, we did not observe additional moraines distal to the Los Zerpas moraines, although the heavily faulted nature of these moraines makes glacial geologic interpretations difficult. We consider the 17.7 ka age more representative of the timing of ice recession.

Faulted Moraine (one moraine)

One sample (VEN18) dates the faulted moraine and yields an age of ~ 21.7 ka. This ^{10}Be age is not discussed in the original paper. For our analysis, we used the one age as the mean moraine age.

Sierra Nevada, Venezuela (8°N)

Carcaillet et al. (2013)

Carcaillet et al. (2013) dated two in a series of moraines that dam the modern Laguna de Mucubaji. Ice retreated from its LGM maximum extent by ~ 21 ka.

Laguna de Mucubaji (two moraines)

One sample (MU09-02) from the outermost dated moraine yields a ^{10}Be age of 22.6 ± 1.8 ka. One sample (MU09-01) from the innermost dated moraine yields a ^{10}Be age of 20.7 ± 0.7 ka. For our analysis, we used these ages to calculate arithmetic-mean moraine ages. We consider the age of 20.7 ka as representative of recession from the LGM maximum position.

Cajamarca, Peru (7°N)

Shakun et al., 2015

Shakun et al. (2015) dated moraines in three former glacier catchments. In all catchments, ice retreated from its LGM maximum extents by ~22 ka.

North Camp Moraines (two moraines)

The North Camp Moraines consist of paired right- and left-lateral moraines that mark the apparent maximum extent of ice in the catchment during the LGM. Two ^{10}Be ages (MC-NC-5, -6) are from the right-lateral moraine and four ^{10}Be ages (MC-NC-7, -8, -9, -10) are from the left-lateral moraine. Shakun et al. (2015) excluded three ages (MC-NC-2, ~51.1 ka; MC-NC-3, ~68.4 ka; MC-NC-4, ~169.2 ka) because of presumed inherited ^{10}Be . The remaining six samples yield arithmetic-mean moraine ages of ~23.6 ka (right-lateral) and ~23.7 ka (left-lateral). For our analyses, we used these six ages.

Galeno Moraines (three moraines)

The Galeno Moraines are a sequence of ~5 nested moraines and are dated with nine ^{10}Be ages. One sample (MC-G-3; 18.9 ± 0.4 ka) is from the outermost dated terminal moraine. Two samples (MC-G-4, -2) are from a more proximal terminal moraine and yield a mean moraine age of ~17.3 ka. Five samples (MC-G-1, -6, -7, -8, -9) are from lateral moraines and yield a mean moraine age of ~20.4 ka. Shakun et al. (2015) exclude one age (MC-G-5, 46.0 ± 0.9 ka) because of presumed inherited ^{10}Be . For our analysis, we used the ^{10}Be age of MC-G-3 (18.9 ± 0.4 ka) as an arithmetic-mean moraine age. We averaged samples MC-G-4 and -2 for an arithmetic-mean moraine age of ~17.3 ka. In

GoogleEarth, we had difficulty observing the context of samples MC-G-1, -6, -7, -8, -9 and were not able to determine whether they are on a single or multiple moraines. Therefore, we assumed that they were on a single moraine and averaged their ^{10}Be ages to determine an arithmetic-mean moraine age (~ 20.4 ka).

San Cirillo Moraines (not used)

The San Cirillo Moraines are within a catchment dotted by kettle lakes and hummocks. Eleven samples (SC-2 to -13) are from boulders on moraines and boulders perched on bedrock. These samples do not date a single landform. For our analysis, we excluded this dataset because we could not assign a moraine age. However, in general these ^{10}Be ages indicate 1) that ice in the catchment achieved its LGM maximum extent prior to ~ 29 ka and 2) that ice retreated from its LGM maximum extent by ~ 22 ka.

Cordillera Blanca, Peru (9°S)

Farber et al., 2005

Farber et al. (2005) dated moraines in two glacier catchments. In both catchments, ice was at or near its LGM maximum extent from at least ~ 29 to 21 ka, and recession from the LGM maximum extent was underway by ~ 21 ka.

Rurec Group 2, Quebrada Cojup (one moraine)

Five samples (HU-1, -2, -4, Peru-21, K-9) from a left-lateral moraine yield an arithmetic-mean moraine age of ~ 21.3 ka. For our analysis, we used samples (HU-1, -2, -4, and Peru-21) and considered sample K-9 (18.1 ± 1.0 ka) an outlier due to its

apparently young age and its distance (~1 km) from the other four samples. The four samples (HU-1, -2, -4, and Peru-21) yield an arithmetic-mean moraine age of ~23.3 ka. However, we note that when plotted in GoogleEarth it is unclear whether the samples are located on a single moraine. For this reason, we do not classify this moraine age as representative of the onset of recession from the LGM maximum position.

Rurec Group 2, Quebrada Llaca (four moraines)

One sample (K-4) from the innermost dated right-lateral moraine yields an age of 22.7 ± 1.1 ka. We used this one ^{10}Be age as an arithmetic-mean moraine age. One sample (K-3) from the next (more distal) right-lateral moraine yields an age of 24.5 ± 1.1 ka. We used this one ^{10}Be age as an arithmetic-mean moraine age. Two samples (K-5a, 29.4 ± 1.4 ka and K-5b, 29.0 ± 0.9 ka) from the outermost dated right-lateral moraine yield an arithmetic-mean moraine age of 29.2 ± 0.3 ka.

Six samples (K-6a, -6b, -8a, -8b, -2, -7) are from the innermost dated left-lateral moraine and four of these samples (K-6a, -6b, -8a, -8b) were dated twice. For our analysis, we used all ten ^{10}Be ages to determine an arithmetic-mean moraine age of ~19.6 ka. We consider this age as representative of the onset of recession from the LGM maximum extent.

Cordillera Blanca, Peru (10°S)

Smith & Rodbell, 2010

Smith & Rodbell (2010) dated a large left-lateral moraine in the Quenua Ragra Valley. Ice retreated from its LGM maximum extent by at least ~21 ka.

Quenua Ragra Valley (one moraine)

Four samples (JEU-33, -34, -35, -36) from a left-lateral moraine yield a mean moraine age of ~21.3 ka. For our analysis, we used the four ^{10}Be ages but note that, when plotted in GoogleEarth, the moraine appears to have multiple crests and it is unclear whether the samples are from a single crest.

Lake Junin, Peru (10°S)

Smith et al., 2005a

Smith et al. (2005a) dated moraines in four glacier catchments near the modern Lake Junin. In all valleys, ice retreated from its LGM maximum extent between ~20 and ~17 ka.

Collpa Valley (one moraine)

Five samples (COL-01, -02, -03, -04, -07) from a left-lateral moraine yield an arithmetic-mean moraine age of ~26.8 ka.

Calcalcocha Valley (six moraines)

Seven samples (CAL-08 to -14) from the middle Calcalcocha Valley are from a series of low-relief terminal moraines and yield ^{10}Be ages between ~23.8 and 19.3 ka. Four of these samples (CAL-08, -11, -12, -13) from a terminal moraine yield an arithmetic-mean age of ~21.4 ka. When plotted in GoogleEarth, the low-relief moraines are not clear and it is difficult to see where samples lie on the moraines. A single sample (CAL-14, 22.2 ± 0.8 ka) is from a more distal terminal moraine. We used this one ^{10}Be

age as the mean moraine age. Two samples (CAL-09, -10) from a right-lateral moraine yield an arithmetic-mean moraine age of ~21.3 ka. We suggest this age may be most representative of the timing of the onset of recession from the LGM maximum extent, as it is in stratigraphic order with the moraine described below (~19.5 ka). However, we do not use this age as such in our analysis.

Farther up the Calcolcocha Valley, seven samples date three nested moraines. One sample (CAL-07) is from the outermost moraine and yields a ^{10}Be age of 17.5 ± 1.6 ka. Three samples (CAL-04, -05, -06) from a moraine proximal to the ~17.5 ka moraine yield an arithmetic-mean age of ~17.4 ka. Three samples (CAL-01, -02, -03) from the innermost moraine yield an arithmetic-mean age of ~19.5 ka. Conservatively, we use this age (~19.5 ka) as the timing of recession from the LGM maximum position in the valley.

There are additional dated moraines distal to the moraine in the middle Calcolcocha Valley. We did not include the ^{10}Be ages of these moraines in our analysis because they pre-date the LGM (>40 ka).

Antacocha Valley (eight moraines)

In the middle Antacocha Valley, eight samples (ANT-08 to -14) date a series of low-relief terminal moraines. We exclude these ages from our analysis because they predate the LGM.

In the upper Antacocha Valley, seven samples (ANT-01 to -07) date six moraines that mark the former terminal positions of a glacier in the valley. For our analysis, we used the seven ^{10}Be ages and assigned them to six moraines. Samples ANT-05 and -06 date the outermost moraine and yield an arithmetic-mean moraine age of ~18.3 ka.

Sample ANT-04 (21.3 ± 0.9 ka) may also date this outermost ridge, but due to uncertainty in the geomorphic context of the sample we treat it as an individual arithmetic-mean moraine age. Sample ANT-03 (20.7 ± 0.6 ka) dates the next more proximal moraine. Roughly 100 m from ANT-03 on the same apparent moraine ridge, ANT-07 yields an age of 19.7 ± 0.7 ka. However, again due to uncertainty in geomorphic context, we treat these samples as representative of individual moraine ridges. Sample ANT-02, which appears to be more proximal relative to samples ANT-03 and ANT-07, yields an age of 20.6 ± 0.6 ka. One sample (ANT-01) from the innermost dated moraine yields an age of 19.3 ± 0.7 ka. Conservatively, we treat the age of ~ 19.3 ka as representative of the timing of the onset of ice recession.

Alcacochoa Valley (three moraines)

In the lower Alcacochoa Valley, eleven samples (ALC-23 to -25, ALC-01 to -05, ALC-26 to -29) range in age from ~ 34.1 to 16.8 ka. These samples are from former terminal positions in the central portion of the valley. We exclude these ^{10}Be ages from our analysis because of the spread in ages and because these ages are out of stratigraphic order with other moraine ages in the valley.

In the middle Alcacochoa Valley, two samples (AL006, 007) from a terminal moraine yield a mean moraine age of ~ 19.6 ka. Proximal to this moraine, one sample (AL010) from a separate moraine yields an age of 20.8 ± 0.5 ka. For our purposes, we consider the age of ~ 19.6 ka as most representative of the timing of recession.

Four samples (ALC-03 to -06) are from a moraine ridge ~ 250 m away from the ~ 19.6 ka moraine and yield a mean moraine age of ~ 21.3 ka. This moraine may be a

portion of the ~19.6 ka moraine, but due to uncertainty in the relationship between these moraine segments we treat this moraine as a separate landform. We excluded sample ACL-07 (35.2 ± 1.0 ka) as an outlier.

In the upper Alcacocha Valley, seven samples (AL001-5, PE01-ALC-01, -2) yield ages between ~17.0 and 33.5 ka. We excluded these samples from our analysis because these ages are 1) out of stratigraphic order with other samples from the valley, 2) post-LGM, or 3) not associated with moraines when viewed in GoogleEarth.

Cordillera Oriental, Peru (14°S)

Bromley et al., 2016

Bromley et al. (2016) dated three terminal moraines at Quebrada Tiratana and one right-lateral moraine near Laguna Aricoma. At both sites ice retreated from its LGM maximum by at least ~18.8 ka.

Quebrada Tirataña (three moraines)

Two samples (NT-11-05, -08) from the outermost dated moraine yield a mean age of ~27.0 ka. One sample (NT-11-13) from a more proximal moraine yields an age of 25.3 ± 0.3 ka. We used this one ^{10}Be age as the mean moraine age. One sample (NT-11-18) from the innermost dated moraine yields an age of 21.6 ± 0.3 ka. We used this one ^{10}Be age as the mean moraine age.

Laguna Aricoma (one moraine)

Two samples (ARC-09-25, -26) from a right-lateral moraine yield a mean age of ~18.8 ka. This moraine is the outermost landform. There are numerous undated more proximal lateral moraines.

Milluni Valley, Bolivia (16°S)

Smith et al., 2005b

Smith et al. (2005b) dated two left-lateral moraines in the Milluni Valley that are ~200 m apart. Below we describe these moraines as the outermost and innermost moraines. In general, the ice was at or near its LGM maximum extent between ~30 and 18 ka.

Milluni valley (one moraine)

Seven samples (MIL-00-08 to -14) from the outermost moraine yield an arithmetic-mean age of 29.3 ± 2.5 ka. Seven samples (MIL-00-01 to -07) from innermost moraine yield an arithmetic-mean age of 30.5 ± 8.9 ka. Three ^{10}Be ages (MIL-00-01, 37.6 ± 1.0 ka; MIL-00-02, 35.6 ± 1.0 ka; MIL-00-04, 41.1 ± 1.5 ka) of the innermost moraine are older than the oldest age (MIL-00-13, 33.5 ± 0.9 ka) of the outermost moraine. Two ages from the innermost moraine (MIL-00-03D, 30.7 ± 0.8 ka and MIL-00-07, 31.7 ± 0.9 ka) are similar to those from the outermost moraine. For our analysis, we use the two ^{10}Be ages of the innermost moraine (MIL-00-05, 17.5 ± 0.5 ka; MIL-00-06, 19.6 ± 0.6 ka) and determine an arithmetic-mean moraine age of ~18.6 ka, which we take as the maximum-limiting timing of recession from the LGM maximum extent.

Cordillera Real and Cochabamba, Bolivia (15-17°S)

Zech et al., 2007

Zech et al. (2007) dated moraines in Valle San Francisco and Valle Huara Loma, two separate catchments. In both catchments, ice retreated from its LGM maximum extent by ~22 ka.

Valle San Francisco (three moraines)

Three samples (SF-41, -42, -43) from the outermost dated right-lateral moraine yield a mean age of ~34.6 ka. Two samples (SF-32, -33) from a more proximal right-lateral moraine yield a mean age of ~28.1 ka. Two samples (SF-12, -13) from a left-lateral moraine yield a mean age of ~27.4 ka.

Valle Huara Loma (one moraine)

Two samples (HH51, -52) from a right-lateral moraine ridge segment yield an arithmetic-mean age of ~22.7 ka. Additional moraines at this site are dated by May et al., 2011 (described below).

Cordillera de Cochabamba, Bolivia (17°S)

May et al., 2011

May et al. (2011) dated four moraines in Valle Huara Loma. Ice retreated from its LGM maximum extent between ~22 and ~20 ka.

Valle Huara Loma

One sample (HL11) from a left-lateral moraine yields an age of 28.8 ± 1.9 ka. Down valley from HL11, on an apparent terminal moraine, sample HL12 yields an age of 20.3 ± 1.2 ka. We consider this age the most representative of the timing of ice recession from the LGM maximum at this site. Farther down valley, one sample (HL43) from a right-lateral moraine yields an age of 23.4 ± 1.1 ka. These moraines are proximal to the ridge dated by Zech et al. (2007)(53) described above.

Two additional samples from a more distal right-lateral moraine (HL51, -52) yield a mean age of ~ 29.7 ka.

A.2. Climatic Controls on Tropical Glaciation

The similarity in timing of the onset of deglaciation in tropical Africa and South America at ~ 20 -19 ka suggests that glaciers in both regions responded to a common forcing, most likely temperature. We do not discount that precipitation changes may have influenced individual glacial fluctuations both during and following the LGM, and emphasize that precipitation plays a role in tropical glacial mass balance (Kaser and Osmaston, 2002). However, we suggest that the tropical glacial systems discussed within the text are temperature rather than precipitation-limited.

Studies of modern (Sagredo and Lowell, 2012; Taylor et al., 2006) and past (Jomelli et al., 2014) tropical glaciers show that temperature is a dominant influence on glacial mass balance in the humid inner tropics (10°N - 10°S). Prior work in South America suggests that glacial advances during the early LGM in tropical South America were influenced by increased precipitation associated with high mean-annual equatorial

insolation, which peaked at ~30 ka (Smith et al., 2005b, Berger and Loutre, 1991; Fig. 2). We note that precipitation patterns varied across the South American tropics during the LGM and at the onset of deglaciation (Novello et al., 2017), as did the onset of wetter conditions following the LGM. At Santiago Cave, Peru, and at Salar Uyuni, Bolivia, relatively dry conditions during the LGM ameliorated only after ~18 ka (Mosblech et al., 2012; Baker et al., 2001), after the onset of glacial recession. It is worth noting, however, that the ‘dry’ conditions of the LGM at these sites are either wetter than or similar to conditions recorded during the Holocene. In Venezuela, Cariaco Basin sedimentation rates indicate the LGM period in the northern South American tropics was relatively wet, and likewise gave way to drier conditions only after the onset of deglaciation (Deplazes et al., 2013).

GDGT records from tropical African lakes also indicate conditions in the region during the LGM (Loomis et al., 2017; Powers et al., 2005; Tierney et al., 2008). Previous work in the Rwenzori showed that LGM glaciation took place contemporaneously with dry and cold conditions (Kelly et al., 2014, and references therein). We also suggest that precipitation records from the African tropics are dissimilar to those from tropical South America (Gasse, 2000).

Based upon the information above, we infer that past fluctuations of Rwenzori glaciers were influenced primarily by past tropospheric temperature changes.

A.3. Evidence of Ocean Circulation Change at the Onset of the Last Deglaciation

During the last termination, changes in Atlantic Meridional Overturning Circulation (AMOC) impacted inter-hemispheric heat transport and the position of global wind belts, which could have affected tropical SSTs. However there is no evidence for such abrupt oceanic reorganization at 20 ka; records of AMOC strength and Intertropical Convergence Zone (ITCZ) position suggest stable conditions between ~24-19 ka (Deplazes et al., 2013; McManus et al., 2004; Böhm et al., 2014) and meltwater release from the Antarctic Ice Sheet (AIS) at ~20-19 ka is not considered significant enough to have affected broader oceanic circulation (Weber et al., 2014).

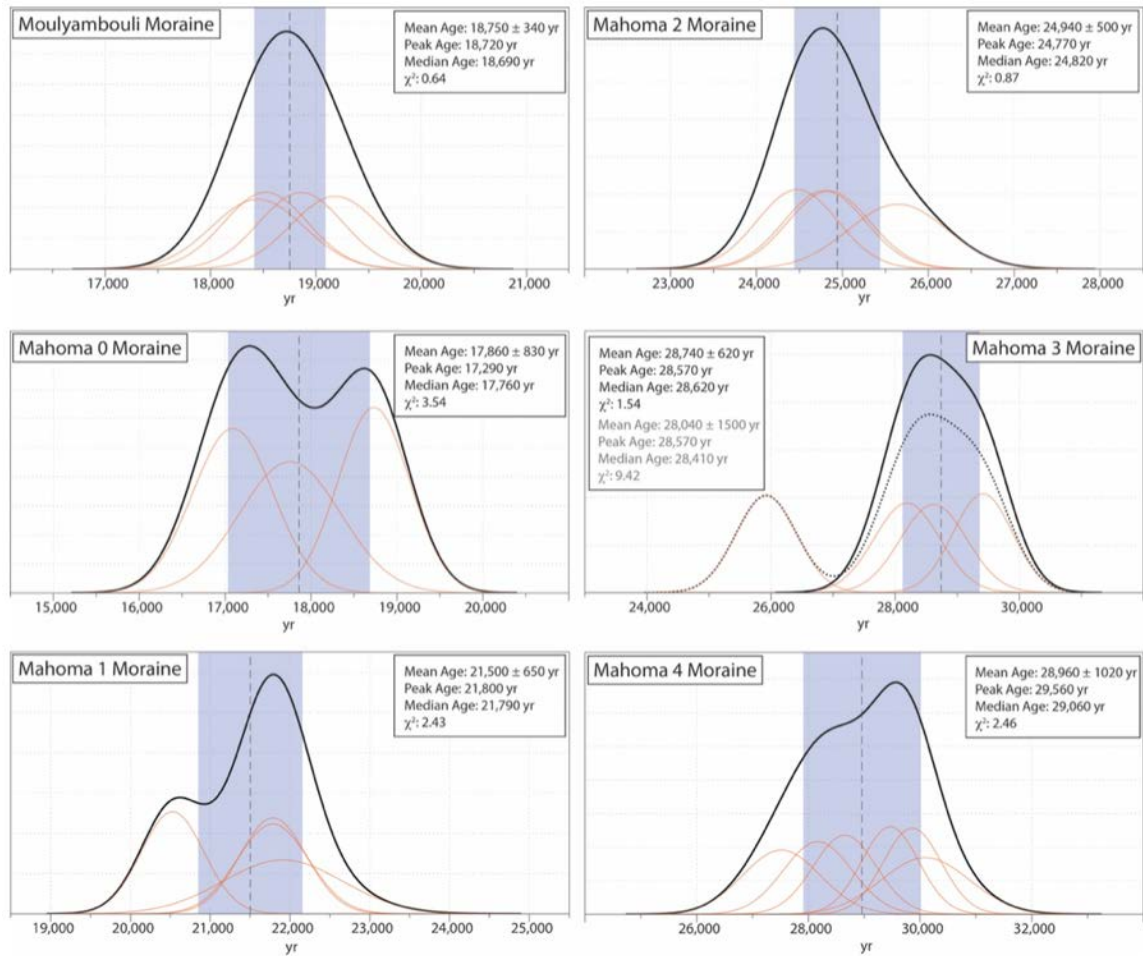


Figure A1. Camel plots showing probability-distribution curves for individual moraine ages with sample age statistics. Time (yr) is on the x-axis, and relative probability (unitless) is on the y-axis for each plot. Single sample ^{10}Be ages are represented by red lines, moraine ages by black lines. Dashed lines indicate the arithmetic-mean moraine age, bounded by 1-sigma standard deviation in blue. The dashed curve within the Mahoma 3 moraine plot indicates the age of the moraine prior to removal of outliers (statistics shown in gray).

A.4. Sample Information for Chapter 3

Table A1. ^{10}Be surface-exposure ages age calculation input for the online calculator as described by Balco et al. (2008) and subsequently updated and measured beryllium ratios. All $^{10}\text{Be}/^9\text{Be}$ ratios were measured at Lawrence Livermore National Laboratory Center for Accelerator Mass Spectrometry (CAMS).

<i>Map ID</i>	<i>Sample</i>	<i>Lat.</i>	<i>Long.</i>	<i>Elev.</i>	<i>Atm.</i>	<i>Thickness</i>	<i>Density</i>	<i>Shielding</i>	<i>Erosion</i>	<i>^{10}Be conc.</i>	<i>^{10}Be uncertainty</i>
		(DD)	(DD)	(m)		(cm)	(g/cm ³)		(cm/yr)	(at/g)	(at/g)
<u>Moulyambouli</u>											
1	RZ-12-4 6	0.2616 7	29.9441	2883	std	1	2.65	0.966	0	283882	6007
2	RZ-12-4 7	0.2615 2	29.9443 8	2872	std	4.21	2.65	0.962	0	269035	5787
3	RZ-12-5 0	0.2608 9	29.9452 4	2848	std	1.64	2.65	0.972	0	283626	6202
4	RZ-12-5 4	0.2581 2	29.9472 4	2777	std	3	2.65	0.983	0	262419	6232
<u>Mahoma 0</u>											
5	RZ-16-4 6a	0.3473 4	29.9611 8	2922	std	2.69	2.65	0.975	0	286711	6356
6	RZ-16-4 7a	0.3473 4	29.9611 8	2922	std	2.16	2.65	0.976	0	263082	7208
7	RZ-16-4 8a	0.3473 5	29.9611 9	2923	std	1.72	2.65	0.973	0	273628	9035
-	RZ-16-4 6	0.3473 4	29.9611 8	2922	std	2.69	2.65	0.975	0	290173	6799
-	RZ-16-4 7	0.3473 4	29.9611 8	2922	std	2.16	2.65	0.976	0	318066	5837
-	RZ-16-4 8	0.3473 5	29.9611 9	2923	std	1.72	2.65	0.973	0	263376	5496
<u>Mahoma 1</u>											
8	RZ-12-0 1	0.3582 8	29.9791	2635	std	2.14	2.65	0.994	0	291543	5576
10	RZ-12-0 7	0.3503 3	29.9681 2	2955	std	1	2.65	0.978	0	346969	11758

11	RZ-12-0 8	0.3498 5	29.9680 4	2953	std	2.13	2.65	0.978	0	341471	6979
-	RZ-12-0 8a	0.3498 5	29.9680 4	2953	std	2.13	2.65	0.978	0	341595	6445
9	RZ-12-0 9	0.3521	29.9693 4	2922	std	1	2.65	1	0	326609	6243
<u>Mahoma 2</u>											
12	RZ-12-0 2	0.3459 7	29.9679 8	2988	std	2.26	2.65	1	0	398870	7611
-	RZ-12-0 2a	0.3459 7	29.9679 8	2988	std	2.26	2.65	1	0	396922	6504
13	RZ-12-0 3	0.3459 7	29.9679 8	2988	std	1.79	2.65	1	0	405605	7743
14	RZ-12-0 4	0.3444 9	29.9689 6	2986	std	2.32	2.65	1	0	417238	9293
15	RZ-12-0 5	0.3441	29.9686 4	2989	std	2.89	2.65	1	0	403011	7700
<u>Mahoma 3</u>											
19	RZ-13-6 3	0.3432 7	29.9692 7	2947	std	2.2	2.65	0.982	0	406004	7589
18	RZ-13-6 4	0.3439 8	29.9697 2	2936	std	2.16	2.65	0.991	0	449547	8383
17	RZ-13-6 6	0.3447 1	29.9702 6	2940	std	3.25	2.65	0.995	0	441571	8248
16	RZ-13-6 7	0.3452 8	29.9707 1	2927	std	2.47	2.65	0.995	0	460279	7463
<u>Mahoma 4</u>											
20	RZ-16-4 9	0.3409	29.9686 3	2943	std	1.08	2.65	0.986	0	453420	8878
21	RZ-16-5 0	0.3409 8	29.9686 3	2941	std	2.34	2.65	0.986	0	470693	12261
22	RZ-16-5 2	0.3410 2	29.9687	2939	std	2.87	2.65	0.987	0	428831	10782
23	RZ-16-5 4	0.3405 9	29.9681 9	2933	std	4.01	2.65	0.99	0	434683	9436
24	RZ-16-5 5	0.3405 9	29.9681 9	2933	std	3.52	2.65	0.99	0	456412	7864
25	RZ-16-5 6	0.3412 1	29.9687 3	2932	std	4.64	2.65	0.982	0	454357	7829

Table A1. (continued)

<i>Sample</i>	<i>9-BeCarrier</i>	<i>Carrier added</i>	<i>Quartz wt.</i>	<i>Be Cathode</i>	<i>10-Be/9-Be</i>	<i>10-Be/9-Be</i>	<i>Process Blank</i>	<i>Process Blank</i>	<i>Process Blank</i>
	<i>Conc. (ppm)</i>	<i>(g)</i>	<i>(g)</i>	<i>(LLNL ID)</i>	<i>ratio</i>	<i>ratio (±)</i>	<i>10-Be/9-Be</i>	<i>10-Be/9-Be</i>	<i>Cathode</i>
<i>Moulyambouli</i>							<i>ratio</i>	<i>ratio</i>	<i>(LLNL ID)</i>
RZ-12-4 6	1335	0.1628	3.032	BE37994	5.93E-14	1.25E-15	4.38E-16	1.49E-16	BE37998
RZ-12-4 7	1335	0.1625	3.0322	BE37995	5.63E-14	1.21E-15	4.38E-16	1.49E-16	BE37998
RZ-12-5 0	1335	0.1631	3.0417	BE37996	5.93E-14	1.30E-15	4.38E-16	1.49E-16	BE37998
RZ-12-5 4	1335	0.1625	3.0733	BE37997	5.56E-14	1.32E-15	4.38E-16	1.49E-16	BE37998
<i>Mahoma 0</i>									
RZ-16-4 6a	1349	0.1569	2.0504	BE43144	4.16E-14	9.21E-16	5.69E-16	1.27E-16	BE43147
RZ-16-4 7a	1349	0.1566	2.1	BE43145	3.91E-14	1.07E-15	5.69E-16	1.27E-16	BE43147
RZ-16-4 8a	1349	0.1574	2.0285	BE43146	3.91E-14	1.29E-15	5.69E-16	1.27E-16	BE43147
RZ-16-4 6	1346	0.1526	5.0422	BE42276	1.07E-13	2.50E-15	1.05E-15	1.91E-16	BE42279
RZ-16-4 7	1346	0.1825	5.0181	BE42277	9.72E-14	1.78E-15	1.05E-15	1.91E-16	BE42279
RZ-16-4 8	1346	0.1484	5.1793	BE42278	1.02E-13	2.13E-15	1.05E-15	1.91E-16	BE42279
<i>Mahoma 1</i>									
RZ-12-0 1	1320	0.1584	6.0131	BE34425	1.25E-13	2.40E-15	2.54E-16	1.10E-16	BE34433
RZ-12-0 7	1320	0.1617	5.9925	BE34430	1.46E-13	4.94E-15	2.54E-16	1.10E-16	BE34433
RZ-12-0 8	1320	0.1626	5.9983	BE34431	1.43E-13	2.92E-15	2.54E-16	1.10E-16	BE34433
RZ-12-0 8a	1341	0.1639	7.0494	BE41129	1.64E-13	3.09E-15	8.48E-16	2.32E-16	BE41134
RZ-12-0 9	1320	0.1597	6.0115	BE34432	1.39E-13	2.66E-15	2.54E-16	1.10E-16	BE34433
<i>Mahoma 2</i>									

RZ-12-0 2	1320	0.16	6.0026	BE34426	1.70E-13	3.24E-15	2.54E-16	1.10E-16	BE34433
RZ-12-0 2a	1341	0.164	7.0782	BE41128	1.91E-13	3.13E-15	8.48E-16	2.32E-16	BE41134
RZ-12-0 3	1320	0.1593	6.0282	BE34427	1.74E-13	3.32E-15	2.54E-16	1.10E-16	BE34433
RZ-12-0 4	1320	0.1615	6.0002	BE34428	1.76E-13	3.92E-15	2.54E-16	1.10E-16	BE34433
RZ-12-0 5	1320	0.1604	5.9939	BE34429	1.71E-13	3.26E-15	2.54E-16	1.10E-16	BE34433
<i>Mahoma 3</i>									
RZ-13-63	1340	0.1605	4.0866	BE40304	1.15E-13	2.16E-15	7.22E-16	1.41E-16	BE40308
RZ-13-6 4	1340	0.164	4.1512	BE40305	1.27E-13	2.37E-15	7.22E-16	1.41E-16	BE40308
RZ-13-6 6	1340	0.1626	4.0284	BE40306	1.22E-13	2.28E-15	7.22E-16	1.41E-16	BE40308
RZ-13-6 7	1340	0.1627	4.0547	BE40307	1.28E-13	2.08E-15	7.22E-16	1.41E-16	BE40308
<i>Mahoma 4</i>									
RZ-16-4 9	1342	0.1523	3.0692	BE41586	1.02E-13	2.00E-15	2.04E-15	3.36E-16	BE41593
RZ-16-5 0	1342	0.1531	3.0391	BE41587	1.04E-13	2.71E-15	2.04E-15	3.36E-16	BE41593
RZ-16-5 2	1342	0.1535	3.0893	BE41588	9.62E-14	2.42E-15	2.04E-15	3.36E-16	BE41593
RZ-16-5 4	1342	0.1525	3.0421	BE41589	9.67E-14	2.10E-15	2.04E-15	3.36E-16	BE41593
RZ-16-5 5	1342	0.1535	3.0099	BE41590	9.98E-14	1.72E-15	2.04E-15	3.36E-16	BE41593
RZ-16-5 6	1342	0.1512	3.0099	BE41591	1.01E-13	1.74E-15	2.04E-15	3.36E-16	BE41593

Table A2. ^{10}Be surface-exposure ages as described in Chapter 3. All ages are reported as calculated using both time-independent (“St”) scaling and time-dependent (“Lm”, “LSDn”) scaling. Arithmetic mean ages for single moraines are provided where possible, with both the standard deviation and standard error of each arithmetic mean age. Arithmetic means are calculated using ages as calculated using “St” scaling.

Map ID	Sample	Sample Age			Sample Age			Sample Age			Arithmetic	Std. Dev.
		St-age	St-err(int)	St-err(ext)	Lm-age	Lm-err(int)	Lm-err(ext)	LSD-age	LSD-err(int)	LSD-err(ext)	Mean Age (St)	± (St)
1	RZ-12-46	18858	401	1139	16788	357	1031	18049	384	1114	--	--
2	RZ-12-47	18523	400	1121	16499	356	1015	17771	384	1099	--	--
3	RZ-12-50	19183	422	1164	17044	374	1051	18361	403	1138	--	--
4	RZ-12-54	18448	440	1132	16454	392	1026	17772	424	1114	18753	338
5	RZ-16-46a	18731	417	1138	16673	371	1030	17916	399	1112	--	--
6	RZ-16-47a	17090	470	1074	15385	423	982	16494	454	1058	--	--
7	RZ-16-48a	17755	589	1164	15908	527	1057	17097	567	1141	17859	825
	RZ-16-46	18961	446	1161	16874	397	1050	18118	426	1133	--	--
	RZ-16-47	20681	381	1231	18129	334	1097	19520	360	1188	--	--
	RZ-16-48	17090	358	1030	15384	322	943	16493	346	1016	--	--
8	RZ-12-01	21787	419	1302	18957	364	1152	20584	396	1258	--	--
10	RZ-12-07	21911	747	1447	19001	647	1272	20437	696	1374	--	--
11	RZ-12-08	21786	448	1312	18916	388	1157	20345	418	1252	--	--
	RZ-12-08a	21792	413	1301	18920	359	1148	20350	386	1242	--	--

9	RZ-12-0 9	20528	394	1227	18012	346	1094	19399	373	1185	21503	653
12	RZ-12-0 2	24476	470	1464	20698	397	1258	22120	424	1352	--	--
	RZ-12-0 2a	24352	402	1436	20621	340	1237	22039	363	1329	--	--
13	RZ-12-0 3	24794	476	1483	20891	401	1270	22343	429	1365	--	--
14	RZ-12-0 4	25646	575	1562	21397	479	1324	22996	515	1430	--	--
15	RZ-12-0 5	24844	478	1486	20921	402	1271	22378	430	1368	24940	498
19	RZ-13-6 3	25922	488	1547	21558	405	1308	23254	437	1418	--	--
18	RZ-13-6 4	28620	538	1709	23223	436	1409	25294	475	1543	--	--
17	RZ-13-6 6	28191	530	1684	22928	431	1391	24972	469	1524	--	--
16	RZ-13-6 7	29413	480	1736	23755	387	1424	25912	423	1563	28741	620
20	RZ-16-4 9	28652	565	1720	23242	458	1417	25310	499	1552	--	--
21	RZ-16-5 0	30095	790	1881	24189	634	1533	26388	692	1681	--	--
22	RZ-16-5 2	27518	697	1708	22480	568	1416	24475	619	1550	--	--
23	RZ-16-5 4	28167	616	1711	22914	500	1413	24961	545	1548	--	--
24	RZ-16-5 5	29465	511	1747	23787	412	1433	25946	450	1572	--	--
25	RZ-16-5 6	29860	518	1771	24041	417	1449	26229	455	1590	28960	1016

Table A3. Summary statistics for Mahoma and Moulyambouli moraines. Data are as presented in Figure A1.

<i>Moraine</i>								$\chi^2 = \text{for } p \leq 0.5$
Mahoma 0								
	<i>Mean Age</i>	<i>1-Sigma Uncertainty</i>	<i>Peak Age</i>	<i>Median</i>	χ^2	χ^2 -R	χ^2 (expected)	χ^2 (expected) > χ^2 (experimental)
	17859	825	17286	17755	3.54	1.77	5.99	yes
Mahoma 1								
	<i>Mean Age</i>	<i>1-Sigma Uncertainty</i>	<i>Peak Age</i>	<i>Median</i>	χ^2	χ^2 -R	χ^2 (expected)	
	21503	653	21795	21787	2.43	0.81	7.82	yes
Mahoma 2								
	<i>Mean Age</i>	<i>1-Sigma Uncertainty</i>	<i>Peak Age</i>	<i>Median</i>	χ^2	χ^2 -R	χ^2 (expected)	
	24940	498	24768	24819	0.87	0.29	7.82	yes
Mahoma 3								
	<i>Mean Age (w/ outliers)</i>	<i>1-Sigma Uncertainty (w/ outliers)</i>	<i>Peak Age (w/ outliers)</i>	<i>Median (w/ outliers)</i>	χ^2 (w/ outliers)	χ^2 -R	χ^2 (expected)	
	28036	1498	28565	28406	9.42	3.14	7.82	no
	<i>Mean Age</i>	<i>1-Sigma Uncertainty</i>	<i>Peak Age</i>	<i>Median</i>	χ^2	χ^2 -R	χ^2 (expected)	
	28741	620	28565	28620	1.54	0.77	5.99	yes
Mahoma 4								
	<i>Mean Age</i>	<i>1-Sigma Uncertainty</i>	<i>Peak Age</i>	<i>Median</i>	χ^2	χ^2 -R	χ^2 (expected)	
	28960	1016	29563	29058	2.46	0.49	11.07	yes
Moulyambouli								
	<i>Mean Age</i>	<i>1-Sigma Uncertainty</i>	<i>Peak Age</i>	<i>Median</i>	χ^2	χ^2 -R	χ^2 (expected)	
	18753	338	18721	18691	0.64	0.21	7.82	yes

Table A4.

Age recalculations for previously reported ^{10}Be chronologies from the South American tropics. All ages are calculated using the ^{10}Be production rate of Kelly et al. (2015) and results are shown as calculated using both time-independent (“St”) scaling and time-dependent (“LSDn”) scaling. Samples marked in green were included in the age calculation. Samples marked in white are considered outliers. Arithmetic mean moraine ages are presented in bold if the moraine is the outermost moraine identified within a catchment. Arithmetic mean ages presented in italics are the outermost dated moraine within the catchment.

Farber et al., 2005										
<i>Sample ID</i>	<i>St-age</i>	<i>St-err(int)</i>	<i>St-err(ext)</i>	<i>LSD-age</i>	<i>LSD-err(int)</i>	<i>LSD-err(ext)</i>	<i>Mean Age (St)</i>	<i>± (St)</i>	<i>Mean Age (LSDn)</i>	<i>± (LSDn)</i>
<i>Farb2005-E-K-9</i>	18073	1005	1433	17164	954	1378	--	--		
Farb2005-E-HU-1	23528	696	1503	21192	627	1380	--	--		
Farb2005-E-HU-2	22349	534	1373	20397	487	1279	--	--		
Farb2005-E-HU-4	23208	570	1432	21000	516	1323	--	--		
Farb2005-E-Peru-21	23936	915	1635	21562	824	1498	23255	674	21038	487
Farb2005-D-K-6a	18543	696	1259	17431	654	1203	--	--		
Farb2005-D-K-6b	18609	895	1381	17484	841	1316	--	--		
Farb2005-D-K-8a	19661	978	1481	18341	912	1401	--	--		
Farb2005-D-K-8b	19530	880	1412	18231	821	1338	--	--		
Farb2005-D-K-2	20214	2077	2371	18907	1942	2230	--	--		
Farb2005-D-K-7	20802	946	1510	19234	874	1417	19560	885	18271	730
Farb2005-D-K-5a	29371	1402	2177	25384	1211	1907	--	--		
Farb2005-D-K-5b	28960	889	1867	25087	769	1647	29166	291	25236	210

Farb2005-D-K-4	22653	1083	1679	20717	990	1557	22653	1083	20717	990
Farb2005-D-K-3	24509	1099	1771	21971	985	1611	24509	1099	21971	985
Smith & Rodbell, 2010										
<i>Sample ID</i>	<i>St-age</i>	<i>St-err(int)</i>	<i>St-err(ext)</i>	<i>LSD-age</i>	<i>LSD-err(int)</i>	<i>LSD-err(ext)</i>	<i>Mean Age (St)</i>	\pm (St)	<i>Mean Age (LSDn)</i>	\pm (LSDn)
SmiRod2010-D-PE05-JEU-33	22456	571	1393	20291	516	1285	--	--		
SmiRod2010-D-PE05-JEU-34	21822	726	1433	19817	659	1325	--	--		
SmiRod2010-D-PE05-JEU-35	19018	901	1403	17608	834	1318	--	--		
SmiRod2010-D-PE05-JEU-36	21770	744	1439	19742	675	1329	21267	1531	19365	1196
Shakun et al., 2015										
<i>Sample ID</i>	<i>St-age</i>	<i>St-err(int)</i>	<i>St-err(ext)</i>	<i>LSD-age</i>	<i>LSD-err(int)</i>	<i>LSD-err(ext)</i>	<i>Mean Age (St)</i>	\pm (St)	<i>Mean Age (LSDn)</i>	\pm (LSDn)
Shak2015-C-MC-G-4	17414	335	1040	16514	317	1008	--	--		
Shak2015-C-MC-G-2	18045	334	1074	17075	316	1039	17730	446	16795	397
Shak2015-C-MC-G-3	18860	354	1124	17716	333	1079	18860	354	17716	333
Shak2015-C-MC-G-9	19024	359	1134	17891	338	1090	--	--		
Shak2015-C-MC-G-8	19132	376	1146	17984	353	1101	--	--		
Shak2015-C-MC-G-7	20149	543	1263	18747	505	1198	--	--		
Shak2015-C-MC-G-6	20770	486	1272	19233	450	1202	--	--		
Shak2015-C-MC-G-1	22762	1216	1772	20735	1108	1635	20367	1523	18918	1157
Shak2015-C-MC-G-5	46015	854	2756	38946	721	2381	--	--		

Shak2015-A-MC-NC-6	22200	1121	1684	20318	1026	1562	--	--		
Shak2015-A-MC-NC-5	25095	1325	1943	22179	1170	1739	23648	2047	21249	1316
Shak2015-A-MC-NC-2	51050	1845	3446	41138	1483	2819	--	--		
Shak2015-A-MC-NC-3	68385	3100	4994	58424	2642	4322	--	--		
Shak2015-A-MC-NC-4	169234	4405	10872	129500	3337	8409	--	--		
Shak2015-A-MC-NC-9	21899	962	1569	20110	883	1463	--	--		
Shak2015-A-MC-NC-10	23425	1083	1712	21193	980	1572	--	--		
Shak2015-A-MC-NC-7	24550	1059	1748	21853	942	1579	--	--		
Shak2015-A-MC-NC-8	24988	1066	1772	22122	943	1593	23716	1378	21320	896
Wesnousky et al., 2012										
<i>Sample ID</i>	<i>St-age</i>	<i>St-err(int)</i>	<i>St-err(ext)</i>	<i>LSD-age</i>	<i>LSD-err(int)</i>	<i>LSD-err(ext)</i>	<i>Mean Age (St)</i>	\pm (St)	<i>Mean Age (LSDn)</i>	\pm (LSDn)
Wesn2012-D-VEN18	21670	977	1568	20079	905	1474	21670	977	20079	905
Wesn2012-E-VEN19	21439	4280	4449	20183	4028	4195	--	--		
Wesn2012-E-VEN20	19482	1076	1540	18637	1029	1492	--	--		
Wesn2012-E-VEN21	17626	710	1224	17062	687	1204	--	--		
Wesn2012-E-VEN23	17476	563	1137	16948	546	1123	19006	1861	18208	1526
Wesn2012-A-LZ09-02	15136	1091	1387	14967	1079	1384	--	--		
Wesn2012-A-VEN26	17407	1776	2030	16974	1732	1991	--	--		
Wesn2012-A-VEN27	20451	611	1308	19523	583	1273	--	--		
Wesn2012-A-VEN28	19610	991	1487	18844	952	1449	19156	1572	18447	1320

Zech et al., 2007										
<i>Sample ID</i>	<i>St-age</i>	<i>St-err(int)</i>	<i>St-err(ext)</i>	<i>LSD-age</i>	<i>LSD-err(int)</i>	<i>LSD-err(ext)</i>	<i>Mean Age (St)</i>	\pm (St)	<i>Mean Age (LSDn)</i>	\pm (LSDn)
Zech2007b-A-SF12	22729	983	1619	20976	907	1517				
Zech2007b-A-SF13	32130	1263	2218	27899	1096	1956	27430	664 8	24438	4895
Zech2007b-C-SF32	26114	1051	1815	23319	938	1647				
Zech2007b-C-SF33	30031	968	1959	26224	845	1741	28073	277 0	24772	2054
Zech2007b-D-SF41	28381	1258	2042	25027	1108	1827				
Zech2007b-D-SF42	36039	1273	2410	31192	1100	2121				
Zech2007b-D-SF43	39236	1387	2626	34474	1217	2346	34552	557 8	30231	4796
Zech2007b-N-HH51	24649	904	1663	22634	830	1554				
Zech2007b-N-HH52	20751	723	1379	19899	693	1346	22700	275 6	21267	1934
Bromley et al., 2016										
<i>Sample ID</i>	<i>St-age</i>	<i>St-err(int)</i>	<i>St-err(ext)</i>	<i>LSD-age</i>	<i>LSD-err(int)</i>	<i>LSD-err(ext)</i>	<i>Mean Age (St)</i>	\pm (St)	<i>Mean Age (LSDn)</i>	\pm (LSDn)
NT-11-05	26112	355	1521	23192	315	1382				
NT-11-08	27804	375	1620	24419	329	1455	26958	119 6	23806	868
NT-11-13	25334	332	1473	22606	296	1345	25334	332	22606	296
NT-11-18	21608	282	1255	20120	262	1196	21608	282	20120	262
ARC-09-25	18798	257	1094	17798	244	1060				
ARC-09-26	18762	464	1158	17769	439	1119	18780	25	17784	21

Smith et al., 2005a										
<i>Sample ID</i>	<i>St-age</i>	<i>St-err(int)</i>	<i>St-err(ext)</i>	<i>LSD-age</i>	<i>LSD-err(int)</i>	<i>LSD-err(ext)</i>	<i>Mean Age (St)</i>	\pm (St)	<i>Mean Age (LSDn)</i>	\pm (LSDn)
Smit2005a-B-AL006	21682	559	1348	19835	511	1259				
Smit2005a-B-AL007	17473	442	1082	16446	416	1040	19578	297 6	18141	2396
Smit2005a-B-AL010	20817	527	1290	19191	485	1214	20817	527	19191	485
Smit2005a-B-PE01-ALC-03	19281	664	1277	17958	618	1210				
Smit2005a-B-PE01-ALC-04	20025	657	1310	18575	609	1237				
Smit2005a-B-PE01-ALC-05	26335	768	1678	22957	669	1491				
Smit2005a-B-PE01-ALC-06	19548	708	1313	18193	658	1243				
Smit2005a-B-PE01-ALC-07	35283	1012	2245	29678	850	1923	21297	337 3	19421	2371
Smit2005a-D-PE01-ANT-01	19275	683	1286	18008	638	1223	19275	683	18008	638
Smit2005a-D-PE01-ANT-02	20602	581	1302	19074	538	1229	20602	581	19074	538
Smit2005a-D-PE01-ANT-03	20678	629	1328	19141	582	1253	20678	629	19141	582
Smit2005a-D-PE01-ANT-04	21303	875	1490	19619	806	1394	21303	875	19619	806
Smit2005a-D-PE01-ANT-05	18081	613	1192	17045	577	1144				
Smit2005a-D-PE01-ANT-06	18429	572	1189	17320	537	1138	18255	246	17183	194
Smit2005a-D-PE01-ANT-07	19663	728	1329	18344	679	1261	19663	728	18344	679
Smit2005a-E-PE01-CAL-01	18577	892	1378	17436	837	1312				

Smit2005a-E-PE01-CAL-02	17840	742	1252	16840	700	1201				
Smit2005a-E-PE01-CAL-03	22123	1165	1711	20231	1065	1585	19513	2290	18169	1810
Smit2005a-E-PE01-CAL-04	17824	675	1213	16825	637	1164				
Smit2005a-E-PE01-CAL-05	16620	715	1180	15765	678	1137				
Smit2005a-E-PE01-CAL-06	17676	2037	2269	16673	1921	2150	17373	657	16421	573
Smit2005a-E-PE01-CAL-07	17450	1616	1893	16478	1525	1799	17450	1616	16478	1525
Smit2005a-F-PE01-CAL-08	19344	627	1261	18080	586	1200				
Smit2005a-F-PE01-CAL-09	20132	797	1390	18720	740	1314				
Smit2005a-F-PE01-CAL-10	22510	772	1490	20508	703	1381	21321			
Smit2005a-F-PE01-CAL-11	21510	755	1432	19777	694	1340	21375			
Smit2005a-F-PE01-CAL-12	23785	2136	2525	21367	1918	2283				
Smit2005a-F-PE01-CAL-13	20861	744	1395	19280	687	1312				
Smit2005a-F-PE01-CAL-14	22239	793	1488	20319	724	1383	21483	1512	19722	1124
Smit2005a-G-PE01-ANT-08	33078	876	2071	28125	744	1795				
Smit2005a-G-PE01-ANT-09	33241	880	2082	28248	747	1803				
Smit2005a-G-PE01-ANT-10	34862	912	2179	29503	771	1880	33727	986	28625	763
Smit2005a-G-PE01-ANT-11	38267	1114	2443	32701	950	2126				
Smit2005a-G-PE01-ANT-12	37383	1049	2369	31705	888	2046				
Smit2005a-G-PE01-ANT-13	35904	935	2243	30233	786	1925	37185	1194	31546	1242
Smit2005a-G-PE01-ANT-14	30955	833	1944	26405	710	1690				

<i>Smit2005a-G-PE01-ANT-15</i>	38573	1001	2410	33052	857	2105				
Smit2005a-I-PE02-COL-01	26764	837	1732	23449	733	1545				
Smit2005a-I-PE02-COL-02	27852	1111	1930	24240	966	1707				
Smit2005a-I-PE02-COL-03	27157	947	1807	23734	827	1606				
Smit2005a-I-PE02-COL-04	24638	880	1650	21913	782	1493				
<i>Smit2005a-I-PE02-COL-05</i>	<i>22640</i> <i>6</i>	<i>9471</i>	<i>16484</i>	<i>17695</i> <i>3</i>	<i>7310</i>	<i>12937</i>				
Smit2005a-I-PE02-COL-07	27750	864	1794	24123	750	1589	26832	130 5	23492	937
Smith et al., 2005b										
<i>Sample ID</i>	<i>St-age</i>	<i>St-err(int)</i>	<i>St-err(ext)</i>	<i>LSD-age</i>	<i>LSD-err(int)</i>	<i>LSD-err(ext)</i>	<i>Mean Age (St)</i>	\pm <i>(St)</i>	<i>Mean Age (LSDn)</i>	\pm <i>(LSDn)</i>
Smit2005b-G-MIL-00-01	37554	980	2348	33124	863	2111	--	--		
Smit2005b-G-MIL-00-02	35561	954	2233	30866	827	1976	--	--		
Smit2005b-G-MIL-00-03-D	30742	799	1918	26963	700	1716	--	--		
Smit2005b-G-MIL-00-04	41143	1497	2778	36065	1311	2475	--	--		
Smit2005b-G-MIL-00-05	17481	518	1116	16951	502	1103	--	--		
Smit2005b-G-MIL-00-06	19600	556	1240	18725	531	1208	--	--		
Smit2005b-G-MIL-00-07	31694	852	1990	27760	746	1777	30539	893 0	27208	7122
Smit2005b-H-MIL-00-08	28635	830	1823	25313	733	1642	--	--		
Smit2005b-H-MIL-00-09	28233	1101	1943	25016	975	1749	--	--		
Smit2005b-H-MIL-00-10	29867	995	1964	26232	873	1756	--	--		
Smit2005b-H-MIL-00-11	26646	772	1696	23834	690	1546	--	--		
Smit2005b-H-MIL-00-12	26969	749	1702	24073	668	1549	--	--		

Smit2005b-H-MIL-00-13	33453	888	2096	29148	773	1862	--	--		
Smit2005b-H-MIL-00-14	31665	849	1987	27753	744	1776	29353	2490	25910	1950

Table A5. Input for the Kelly et al. (2015) calibration dataset to the online calculator as described by Balco et al. (2008) and subsequently updated. Input is as formatted as provided by the calibration.ice-d.org website for use with the online calculator.

K2015-Q-40 -13.94420 -70.89360 4853 std 1.5 2.29 0.9980 0.00e+00 0;
K2015-Q-40 true_t HUANCANE2A 12200 560;
K2015-Q-40 Be-10 quartz 5.452e+05 1.342e+04 KNSTD;
K2015-Q-40a -13.94420 -70.89360 4853 std 2.8 2.29 0.9990 1.15e-03 0;
K2015-Q-40a true_t HUANCANE2A 12200 560;
K2015-Q-40a Be-10 quartz 5.652e+05 1.314e+04 KNSTD;
K2015-Q-42 -13.94500 -70.89290 4857 std 1.6 2.29 0.9960 4.51e-04 0;
K2015-Q-42 true_t HUANCANE2A 12200 560;
K2015-Q-42 Be-10 quartz 5.673e+05 9.690e+03 KNSTD;
K2015-Q-43 -13.94370 -70.89530 4844 std 1.5 2.29 0.9990 4.51e-04 0;
K2015-Q-43 true_t HUANCANE2A 12200 560;
K2015-Q-43 Be-10 quartz 5.533e+05 1.361e+04 KNSTD;
K2015-Q-44 -13.94500 -70.89540 4849 std 2.0 2.29 1.0000 0.00e+00 0;
K2015-Q-44 true_t HUANCANE2A 12200 560;
K2015-Q-44 Be-10 quartz 5.540e+05 1.364e+04 KNSTD;
K2015-Q-44a -13.94500 -70.89540 4849 std 2.9 2.29 1.0000 1.23e-03 0;
K2015-Q-44a true_t HUANCANE2A 12200 560;
K2015-Q-44a Be-10 quartz 5.779e+05 1.799e+04 KNSTD;
K2015-Q-46 -13.94630 -70.89240 4863 std 0.9 2.29 1.0000 4.51e-04 0;
K2015-Q-46 true_t HUANCANE2A 12200 560;
K2015-Q-46 Be-10 quartz 5.716e+05 1.403e+04 KNSTD;
K2015-Q-47 -13.94630 -70.89210 4865 std 2.1 2.29 1.0000 4.51e-04 0;
K2015-Q-47 true_t HUANCANE2A 12200 560;
K2015-Q-47 Be-10 quartz 5.714e+05 1.158e+04 07KNSTD;

K2015-Q-48 -13.94610 -70.89270 4862 std 3.4 2.29 0.9980 4.51e-04 0;
K2015-Q-48 true_t HUANCANE2A 12200 560;
K2015-Q-48 Be-10 quartz 5.896e+05 1.350e+04 07KNSTD;
K2015-Q-49 -13.94580 -70.89350 4851 std 5.1 2.29 1.0000 4.51e-04 0;
K2015-Q-49 true_t HUANCANE2A 12200 560;
K2015-Q-49 Be-10 quartz 5.863e+05 1.107e+04 KNSTD;
K2015-Q-83 -13.94400 -70.89230 4856 std 3.2 2.29 0.9750 0.00e+00 0;
K2015-Q-83 true_t HUANCANE2A 12200 560;
K2015-Q-83 Be-10 quartz 4.954e+05 9.280e+03 07KNSTD;
K2015-Q-83a -13.94400 -70.89230 4856 std 2.8 2.29 0.9750 4.10e-04 0;
K2015-Q-83a true_t HUANCANE2A 12200 560;
K2015-Q-83a Be-10 quartz 4.987e+05 1.118e+04 07KNSTD;
K2015-Q-135 -13.94680 -70.88620 4863 std 2.3 2.29 0.9990 4.51e-04 0;
K2015-Q-135 true_t HUANCANE2A 12200 560;
K2015-Q-135 Be-10 quartz 5.159e+05 1.150e+04 07KNSTD;
K2015-Q-136 -13.94630 -70.88650 4866 std 2.3 2.29 0.9930 4.51e-04 0;
K2015-Q-136 true_t HUANCANE2A 12200 560;
K2015-Q-136 Be-10 quartz 4.993e+05 1.196e+04 07KNSTD;
K2015-Q-137 -13.94570 -70.88550 4870 std 2.1 2.29 0.9990 4.51e-04 0;
K2015-Q-137 true_t HUANCANE2A 12200 560;
K2015-Q-137 Be-10 quartz 5.433e+05 1.020e+04 07KNSTD;
HU08-01 -13.94494 -70.89539 4854 std 7.0 2.29 0.9969 8.20e-04 2008;
HU08-01 true_t HUANCANE2A 12200 560;
HU08-01 Be-10 quartz 4.949e+05 9.314e+03 07KNSTD;
HU08-01 Be-10 quartz 4.896e+05 1.013e+04 07KNSTD;
HU08-01 Be-10 quartz 5.241e+05 1.201e+04 07KNSTD;
HU08-01 Be-10 quartz 5.390e+05 1.011e+04 07KNSTD;
HU08-02 -13.94635 -70.89241 4862 std 5.0 2.29 0.9990 4.84e-04 2008;
HU08-02 true_t HUANCANE2A 12200 560;
HU08-02 Be-10 quartz 5.003e+05 1.022e+04 07KNSTD;

HU08-02 Be-10 quartz 4.946e+05 1.557e+04 07KNSTD;
HU08-02 Be-10 quartz 5.418e+05 1.018e+04 07KNSTD;
HU08-02 Be-10 quartz 5.195e+05 9.767e+03 07KNSTD;
HU08-03 -13.94613 -70.89266 4859 std 6.0 2.29 0.9947 3.20e-04 2008;
HU08-03 true_t HUANCANE2A 12200 560;
HU08-03 Be-10 quartz 4.835e+05 9.099e+03 07KNSTD;
HU08-03 Be-10 quartz 5.265e+05 9.883e+03 07KNSTD;
HU08-04 -13.94545 -70.89280 4848 std 5.0 2.29 0.9914 8.20e-04 2008;
HU08-04 true_t HUANCANE2A 12200 560;
HU08-04 Be-10 quartz 4.977e+05 7.205e+03 07KNSTD;
HU08-04 Be-10 quartz 4.883e+05 8.239e+03 07KNSTD;
HU08-04 Be-10 quartz 5.125e+05 9.632e+03 07KNSTD;
HU08-06 -13.94454 -70.89483 4843 std 7.0 2.29 0.9993 4.84e-04 2008;
HU08-06 true_t HUANCANE2A 12200 560;
HU08-06 Be-10 quartz 5.081e+05 9.569e+03 07KNSTD;
HU08-06 Be-10 quartz 4.992e+05 7.616e+03 07KNSTD;
HU08-06 Be-10 quartz 5.009e+05 9.418e+03 07KNSTD;
HU08-10 -13.94700 -70.88693 4860 std 3.2 2.29 0.9975 4.84e-04 2008;
HU08-10 true_t HUANCANE2A 12200 560;
HU08-10 Be-10 quartz 5.142e+05 1.286e+04 07KNSTD;
HU08-10 Be-10 quartz 5.012e+05 8.335e+03 07KNSTD;
HU08-10 Be-10 quartz 5.329e+05 1.001e+04 07KNSTD;
HU08-11 -13.94715 -70.88680 4860 std 6.0 2.29 0.9990 6.56e-04 2008;
HU08-11 true_t HUANCANE2A 12200 560;
HU08-11 Be-10 quartz 5.250e+05 8.751e+03 07KNSTD;
HU08-11 Be-10 quartz 5.147e+05 6.469e+03 07KNSTD;
HU08-14 -13.94887 -70.88559 4871 std 5.0 2.29 0.9960 3.20e-04 2008;
HU08-14 true_t HUANCANE2A 12200 560;
HU08-14 Be-10 quartz 5.138e+05 9.607e+03 07KNSTD;
HU08-14 Be-10 quartz 5.078e+05 8.451e+03 07KNSTD;

HU08-15 -13.94838 -70.88537 4869 std 6.0 2.29 0.9950 6.56e-04 2008;
HU08-15 true_t HUANCANE2A 12200 560;
HU08-15 Be-10 quartz 4.929e+05 9.240e+03 07KNSTD;
HU08-15 Be-10 quartz 4.385e+05 7.900e+03 07KNSTD;
HU08-16 -13.94679 -70.88619 4867 std 6.0 2.29 0.9974 3.20e-04 2008;
HU08-16 true_t HUANCANE2A 12200 560;
HU08-16 Be-10 quartz 5.151e+05 9.598e+03 07KNSTD;
HU08-16 Be-10 quartz 4.459e+05 8.500e+03 07KNSTD;

APPENDIX B

SAMPLE INFORMATION FOR CHAPTER 4

Table B1. ^{10}Be Surface-exposure ages as described in Chapter 4. All ages are reported as calculated using both time-independent (“St”) scaling and time-dependent (“LSDn”) scaling. Arithmetic mean ages for single moraines are provided where possible, with both the standard deviation and standard error of each arithmetic mean age. Arithmetic means are calculated using ages as calculated using “St” scaling.

Mubuku Valley											
<i>Map ID</i>	<i>Landform</i>	<i>Sample ID</i>	<i>Age (St)</i>	\pm (<i>int; St</i>)	\pm (<i>ext; St</i>)	<i>Age (LSDn)</i>	\pm (<i>int; LSDn</i>)	\pm (<i>ext; LSDn</i>)	<i>Mean Age (St)</i>	<i>Std. Dev.</i>	<i>Std. Err.</i>
	Mubuku 0	RZ-16-41	1144 6	282	705	11507	284	724	--		
1	Mubuku 0	RZ-16-41 x	1117 0	277	689	11293	280	711	--		
	Mubuku 0	RZ-16-43	142 50	272	850	14045	268	856	--		
2	Mubuku 0	RZ-16-43 x	137 86	346	852	13673	343	863	--		
	Mubuku 0	RZ-16-44	132 26	547	926	13168	544	937	--		
3	Mubuku 0	RZ-16-44 x	126 01	326	783	12677	328	804	--		
										12974	1419
											819
Bujuku Valley											
<i>Map ID</i>	<i>Landform</i>	<i>Sample ID</i>	<i>Age (St)</i>	\pm (<i>int; St</i>)	\pm (<i>ext; St</i>)	<i>Age (LSDn)</i>	\pm (<i>int; LSDn</i>)	\pm (<i>ext; LSDn</i>)	<i>Mean Age (St)</i>	<i>Std. Dev.</i>	<i>Std. Err.</i>
4	Bujuku 8	RZ-16-07	219 4	286	312	2651	346	378	--		
5	Bujuku 8	RZ-16-08	138 64	404	881	13894	405	901	--		
6	Bujuku 7	RZ-16-02	167 68	313	998	16327	305	994	--		

7	Bujuku 7	RZ-16-03	153 65	373	945	15105	367	949	--			
8	Bigo Drift	RZ-16-09	1101 3	341	709	11077	343	727	--			
9	Bigo Drift	RZ-16-11	158 63	476	1015	15225	456	993	--			
10	Bigo Drift	RZ-16-13	223 73	448	1343	20507	410	125 8	--			
11	Bujuku 6	RZ-16-24	933 3	260	587	9613	268	617	--			
12	Bujuku 6	RZ-16-25	135 70	351	843	13217	342	838	--			
13	Bujuku 5	RZ-16-21	152 31	331	922	14648	318	906	--			
14	Bujuku 5	RZ-16-26	146 85	310	885	14163	299	873	--	14958	386	273
15	Bujuku 4	RZ-16-17	151 29	399	943	14585	384	928	--			
16	Bujuku 4	RZ-16-18	146 14	393	914	14118	379	901	--	14872	364	258
17	Bujuku 3	RZ-16-14	138 56	411	884	13553	402	882	--			
18	Bujuku 2	RZ-12-11	155 38	295	926	14867	282	906	--			
19	Bujuku 2	RZ-12-12	147 04	279	876	14153	269	862	--			
20	Bujuku 2	RZ-12-13	139 21	264	829	13545	257	825	--			
	Bujuku 2	RZ-12-13 x	135 49	257	807	13196	250	804	--	14721	809	467
21	Bujuku 1	RZ-12-14	140 13	295	844	13632	286	840	--			
22	Bujuku 1	RZ-12-15	140 61	231	827	13669	224	822	--			
23	Bujuku 1	RZ-12-16	143 08	280	855	13865	271	847	--	14127	158	91
	Bujuku 1											

24	Bujuku 0	RZ-12-17	1149 7	218	685	11276	214	687	--			
25	Bujuku 0	RZ-12-18	121 84	375	784	11842	365	776	--			
26	Bujuku 0	RZ-16-31	1155 1	228	691	11308	223	691	--	11744	382	221
27	Bujuku Slide	RZ-16-35	123 61	229	734	11917	221	724	--			
28	Bujuku Slide	RZ-16-36	1102 9	206	656	10931	204	664	--			
29	Bujuku Slide	RZ-16-39	1102 7	205	655	10928	204	664	--			
<u>Nyamugasani Valley</u>												
<i>Map ID</i>	<i>Landform</i>	<i>Sample ID</i>	<i>Age (St)</i>	\pm (<i>int; St</i>)	\pm (<i>ext; St</i>)	<i>Age (LSDn)</i>	\pm (<i>int; LSDn</i>)	\pm (<i>ext; LSDn</i>)		<i>Mean Age (St)</i>	<i>Std. Dev.</i>	<i>Std. Err.</i>
30	Katunda boulder	RZ-15-05	141 09	269	841	13531	258	825	--			
31	Katunda boulder	RZ-15-06	137 78	228	811	13223	219	796	--			
32	Nyamu 2	LA-2	1155 9	222	689	11268	216	687	--			
33	Nyamu 2	LA-1	127 29	278	770	12309	268	761	--			
	Nyamu 2	LA-1x	122 53	374	786	11824	361	773	--			
34	Nyamu 2	LA-3	124 91	239	745	12061	230	735	--			
35	Nyamu 2	LA-5	1178 1	224	702	11388	217	694	--			
	Nyamu 2	LA-5x	1161 7	192	683	11277	186	678	--	12140	559	279
36	Nyamu 1	RZ-12-33	1152 3	218	686	11213	212	683	--			
37	Nyamu 1	RZ-12-34	1138 1	214	677	11126	210	677	--			
38	Nyamu 1	RZ-12-36	1126 8	213	671	11058	209	673	--			
39	Nyamu 1	RZ-12-37	1114 8	232	671	10987	229	676	--	11330	160	80

40	Nyamu 0	RZ-12-38	1166 4	220	694	11297	213	687	--			
41	Nyamu 0	RZ-12-39	1104 1	209	657	10911	206	664	--			
42	Nyamu 0	RZ-12-41	1113 6	210	663	10975	207	668	--			
43	Nyamu 0	RZ-12-44	1102 0	278	681	10892	274	687	--	11215	303	152
44	Kopello boulder	KOP-1	104 54	271	649	10389	269	658	--			
45	Kopello boulder	KOP-2	1177 0	288	724	11359	278	714	--			
46	Kopello boulder	KOP-4A	120 76	335	760	11598	322	744	--			
47	Kopello boulder	KOP-5	830 2	205	511	8222	203	517	--			
48	Kopello boulder	RZ-15-12	1102 8	211	657	10895	208	664	--			

Table B2. ^{10}Be surface-exposure age calculation input for the cosmogenic surface exposure online calculator as described by Balco et al. (2008) and subsequently updated. All data are as described in Chapter 4.

Mubuku Valley												
Map ID	Landform	Sample ID	Latitude	Longitude	Elevation	Atm.	Thickness	Density	Shielding	Erosion	^{10}Be	$\pm 10\text{-Be}$
			(DD)	(DD)	(m)		(cm)	(g/cm ³)		(mm/yr)	(atoms/g)	(atoms/g)
	Mubuku 0	RZ-16-41	0.34533	29.95181	2955	std	1.4	2.65	0.965	0	178842	4397
1	Mubuku 0	RZ-16-41x	0.34533	29.95181	2955	std	1.4	2.65	0.965	0	174463	4317
	Mubuku 0	RZ-16-43	0.34547	29.95206	2975	std	2.8	2.65	0.965	0	222085	4228
2	Mubuku 0	RZ-16-43x	0.34547	29.95206	2975	std	2.8	2.65	0.965	0	214908	5369
	Mubuku 0	RZ-16-44	0.34543	29.95196	2948	std	2.1	2.65	0.942	0	199614	8225
3	Mubuku 0	RZ-16-44x	0.34543	29.95196	2948	std	2.1	2.65	0.942	0	190167	4903
Bujuku Valley												
Map ID	Landform	Sample ID	Latitude	Longitude	Elevation	Atm.	Thickness	Density	Shielding	Erosion	^{10}Be	$\pm 10\text{-Be}$
			(DD)	(DD)	(m)		(cm)	(g/cm ³)		(mm/yr)	(atoms/g)	(atoms/g)
4	Bujuku 8	RZ-16-07	0.35942	29.97108	2673	std	2.4	2.65	0.964	0	29185	3805
5	Bujuku 8	RZ-16-08	0.35855	29.97204	2630	std	2.3	2.65	0.96	0	178904	5200
6	Bujuku 7	RZ-16-02	0.361	29.96632	2776	std	2.9	2.65	0.956	0	232364	4317
7	Bujuku 7	RZ-16-03	0.3604	29.96773	2737	std	1.8	2.65	0.977	0	214817	5197
8	Bigo Drift	RZ-16-09	0.38174	29.93753	3332	std	2.7	2.65	0.957	0	205560	6352
9	Bigo Drift	RZ-16-11	0.38177	29.93755	3240	std	2.9	2.65	0.957	0	281653	8410

10	Bigo Drift	RZ-16-1 3	0.3818	29.9375 8	332 0	std	1.2	2.65	0.943	0	412826	8213
11	Bujuku 6	RZ-16-2 4	0.3855	29.9301 5	347 3	std	1.5	2.65	0.974	0	192225	5350
12	Bujuku 6	RZ-16-2 5	0.3854	29.9302 2	347 0	std	1.5	2.65	0.974	0	278834	7181
13	Bujuku 5	RZ-16-2 1	0.3859	29.9294 5	349 1	std	2.4	2.65	0.974	0	313790	6796
14	Bujuku 5	RZ-16-2 6	0.385	29.9302 3	346 5	std	1.9	2.65	0.973	0	299629	6296
15	Bujuku 4	RZ-16-1 7	0.3838 1	29.9308 1	343 6	std	3.3	2.65	0.977	0	301965	7925
16	Bujuku 4	RZ-16-1 8	0.3837	29.9308 9	343 3	std	2.1	2.65	0.974	0	293243	7853
17	Bujuku 3	RZ-16-1 4	0.3814 8	29.9319 8	334 7	std	4	2.65	0.977	0	263048	7775
18	Bujuku 2	RZ-12-1 1	0.3867 9	29.9203 7	352 6	std	1.6	2.65	0.966	0	325150	6141
19	Bujuku 2	RZ-12-1 2	0.3867 9	29.9204 7	351 4	std	0.6	2.65	0.977	0	311932	5906
20	Bujuku 2	RZ-12-1 3	0.3862 2	29.9212 6	347 3	std	0.6	2.65	0.977	0	289500	5464
	Bujuku 2	RZ-12-1 3x	0.3862 2	29.9212 6	347 3	std	0.6	2.65	0.977	0	281801	5320
21	Bujuku 1	RZ-12-1 4	0.3866	29.9216 5	345 0	std	1.3	2.65	0.972	0	284851	5967
22	Bujuku 1	RZ-12-1 5	0.3867	29.9214 3	345 4	std	0.4	2.65	0.95	0	282127	4614
23	Bujuku 1	RZ-12-1 6	0.3866 7	29.9214 4	344 3	std	0.9	2.65	0.972	0	290822	5672
	Bujuku 1											
24	Bujuku 0	RZ-12-1 7	0.3790 8	29.9067 9	371 9	std	0.9	2.65	0.955	0	263168	4976
25	Bujuku 0	RZ-12-1 8	0.3792 7	29.907	370 5	std	0.4	2.65	0.952	0	277316	8511
26	Bujuku 0	RZ-16-3 1	0.379	29.9064 9	373 0	std	2.3	2.65	0.954	0	262531	5171

27	Bujuku Slide	RZ-16-35	0.37595	29.89511	3913	std	0.8	2.65	0.901	0	292985	5412
28	Bujuku Slide	RZ-16-36	0.37596	29.89498	3913	std	0.8	2.65	0.931	0	270201	5026
29	Bujuku Slide	RZ-16-39	0.37576	29.89535	3916	std	1.4	2.65	0.929	0	268473	4988
Nyamugasani Valley												
<i>Map ID</i>	<i>Landform</i>	<i>Sample ID</i>	<i>Latitude</i>	<i>Longitude</i>	<i>Elevation</i>	<i>Atm.</i>	<i>Thickness</i>	<i>Density</i>	<i>Shielding</i>	<i>Erosion</i>	<i>10-Be</i>	<i>± 10-Be</i>
			(DD)	(DD)	(m)		(cm)	(g/cm ³)		(mm/yr)	(atoms/g)	(atoms/g)
30	Katunda boulder	RZ-15-05	0.27685	29.89385	3814	std	6.1	2.65	0.976	0	330743	6290
31	Katunda boulder	RZ-15-06	0.27712	29.89385	3817	std	2.7	2.65	0.976	0	332348	5478
32	Nyamu 2	LA-2	0.29487	29.89638	3871	std	4	2.65	0.979	0	284240	5432
33	Nyamu 2	LA-1	0.29488	29.89633	3870	std	1	2.65	0.976	0	319386	6943
	Nyamu 2	LA-1x	0.29488	29.89633	3870	std	1	2.65	0.976	0	307543	9353
34	Nyamu 2	LA-3	0.2949	29.89642	3872	std	1	2.65	0.979	0	314748	5995
35	Nyamu 2	LA-5	0.29502	29.89685	3968	std	1.4	2.65	0.978	0	309215	5862
	Nyamu 2	LA-5x	0.29502	29.89685	3968	std	1.4	2.65	0.978	0	304863	5013
36	Nyamu 1	RZ-12-33	0.30186	29.89462	3980	std	0.5	2.65	0.987	0	309180	5833
37	Nyamu 1	RZ-12-34	0.3018	29.89468	3974	std	1	2.65	0.987	0	303278	5699
38	Nyamu 1	RZ-12-36	0.30214	29.89513	3981	std	1.2	2.65	0.993	0	302551	5696
39	Nyamu 1	RZ-12-37	0.30222	29.89515	3980	std	1.5	2.65	0.993	0	298533	6206
40	Nyamu 0	RZ-12-38	0.30624	29.89303	4007	std	3.5	2.65	0.971	0	304302	5715
41	Nyamu 0	RZ-12-39	0.30551	29.89288	4001	std	0.8	2.65	0.984	0	297747	5617
42	Nyamu 0	RZ-12-41	0.30515	29.89296	4001	std	1.1	2.65	0.983	0	299071	5636

43	Nyamu 0	RZ-12-4 4	0.3050 9	29.8917 5	401 3	std	2	2.65	0.966	0	290391	7296
44	Kopello boulder	KOP-1	0.3108 5	29.8916 2	403 3	std	1.3	2.65	0.992	0	287151	7422
45	Kopello boulder	KOP-2	0.3110 8	29.8914 2	403 2	std	2	2.65	0.963	0	311917	7619
46	Kopello boulder	KOP-4A	0.3107	29.8918	403 0	std	1.8	2.65	0.963	0	320163	8864
47	Kopello boulder	KOP-5	0.3095 8	29.8927	402 2	std	3	2.65	0.963	0	217380	5345
48	Kopello boulder	RZ-15-1 2	0.3110 7	29.8911 1	402 5	std	2.1	2.65	0.97	0	293156	5592

Table B3. ¹⁰Be surface-exposure sample laboratory chemistry and processing data from Chapter 4. All ¹⁰Be/⁹Be ratios were measured at Lawrence Livermore National Laboratory Center for Accelerator Mass Spectrometry (CAMS).

Mubuku Valley											
<i>Map ID</i>	<i>Landform</i>	<i>Sample ID</i>	<i>Cathode ID</i>	<i>Quartz</i>	<i>Carrier wt.</i>	<i>Carrier Conc.</i>	<i>Sample</i>	\pm <i>Sample</i>	<i>Process Blank</i>	<i>Blank</i>	\pm <i>Blank</i>
				(g)	(mg)	(ppm)	(¹⁰ -Be/ ⁹ -Be)	(¹⁰ -Be/ ⁹ -Be)	<i>Cathode ID</i>	(¹⁰ -Be/ ⁹ -Be)	(¹⁰ -Be/ ⁹ -Be)
	Mubuku 0	RZ-16-41	BE42273	5.0387	0.1536	1.346	6.52E-14	1.60E-15	BE42279	1.05E-15	1.91E-16
1	Mubuku 0	RZ-16-41x	BE43141	3.1667	0.1548	1.349	3.96E-14	9.80E-16	BE43147	5.69E-16	1.27E-16
	Mubuku 0	RZ-16-43	BE42274	5.1408	0.1916	1.346	6.63E-14	1.26E-15	BE42279	1.05E-15	1.91E-16
2	Mubuku 0	RZ-16-43x	BE43142	3.0083	0.1576	1.349	4.55E-14	1.14E-15	BE43147	5.69E-16	1.27E-16
	Mubuku 0	RZ-16-44	BE42275	5.0369	0.1576	1.346	7.09E-14	2.92E-15	BE42279	1.05E-15	1.91E-16
3	Mubuku 0	RZ-16-44x	BE43143	3.0327	0.1562	1.349	4.10E-14	1.06E-15	BE43147	5.69E-16	1.27E-16
Bujuku Valley											
<i>Map ID</i>	<i>Landform</i>	<i>Sample ID</i>	<i>Cathode ID</i>	<i>Quartz</i>	<i>Carrier wt.</i>	<i>Carrier Conc.</i>	<i>Sample</i>	\pm <i>Sample</i>	<i>Process Blank</i>	<i>Blank</i>	\pm <i>Blank</i>
				(g)	(mg)	(ppm)	(¹⁰ -Be/ ⁹ -Be)	(¹⁰ -Be/ ⁹ -Be)	<i>Cathode ID</i>	(¹⁰ -Be/ ⁹ -Be)	(¹⁰ -Be/ ⁹ -Be)
4	Bujuku 8	RZ-16-07	BE42145	5.1013	0.3499	1.344	4.74E-15	6.18E-16	BE42147	6.18E-16	5.12E-16
5	Bujuku 8	RZ-16-08	BE42146	5.0411	0.1547	1.344	6.49E-14	1.89E-15	BE42147	6.18E-16	5.12E-16
6	Bujuku 7	RZ-16-02	BE42143	5.0669	0.2008	1.344	6.53E-14	1.21E-15	BE42147	6.18E-16	5.12E-16
7	Bujuku 7	RZ-16-03	BE42144	5.0408	0.1976	1.344	6.10E-14	1.48E-15	BE42147	6.18E-16	5.12E-16
8	Bigo Drift	RZ-16-09	BE43561	2.0904	0.204	0.957	3.29E-14	1.02E-15	BE43567	6.79E-16	2.58E-16
9	Bigo Drift	RZ-16-11	BE43562	2.0968	0.2034	0.957	4.54E-14	1.36E-15	BE43567	6.79E-16	2.58E-16

10	Bigo Drift	RZ-16-13	BE43563	2.1483	0.2039	0.957	6.80E-14	1.35E-15	BE43567	6.79E-16	2.58E-16
11	Bujuku 6	RZ-16-24	BE43569	2.1943	0.2014	0.957	3.28E-14	9.12E-16	BE43573	4.47E-16	1.32E-16
12	Bujuku 6	RZ-16-25	BE43570	2.2332	0.1996	0.957	4.88E-14	1.26E-15	BE43573	4.47E-16	1.32E-16
13	Bujuku 5	RZ-16-21	BE43568	2.2553	0.1988	0.957	5.57E-14	1.21E-15	BE43573	4.47E-16	1.32E-16
14	Bujuku 5	RZ-16-26	BE43571	2.1882	0.1999	0.957	5.13E-14	1.08E-15	BE43573	4.47E-16	1.32E-16
15	Bujuku 4	RZ-16-17	BE43565	2.0313	0.204	0.957	4.70E-14	1.23E-15	BE43567	6.79E-16	2.58E-16
16	Bujuku 4	RZ-16-18	BE43566	2.0427	0.2043	0.957	4.58E-14	1.23E-15	BE43567	6.79E-16	2.58E-16
17	Bujuku 3	RZ-16-14	BE43564	2.024	0.2038	0.957	4.09E-14	1.21E-15	BE43567	6.79E-16	2.58E-16
18	Bujuku 2	RZ-12-11	BE36868	6.3178	0.1622	1.328	1.43E-13	2.70E-15	BE36874	3.83E-16	1.42E-16
19	Bujuku 2	RZ-12-12	BE36869	4.8772	0.1628	1.328	1.05E-13	1.99E-15	BE36874	3.83E-16	1.42E-16
20	Bujuku 2	RZ-12-13	BE37992	8.0182	0.1629	1.335	1.60E-13	3.02E-15	BE37998	4.38E-16	1.49E-16
	Bujuku 2	RZ-12-13x	BE41130	8.4586	0.1639	1.341	1.62E-13	3.06E-15	BE41134	8.48E-16	2.32E-16
21	Bujuku 1	RZ-12-14	BE36870	3.3612	0.1613	1.328	6.69E-14	1.40E-15	BE36874	3.83E-16	1.42E-16
22	Bujuku 1	RZ-12-15	BE36871	6.0607	0.1629	1.328	1.18E-13	1.93E-15	BE36874	3.83E-16	1.42E-16
23	Bujuku 1	RZ-12-16	BE37993	4.4068	0.1627	1.335	8.83E-14	1.72E-15	BE37998	4.38E-16	1.49E-16
	Bujuku 1										
24	Bujuku 0	RZ-12-17	BE36872	6.7221	0.1623	1.328	1.23E-13	2.32E-15	BE36874	3.83E-16	1.42E-16
25	Bujuku 0	RZ-12-18	BE36873	4.7221	0.163	1.328	9.05E-14	2.78E-15	BE36874	3.83E-16	1.42E-16
26	Bujuku 0	RZ-16-31	BE43572	3.1557	0.1996	0.973	6.49E-14	1.28E-15	BE43573	4.47E-16	1.32E-16

27	Bujuku Slide	RZ-16-35	BE42269	30.226	0.1997	1.345	4.93E-13	9.11E-15	BE42272	1.51E-15	2.05E-16
28	Bujuku Slide	RZ-16-36	BE42270	26.1295	0.2022	1.345	3.89E-13	7.23E-15	BE42272	1.51E-15	2.05E-16
29	Bujuku Slide	RZ-16-39	BE42271	22.0332	0.2021	1.345	3.26E-13	6.05E-15	BE42272	1.51E-15	2.05E-16
Nyamugasani Valley											
<i>Map ID</i>	<i>Landform</i>	<i>Sample ID</i>	<i>Cathode ID</i>	<i>Quartz</i>	<i>Carrier wt.</i>	<i>Carrier Conc.</i>	<i>Sample</i>	\pm <i>Sample</i>	<i>Process Blank</i>	<i>Blank</i>	\pm <i>Blank</i>
				(g)	(mg)	(ppm)	(10-Be/9-Be)	(10-Be/9-Be)	<i>Cathode ID</i>	(10-Be/9-Be)	(10-Be/9-Be)
30	Katunda boulder	RZ-15-05	BE39120	4.083	0.165	1.335	9.17E-14	1.74E-15	BE39123	1.13E-15	2.18E-16
31	Katunda boulder	RZ-15-06	BE39121	4.103	0.1628	1.335	9.39E-14	1.55E-15	BE39123	1.13E-15	2.18E-16
32	Nyamu 2	LA-2	BE30979	6.5752	0.1989	1.03	1.37E-13	2.61E-15	BE30980	3.60E-16	1.09E-16
33	Nyamu 2	LA-1	BE33734	6.0074	0.1623	1.318	1.34E-13	2.92E-15	BE33740	2.87E-16	1.11E-16
	Nyamu 2	LA-1x	BE41126	8.113	0.1615	1.341	1.72E-13	5.24E-15	BE41134	8.48E-16	2.32E-16
34	Nyamu 2	LA-3	BE33735	6.0693	0.1554	1.318	1.40E-13	2.66E-15	BE33740	2.87E-16	1.11E-16
35	Nyamu 2	LA-5	BE33736	6.0111	0.1617	1.318	1.31E-13	2.47E-15	BE33740	2.87E-16	1.11E-16
	Nyamu 2	LA-5x	BE41127	8.2705	0.1644	1.341	1.71E-13	2.81E-15	BE41134	8.48E-16	2.32E-16
36	Nyamu 1	RZ-12-33	BE34160	6.1051	0.1634	1.319	1.31E-13	2.47E-15	BE34168	4.07E-16	1.44E-16
37	Nyamu 1	RZ-12-34	BE34161	6.0271	0.1625	1.319	1.28E-13	2.40E-15	BE34168	4.07E-16	1.44E-16
38	Nyamu 1	RZ-12-36	BE34162	6.005	0.1627	1.319	1.27E-13	2.39E-15	BE34168	4.07E-16	1.44E-16
39	Nyamu 1	RZ-12-37	BE34163	6.0069	0.1624	1.319	1.25E-13	2.60E-15	BE34168	4.07E-16	1.44E-16
40	Nyamu 0	RZ-12-38	BE34164	6.0051	0.1631	1.319	1.27E-13	2.39E-15	BE34168	4.07E-16	1.44E-16
41	Nyamu 0	RZ-12-39	BE34165	6.0051	0.1633	1.319	1.24E-13	2.34E-15	BE34168	4.07E-16	1.44E-16

42	Nyamu 0	RZ-12-41	BE34166	6.1877	0.1633	1.319	1.29E-13	2.42E-15	BE34168	4.07E-16	1.44E-16
43	Nyamu 0	RZ-12-44	BE34167	6.0497	0.1631	1.319	1.22E-13	3.07E-15	BE34168	4.07E-16	1.44E-16
44	Kopello boulder	KOP-1	BE30978	6.5625	0.1961	1.03	1.40E-13	3.61E-15	BE30980	3.60E-16	1.09E-16
45	Kopello boulder	KOP-2	BE33737	6.018	0.1619	1.318	1.32E-13	3.22E-15	BE33740	2.87E-16	1.11E-16
46	Kopello boulder	KOP-4 A	BE33738	6.034	0.1614	1.318	1.36E-13	3.76E-15	BE33740	2.87E-16	1.11E-16
47	Kopello boulder	KOP-5	BE33739	6.0837	0.1616	1.318	9.29E-14	2.28E-15	BE33740	2.87E-16	1.11E-16
48	Kopello boulder	RZ-15-12	BE39122	4.004	0.1637	1.335	8.04E-14	1.53E-15	BE39123	1.13E-15	2.18E-16

APPENDIX C

SAMPLE INFORMATION FOR CHAPTER 5

Table C1. ¹⁰Be Surface-exposure ages as described in Chapter 4. All ages are reported as calculated using both time-independent (“St”) scaling and time-dependent (“LSDn”) scaling.

Bujuku Valley								
<i>Map ID</i>	<i>Sample ID</i>	<i>Landform</i>	<i>Age (St)</i>	\pm (<i>int; St</i>)	\pm (<i>ext; St</i>)	<i>Age (LSDn)</i>	\pm (<i>int; LSDn</i>)	\pm (<i>ext; LSDn</i>)
1	RZ-12-21	Rampart moraine	352	30	36	361	30	37
2	RZ-12-22	Rampart moraine	269	19	24	273	19	25
3	RZ-12-24	Rampart moraine	394	20	30	406	20	31
4	RZ-12-25	Rampart moraine	454	15	30	472	16	31
Nyamugasani Valley								
<i>Map ID</i>	<i>Sample ID</i>	<i>Landform</i>	<i>Age (St)</i>	\pm (<i>int; St</i>)	\pm (<i>ext; St</i>)	<i>Age (LSDn)</i>	\pm (<i>int; LSDn</i>)	\pm (<i>ext; LSDn</i>)
5	RZ-15-10	Perched boulder	12131	115	694	11511	109	675
6	RZ-15-11	Perched boulder	11359	79	646	11013	77	642
7	RZ-15-09	Perched boulder	10923	118	628	10696	116	629
8	RZ-15-07	Perched boulder	4520	45	259	4979	49	292
9	RZ-15-08	Perched boulder	6524	123	388	6590	125	401
10	RZ-15-01	Bedrock	5008	55	287	5402	59	318
11	RZ-15-02	Bedrock	5039	55	289	5425	59	319
12	RZ-15-03	Bedrock	5679	50	324	5926	53	346

Table C2. ^{10}Be surface-exposure age calculation input for the cosmogenic surface exposure online calculator as described by Balco et al. (2008) and subsequently updated. All data are as described in Chapter 5.

Bujuku Valley												
Map ID	Sample ID	Landform	Lat.	Long.	Elev.	Atm.	Thickness	Density	Shielding	Erosion	^{10}Be	$\pm 10\text{-Be}$
			(DD)	(DD)	(m)		(cm)	(g/cm ³)		(mm/yr)	(atoms/g)	(atoms/g)
1	RZ-12-21	Rampart moraine	0.3875	29.88821	4095	std	1.5	2.65	0.909	0	9136	771
2	RZ-12-22	Rampart moraine	0.38768	29.88816	4046	std	1.2	2.65	0.909	0	6842	472
3	RZ-12-24	Rampart moraine	0.38768	29.88816	4046	std	1.3	2.65	0.909	0	10019	499
4	RZ-12-25	Rampart moraine	0.38768	29.88816	4046	std	1.5	2.65	0.909	0	11535	380
Nyamugasani Valley												
Map ID	Sample ID	Landform	Latitude	Longitude	Elev.	Atm.	Thickness	Density	Shielding	Erosion	^{10}Be	$\pm 10\text{-Be}$
			(DD)	(DD)	(m)		(cm)	(g/cm ³)		(mm/yr)	(atoms/g)	(atoms/g)
5	RZ-15-10	Perched boulder	0.32265	29.89128	4397	std	4	2.65	0.976	0	377849	3561
6	RZ-15-11	Perched boulder	0.32263	29.89132	4400	std	2	2.65	0.976	0	360114	2499
7	RZ-15-09	Perched boulder	0.32385	29.89034	4431	std	3	2.65	0.983	0	350726	3793
8	RZ-15-07	Perched boulder	0.32589	29.88928	4488	std	1.9	2.65	0.989	0	151256	1502
9	RZ-15-08	Perched boulder	0.32601	29.88953	4498	std	2	2.65	0.99	0	219198	4136
10	RZ-15-01	Bedrock	0.32793	29.88877	4509	std	1.9	2.65	0.969	0	165655	1808
11	RZ-15-02	Bedrock	0.32786	29.88887	4526	std	1.4	2.65	0.97	0	168872	1841
12	RZ-15-03	Bedrock	0.32781	29.88871	4536	std	2.8	2.65	0.97	0	188861	1676

Table C3. ^{10}Be surface-exposure sample laboratory chemistry and processing data from Chapter 5. All $^{10}\text{Be}/^9\text{Be}$ ratios were measured at Lawrence Livermore National Laboratory Center for Accelerator Mass Spectrometry (CAMS).

<u>Bujuku Valley</u>											
<i>Map ID</i>	<i>Sample ID</i>	<i>Landform</i>	<i>Cathode ID</i>	<i>Quartz</i>	<i>Carrier wt.</i>	<i>Carrier Conc.</i>	<i>Sample</i>	\pm <i>Sample</i>	<i>Process Blank</i>	<i>Blank</i>	\pm <i>Blank</i>
				(g)	(mg)	(ppm)	($^{10}\text{Be}/^9\text{Be}$)	($^{10}\text{Be}/^9\text{Be}$)	<i>Cathode ID</i>	($^{10}\text{Be}/^9\text{Be}$)	($^{10}\text{Be}/^9\text{Be}$)
1	RZ-12-21	Rampart moraine	BE43754	16.1727	0.2013	0.957	1.15E-14	9.69E-16	BE43758	1.64E-15	3.54E-16
2	RZ-12-22	Rampart moraine	BE43755	32.3243	0.2006	0.957	1.72E-14	1.19E-15	BE43758	1.64E-15	3.54E-16
3	RZ-12-24	Rampart moraine	BE43756	23.8116	0.2013	0.957	1.85E-14	9.22E-16	BE43758	1.64E-15	3.54E-16
4	RZ-12-25	Rampart moraine	BE43757	40.0454	0.201	0.957	3.59E-14	1.18E-15	BE43758	1.64E-15	3.54E-16
<u>Nyamugasani Valley</u>											
<i>Map ID</i>	<i>Sample ID</i>	<i>Landform</i>	<i>Cathode ID</i>	<i>Quartz</i>	<i>Carrier wt.</i>	<i>Carrier Conc.</i>	<i>Sample</i>	\pm <i>Sample</i>	<i>Process Blank</i>	<i>Blank</i>	\pm <i>Blank</i>
				(g)	(mg)	(ppm)	($^{10}\text{Be}/^9\text{Be}$)	($^{10}\text{Be}/^9\text{Be}$)	<i>Cathode ID</i>	($^{10}\text{Be}/^9\text{Be}$)	($^{10}\text{Be}/^9\text{Be}$)
5	RZ-15-10	Perched boulder	BE39810	100.9451	0.0907	1.338	4.70E-12	4.43E-14	BE39812	3.81E-15	6.16E-16
6	RZ-15-11	Perched boulder	BE39811	102.028	0.091	1.338	4.52E-12	3.13E-14	BE39812	3.81E-15	6.16E-16
7	RZ-15-09	Perched boulder	BE39809	100.5729	0.0916	1.338	4.31E-12	4.66E-14	BE39812	3.81E-15	6.16E-16
8	RZ-15-07	Perched boulder	BE39808	101.2921	0.0881	1.338	1.95E-12	1.93E-14	BE39812	3.81E-15	6.16E-16
9	RZ-15-08	Perched boulder	BE40319	12.014	0.165	1.34	1.78E-13	3.36E-15	BE40308	7.22E-16	1.41E-16
10	RZ-15-01	Bedrock	BE39531	100.5702	0.0961	1.337	1.94E-12	2.12E-14	BE39534	7.00E-15	5.81E-16
11	RZ-15-02	Bedrock	BE39532	100.7899	0.0967	1.337	1.97E-12	2.15E-14	BE39534	7.00E-15	5.81E-16
12	RZ-15-03	Bedrock	BE39533	101.3296	0.093	1.337	2.30E-12	2.04E-14	BE39534	7.00E-15	5.81E-16

REFERENCES

Abruzzi, S.A.R.i.D.d., 1907. The snows of the Nile. *Geography Journal* 29, 121-147.

Ahn, J., Brook, E.J., 2008. Atmospheric CO₂ and Climate on Millennial Time Scales During the Last Glacial Period. *Science* 322, 83-85.

Anderson, B., Mackintosh, A., 2006. Temperature change is the major driver of late-glacial and Holocene glacier fluctuations in New Zealand. *Geology* 34, 121-124.

Anderson, R.F., Ali, S., Bradtmiller, L.I., Nielsen, S.H.H., Fleisher, M.Q., Anderson, B.E., Burckle, L.H., 2009. Wind-Driven Upwelling in the Southern Ocean and the Deglacial Rise in Atmospheric CO₂. *Science* 323, 1443–1448.

Baker, P.A., Seltzer, G.O., Fritz, S.C., Dunbar, R.B., Grove, M.J., 2001. The history of South American tropical precipitation for the past 25,000 years. *Science* 291, 640-643.

Balco, G., Stone, J. O. H., Porter, S. C., Caffee, M. W., 2002. Cosmogenic-nuclide ages for New England coastal moraines, Martha's Vineyard and Cape Cod, Massachusetts, USA. *Quaternary Science Reviews* 21, 2127–2135.

Balco, G., Stone, J.O., Lifton, N.A., Dunai, T.J., 2008. A complete and easily accessible means of calculating surface exposure ages or erosion rates from ^{10}Be and ^{26}Al measurements. *Quaternary Geochronology* 3, 174–195.

Balco, G., Briner, J., Finkel, R.C., Rayburn, J.A., Ridge, J.C., Schaefer, J.M., 2009. Regional beryllium-10 production rate calibration for late-glacial northeastern North America. *Quaternary Geochronology* 4, 93–107.

Bar-Matthews, M., Ayalon, A., Kaufman, A., Wasserburg, G.J., 1999. The Eastern Mediterranean paleoclimate as a reflection of regional events: Soreq cave, Israel. *Earth and Planetary Science Letters* 166, 85-95.

Bauer, F.U., Glasmacher, U.A., Ring, U., Schumann, A., Nagudi, B., 2010. Thermal and exhumation history of the central Rwenzori Mountains, Western Rift of the East African Rift system, Uganda. *International Journal of Earth Sciences* 99, 1575-1597.

Bereiter, B., Eggleston, S., Schmitt, J., Nehrbass-Ahles, C., Stocker, T. F., Fischer, H., Kipfstuhl, S., Chappellaz, J., 2015. Revision of the EPICA Dome C CO_2 record from 800 to 600 kyr before present. *Geophysical Research Letters* 42, 542-549.

Berger, A., Loutre, M. F., 1991. Insolation values for the climate of the last 10 million years. *Quaternary Science Reviews* 10, 297-317.

Berger, A., Loutre, M.F., Mélice, J.L., 2006. Equatorial insolation: from precession harmonics to eccentricity frequencies. *Climate of the Past* 2, 131-136.

Bergström, E., 1955. British Ruwenzori Expedition, 1952 Glaciological Observations—Preliminary Report. *Journal of Glaciology* 2, 469-476.

Berke, M.A., Johnson, T.C., Werne, J.P., Schouten, S., Damsté, J.S.S., 2012. A mid Holocene thermal maximum at the end of the African Humid Period. *Earth and Planetary Science Letters* 351-352, 95–104.

Berke, M.A., Johnson, T.C., Werne, J.P., Livingstone, D.A., Grice, K., Schouten, S., Damsté, J.S.S., 2014. Characterization of the last deglacial transition in tropical East Africa: Insights from Lake Albert. *Palaeogeography, Palaeoclimatology, Palaeoecology* 409, 1-8.

Beuning, K.R.M., Kelts, K.R., Stager, J.C., 1998. Abrupt climatic changes associated with the arid Younger Dryas interval in Africa. In Lehmen, J. (Ed.) *Environmental Change and Response in East African Lakes*. Dordrecht, The Netherlands, Kluwer Academic Publishers, 147-156.

Blard, P.H., Braucher, R., Lavé, J., Bourlès, D., 2013. Cosmogenic ^{10}Be production rate calibrated against ^3He in the high Tropical Andes (3800–4900 m, 20–22° S). *Earth and Planetary Science Letters* 382, 140–149.

Boccaletti, G., Pacanowski, R.C., Philander, G.H., Fedorov, A.V., 2004. The thermal structure of the upper ocean. *Journal of Physical Oceanography* 34, 888-902.

Böhm, E., Lippold, J., Gutjahr, M., Frank, M., Blaser, P., Antz, B., Fohlmeister, J., Frank, N., Andersen, M. B., Deininger, M., 2014. Strong and deep Atlantic meridional overturning circulation during the last glacial cycle. *Nature* 517, 1–17.

Borchers, B., Marrero, S., Balco, G., Caffee, M., Goehring, B., Lifton, N., Nishiizumi, K., Phillips, F., Schaefer, J., Stone, J., 2016. Geological calibration of spallation production rates in the CRONUS-Earth project. *Quaternary Geochronology* 31, 188-198.

Bradley, R.S., Vuille, M., Diaz, H.F., Vergara, W., 2006. Threats to water supplies in the tropical Andes. *Science* 312, 1755-1756.

Bradt Miller, L.I., Anderson, R.F., Fleischer, M.Q., Burckle, L.H., 2006. Diatom productivity in the equatorial Pacific Ocean from the last glacial period to the present: A test of the silicic acid leakage hypothesis. *Paleoceanography* 21, PA4201.

Broecker, W.S., Denton, G.H., 1989. The role of ocean-atmosphere reorganizations in glacial cycles. *Geochimica et Cosmochimica Acta* 53, 2465-2501.

Bromley, G.R.M., Schaefer, J.M., Hall, B.L., Rademaker, K.M., Putnam, A.E., Todd, C.E., Hegland, M., Winckler, G., Jackson, M.S., Strand, P.D., 2016. A cosmogenic ^{10}Be

chronology for the local last glacial maximum and termination in the Cordillera Oriental, southern Peruvian Andes: Implications for the tropical role in global climate. *Quaternary Science Reviews* 148, 54–67.

Bush, A., Philander, S., 1998. The role of ocean-atmosphere interactions in tropical cooling during the last glacial maximum. *Science* 279, 1341–1344.

Carcaillet, J., Angel, I., Carrillo, E., Audemard, F.A., Beck, C., 2013. Timing of the last deglaciation in the Sierra Nevada of the Mérida Andes, Venezuela. *Quaternary Research* 80, 482–494.

Chiang, J.C., Sobel, A.H., 2002. Tropical tropospheric temperature variations caused by ENSO and their influence on the remote tropical climate. *Journal of Climate* 15, 2616-2631.

Clark, D.H., Bierman, P.R., Larsen, P., 1995. Improving in situ cosmogenic chronometers. *Quaternary Research* 44, 367–377.

Clark, P.U., Dyke, A.S., Shakun, J.D., Carlson, A.E., Clark, J., Wohlfarth, B., Mitrovica, J.X., Hostetler, S.W., McCabe, A.M., 2009. The last glacial maximum. *Science* 325, 710-714.

Clark, P.U., Shakun, J.D., Baker, P.A., Bartlein, P.J., Brewer, S., Brook, E., Carlson, A.E., Cheng, H., Kaufman, D.S., Liu, Z., Marchitto, T.M., 2012. Global climate evolution during the last deglaciation. *Proceedings of the National Academy of Sciences* 109, 1134-1142.

Cullen, N.J., Sirguey, P., Mölg, T., Kaser, G., Winkler, M., Fitzsimons, S.J., 2013. A century of ice retreat on Kilimanjaro: the mapping reloaded. *The Cryosphere Discussions* 6, 4233–4265.

D'agostino, R.A., Lionello, P., Adam, O., Schneider, T., 2017. Factors controlling Hadley circulation changes, from the Last Glacial Maximum to the end of the 21st century. *Geophysical Research Letters* 44, 8585-8591.

deMenocal, P., Ortiz, J., Guilderson, T., Adkins, J., Sarnthein, M., Baker, L. Yarusinsky, M., 2000. Abrupt onset and termination of the African Humid Period: rapid climate responses to gradual insolation forcing. *Quaternary Science Reviews* 19, 347-361.

Denton, G., Alley, R., Comer, G., Broecker, W., 2005. The role of seasonality in abrupt climate change. *Quaternary Science Reviews* 24, 1159–1182.

Denton, G. H., Anderson, R. F., Toggweiler, J. R., Edwards, R. L., Schaefer, J. M., Putnam, A. E., 2010. The Last Glacial Termination. *Science* 328, 1652–1656.

Deplazes, G., Lükge, A., Peterson, L.C., Timmerman, A., Hamann, Y., Hughen, K.A., Röhl, U., Laj, C., Cane, M.A., Sigman, D.M., Haug, G.H., 2013. Links between tropical rainfall and North Atlantic climate during the last glacial period. *Nature Geoscience* 6, 213.

Dorman, L. I., Valdés-Galicia, J. F., Dorman, I. V., 1999. Numerical simulation and analytical description of solar neutron transport in the Earth's atmosphere, *Journal of Geophysical Research* 104, 22417–22426.

Dunai, T.J., 2010. *Cosmogenic Nuclides: Principles, Concepts and Applications in the Earth Surface Sciences*. Cambridge.

Dunne, J., Elmore, D., Muzikar, P., 1999. Scaling factors for the rates of production of cosmogenic nuclides for geometric shielding and attenuation at depth on sloped surfaces. *Geomorphology* 27, 3–11.

Dyez, K.A., Ravelo, A.C., 2013. Late Pleistocene tropical Pacific temperature sensitivity to radiative greenhouse gas forcing. *Geology* 41, 23-26.

Farber, D. L., Hancock, G. S., Finkel, R. C., Rodbell, D. T., 2005. The age and extent of tropical alpine glaciation in the Cordillera Blanca, Peru. *Journal of Quaternary Science* 20, 759–776.

Favier, V., Wagnon, P., Ribstein, P., 2004. Glaciers of the outer and inner tropics: A different behaviour but a common response to climatic forcing. *Geophysical Research Letters* 31, LI6403.

Fedorov, A.V., Burls, N.J., Lawrence, K.T., Peterson, L.C., 2015. Tightly linked zonal and meridional sea surface temperature gradients over the past five million years. *Nature Geoscience* 8, 975-980.

Foster, P., 2001. The potential negative impacts of global climate change on tropical montane cloud forests. *Earth Science Reviews* 55, 73-106.

Fudge, T.J., Steig, E.J., Markle, B.R., Schoenemann, S.W., Ding, Q., Taylor, K.C., McConnell, J.R., Brook, E.J., Sowers, T., White, J.W., Alley, R.B., 2013. Onset of deglacial warming in West Antarctica driven by local orbital forcing. *Nature* 500, 440-444.

Gabrielli, P., Hardy, D.R., Kehrwald, N., Davis, M., Cozzi, G., Turetta, C., Barbante, C., Thompson, L.G., 2014. Deglaciaded areas of Kilimanjaro as a source of volcanic trace elements deposited on the ice cap during the late Holocene. *Quaternary Science Reviews* 93, 1–10.

Garcin, Y., Vincens, A., Williamson, D., Buchet, G., Guiot, J., 2007. Abrupt resumption of the African Monsoon at the Younger Dryas—Holocene climatic transition. *Quaternary Science Reviews* 26, 690-704.

Gasse, F., 2000. Hydrological changes in the African tropics since the Last Glacial Maximum. *Quaternary Science Reviews* 19, 198-211.

Glasser, N.F., Clemmens, S., Schnabel, C., Fenton, C.R., McHargue, L., 2009. Tropical glacier fluctuations in the Cordillera Blanca, Peru between 12.5 and 7.6ka from cosmogenic ^{10}Be dating. *Quaternary Science Reviews* 28, 3448–3458.

Gosse, J.C., Phillips, F.M., 2001. Terrestrial in situ cosmogenic nuclides: theory and application. *Quaternary Science Reviews* 20, 1475–1560.

Gregory, J.W., 1894. The glacial geology of Mount Kenya. *Journal of the Geological Society* 50, 515-530.

Hall et al., 2009. Geochronology of Quaternary glaciations from the tropical Cordillera Huayhuash, Peru. *Quaternary Science Reviews* 28, 2991-3009.

Hamilton, A.C., Perrott, R.A., 1978. Date of deglaciation of Mount Elgon. *Nature* 273, 49.

Hamilton, A.C., 1982. Environmental history of East Africa: a study of the Quaternary. Academic Press, London.

Hastenrath, S., 1995. Glacier recession on Mount Kenya in the context of the global tropics. *Bulletin Institute Francais Études Andines* 633–638.

He, F., Shakun, J.D., Clark, P.U., Carlson, A.E., Liu, Z., Otto-Bliesner, B.L., Kutzbach, J.E., 2013. Northern Hemisphere forcing of Southern Hemisphere climate during the last deglaciation. *Nature* 494, 81-85.

Held, I.M., Hou, A.Y., 1980. Nonlinear axially symmetric circulations in a nearly inviscid atmosphere. *Journal of the Atmospheric Sciences* 37, 515-533.

Heyman, J., Applegate, P.J., Blomdin, R., Gribenski, N., Harbor, J.M., Stroeven, A.P., 2016. Boulder height - exposure age relationships from a global glacial ¹⁰Be compilation. *Quaternary Geochronology* 34, 1–11.

Huybers, P., Denton, G., 2008. Antarctic temperature at orbital timescales controlled by local summer duration. *Nature Geoscience* 1, 787–792.

Imbrie, J., Hays, J.D., Martinson, D.G., McIntyre, A., Mix, A.C., Morley, J.J., Pisias, N.G., Prell, W.L., Shackleton, N.J., 1984. The orbital theory of Pleistocene climate: support from a revised chronology of the marine d18O record.

Ivory, S.J., Russell, J., 2017. Lowland forest collapse and early human impacts at the end of the African Humid Period at Lake Edward, equatorial East Africa. *Quaternary Research* 89, 7-20.

Johansson, L., Holmgren, K., 1985. Dating of a moraine on Mount Kenya. *Geografiska Annaler Series A Physical Geography* 67, 123-128.

Jomelli, V., Khodri, M., Favier, V., Brunstein, D., Ledru, M.-P., Wagnon, P., Blard, P.-H., Sicart, J.-E., Braucher, R., Grancher, D., Bourlès, D.L., Braconnot, P., Vuille, M., 2011. Irregular tropical glacier retreat over the Holocene epoch driven by progressive warming. *Nature*, 474, 196–199.

Jomelli, V., Favier, V., Vuille, M., Braucher, R., Martin, L., Blard, P.-H., Colose, C., Brunstein, D., He, F., Khodri, M., Bourlès, D.L., Leanni, L., Rinterknecht, V., Grancher, D., Francou, B., Ceballos, J.L., Fonseca, H., Liu, Z., Otto-Bleisner, L., 2014. A major advance of tropical Andean glaciers during the Antarctic cold reversal. *Nature* 513, 224-228.

Jomelli, V., Martin, L., Blard, P.H., Favier, V., Vuillé, M., Ceballos, J.L., 2017. Revisiting the Andean tropical glacier behavior during the Antarctic cold reversal. *Cuadernos de Investigación Geográfica* 43, 629-648.

Karlén, W., Fastook, J.L., Holmgren, K., 1999. Glacier Fluctuations on Mount Kenya since-6000 Cal. Years BP: Implications for Holocene Climatic Change in Africa. *Ambio* 28, 409-418.

Kaser, G., Noggler, B., 1996. Glacier fluctuations in the Ruwenzori Range (East Africa) during the 20th century: A preliminary report. *Zeitschrift für Gletscherkunde und Glazialgeologie* 32, 109-117.

Kaser, G., 2001. Glacier-climate interaction at low latitudes. *Journal of Glaciology* 47, 195–204.

Kaser, G., Osmatson, H., 2002. Tropical Glaciers. Cambridge, Cambridge University Press, 207 pp.

Kaser, G., Molg, T., Cullen, N.J., Hardy, D.R., Winkler, M., 2010. Is the decline of ice on Kilimanjaro unprecedented in the Holocene? *The Holocene* 20, 1079–1091.

Kelly, M.A., 2003. The Late Würmian Age in the Western Swiss Alps: Last Glacial Maximum (LGM) Ice-surface Reconstruction and ¹⁰Be Dating of Late-glacial Features (Doctoral dissertation, Verlag nicht ermittelbar).

Kelly, M.A., Russell, J.M., Baber, M.B., Howley, J.A., Loomis, S.E., Zimmerman, S., Nakileza, R., Lukaye, J., 2014. Expanded glaciers during a dry and cold Last Glacial Maximum in equatorial East Africa. *Geology* 42, 519-522.

Kelly, M.A., Lowell, T.V., Applegate, P.J., Phillips, F.M., Schaefer, J.M., Smith, C.A., Kim, H., Leonard, K.C., Hudson, A.M., 2015. A locally calibrated, late glacial ^{10}Be production rate from a low-latitude, high-altitude site in the Peruvian Andes. *Quaternary Geochronology* 26, 1–16.

Koutavas, A., Lynch-Stieglitz, J., Marchitto, T.M., Sachs, J.P., 2002. El Niño-like pattern in ice age tropical Pacific sea surface temperature. *Science* 297, 226–230.

Koutavas, A., Joannides, S., 2012. El Niño-Southern Oscillation extrema in the Holocene and Last Glacial Maximum. *Paleoceanography* 27, PA4208.

Kurz, M.D., Colodner, D., Trull, T.W., Moore, R.B., O'Brien, K., 1990. Cosmic ray exposure dating with in situ produced cosmogenic ^3He : Results from young Hawaiian lava flows. *Earth and Planetary Science Letters* 97, 177–189.

Lal, D., 1991. Cosmic ray labeling of erosion surfaces: in situ nuclide production rates and erosion models. *Earth and Planetary Science Letters* 104, 424–439.

Lambeck, K., Rouby, H., Purcell, A., Sun, Y., Sambridge, M., 2014. Sea level and global ice volumes from the Last Glacial Maximum to the Holocene. *Proceedings of the National Academy of Sciences* 111, 15296–15303.

Lea, D.W., Pak, D.K., Peterson, L.C., Hughen, K.A., 2003. Synchronicity of Tropical and High-Latitude Atlantic Temperatures over the Last Glacial Termination. *Science* 301, 1361-1364.

Lea, D.W., 2004. The 100,000-yr cycle in tropical SST, greenhouse forcing, and climate sensitivity. *Journal of Climate* 17, 2170-2179.

Lentini, G., Cristofanelli, P., Duchi, R., Marinoni, A., Verza, G., Vuillermoz, E., Toffolon, R., Bonasoni, P., 2011. Mount Rwenzori (4750 m a.s.l., Uganda): Meteorological characterization and air-mass transport analysis. *Geografia Fisica e Dinamica Quaternaria* 34, 183-193.

Licciardi, J.M., Kurz, M.D., Clark, P.U., Brook, E.J., 1999. Calibration of cosmogenic ^3He production rates from Holocene lava flows in Oregon, USA, and effects of the Earth's magnetic field. *Earth and Planetary Science Letters* 172, 261–271.

Licciardi, J.M., Schaefer, J.M., Taggart, J.R., Lund, D.C., 2009. Holocene Glacier Fluctuations in the Peruvian Andes Indicate Northern Climate Linkages. *Science* 325, 1677–1679.

Lifton, N., Sato, T., Dunai, T.J., 2014. Scaling in situ cosmogenic nuclide production rates using analytical approximations to atmospheric cosmic-ray fluxes. *Earth Planetary Science Letters* 386, 149-160.

Lifton, N., 2016. Implications of two Holocene time-dependent geomagnetic models for cosmogenic nuclide production rate scaling. *Earth and Planetary Science Letters* 433, 257–268.

Livingstone, D.M., 1962. Age of deglaciation in the Ruwenzori Range, Uganda. *Nature* 194, 859-860.

Livingstone, D.A., 1967. Postglacial vegetation of the Ruwenzori Mountains in equatorial Africa. *Ecological Monographs* 37, 25-52.

Loomis, S.E., Russell, J.M., Ladd, B., Street-Perrott, F. A., Sinninghe Damsté, J.S., 2012. Calibration and application of the branched GDGT temperature proxy on East African lake sediments. *Earth and Planetary Science Letters* 375-378, 277-288.

Loomis, S.E., Russell, J.M., Verschuren, D., Morrill, C., De Cort, G., Sinninghe Damsté, J. S., Olago, D., Eggermont, H., Street-Perrott, F.A., Kelly, M.A., 2017. The tropical lapse rate steepened during the Last Glacial Maximum. *Science Advances* 3, e1600815.

Lu, J., Vecchi, G.A., Reichler, T., 2007. Expansion of the Hadley cell under global warming. *Geophysical Research Letters* 34, L06805.

Mahaney, W.C., 1981. The climate of Mount Kenya and Kilimanjaro. In: *Guide to Mounts Kenya and Kilimanjaro*. Allan I. (ed.) Mountain Club of Kenya, Nairobi, 36-38.

Mahaney, W.C., n.d. 1989. *Quaternary and Environmental Research on East African Mountains*. CRC Press.

Marcott, S.A., Bauska, T.K., Buizert, C., Steig, E.J., Rosen, J.L., Cuffey, K.M., Fudge, T.J., Severinghaus, J.P., Ahn, J., Kalk, M.L., McConnell, J.R., Sowers, T., Taylor, K.C., White, J.W.C., Brook, E.J., 2014. Centennial-scale changes in the global carbon cycle during the last deglaciation. *Nature* 514, 616-619.

Mark, B.G., Stansell, N.D., Zeballos, G., 2017. The last deglaciation of Peru and Bolivia. *Cuadernos de Investigacion Geografica* 43, 591–632.

Martínez-Botí, M.A., Marino, G., Foster, G.L., Ziveri, P., Henehan, M.J., Rae, J.W.B., Mortyn, P.G., Vance, D., 2015. Boron isotope evidence for oceanic carbon dioxide leakage during the last deglaciation. *Nature* 518, 219–222.

May, J. H., Zech, J., Zech, R., Preusser, F., Argollo, J., Kubik, P.W., Veit, H., 2011. Reconstruction of a complex late Quaternary glacial landscape in the Cordillera de Cochabamba (Bolivia) based on a morphostratigraphic and multiple dating approach. *Quaternary Research* 76, 106-118.

McConnell, R.B., 1959. Outline of the geology of the Ruwenzori Mountains, a preliminary account of the results of the British Ruwenzori expedition, 1951-1952. *Overseas Geology and Mineral Resources* 7, 245-268.

McIntyre, A., Molino, B., 1996. Forcing of Atlantic equatorial and subpolar millennial cycles by precession. *Science* 274, 1867-1870.

McManus, J.F., Francois, R., Gherardi, J.M., Keigwin, L.D., Brown-Leger, S., 2004. Collapse and rapid resumption of Atlantic meridional circulation linked to deglacial climate changes. *Nature* 428, 834-837.

Meader, M., 1937. *From the University of Wisconsin Milwaukee AGSL Photo Library* [<https://collections.lib.uwm.edu/digital/collection/agsafrica/id/358/rec/102>]

Mercer, J. H., 1984. Simultaneous climatic change in both hemispheres and similar bipolar interglacial warming: Evidence and implications. *American Geophysical Union*, 307-313.

Milankovitch, M.K., 1941. Kanon der Erdbestrahlung und seine Anwendung auf das Eiszeitenproblem. *Royal Serbian Academy Special Publication* 133, 1-633.

Mohtadi, M., Prange, M., Oppo, D.W., De Pol-Holz, R., Merkel, U., Zhang, X., Steinke, S., Lückhe, A., 2014. North Atlantic forcing of tropical Indian Ocean climate. *Nature* 509, 76-80.

Mölg, T., Georges, C., Kaser, G., 2003. The contribution of increased incoming shortwave radiation to the retreat of the Rwenzori glaciers, East Africa, during the 20th century. *International Journal of Climatology* 23, 291-303.

Mölg, T., Rott, H., Kaser, G., Fischer, A., Cullen, N.J., 2006. Comment on “Recent glacial recession in the Rwenzori Mountains of East Africa due to rising air temperature”. *Geophysical Research Letters* 33, L20404.

Monnin, E., Indermühle, A., Dällenbach, A., Flückiger, J., Stauffer, B., Stocker, T.F., Raynaud, D., Barnola, J.M., 2001. Atmospheric CO₂ concentrations over the last glacial termination. *Science* 291, 112-114.

Mosblech, N.A.S., Bush, M.B., Gosling, W.D., Hodell, D., Thomas, L., van Calsteren, P., Correa-Metrio, A., Valencia, B.G., Curtis, J., van Woesik, R., 2012. North Atlantic forcing of Amazonian precipitation during the last ice age. *Nature Geoscience* 5, 817-820.

Nicholson, S.E., Yin, X., 2001. Rainfall conditions in equatorial East Africa during the nineteenth century as inferred from the record of Lake Victoria. *Climatic Change* 48, 1-12.

Nishiizumi, K., Winterer, E.L., Kohl, C.P., Klein, J., Middleton, R., Lal, D., Arnold, J.R., 1989. Cosmic ray production rates of ^{10}Be and ^{26}Al in quartz from glacially polished rocks. *Journal of Geophysical Research* 94, 17907–17915.

Nishiizumi, K., Imamura, M., Caffee, M.W., Southon, J.R., Finkel, R.C., McAninch, J., 2007. Absolute calibration of Be-10 AMS standards. *Nuclear Instruments and Methods in Physics Research Section B* 285B, 403-413.

Noell, A.C., Abbey, W.J., Anderson, R.C., Ponce, A., 2014. Radiocarbon dating of glacial dust layers and soils at Kilimanjaro's Northern Ice Field. *The Holocene* 24, 1398-1405.

North Greenland Ice Core Project members. 2004. High-resolution record of Northern Hemisphere climate extending into the last interglacial period. *Nature* 431, 147-151.

Novello, V.F., Cruz, F.W., Vuille, M., Stríkis, N.M., Edwards, R.L., Cheng, H., Emerick, S., de Paula, M.S., Li, X., de S Barreto, E., Karmann, I., Santos, R.V., 2017. A high-resolution history of the South American Monsoon from Last Glacial Maximum to the Holocene. *Scientific Reports* 7, 44267.

Oerlemans, J., 2005. Extracting a climate signal 169 from glacial records. *Science* 308, 675-677.

Osmatson, H., 1965. The past and present climate and vegetation of the Ruwenzori and its neighborhood. Ph.D. Thesis, Oxford University. 140 pp.

Osmatson, H., 1989. Glaciers, glaciations, and equilibrium line altitudes on the Rwenzori. In Mahaney, W.C. (Ed.) Quaternary and environmental research on East African mountains. Rotterdam, Balkema, 31-104.

Osmaston, H., 2006. Guide to the Rwenzori: Mountains of the Moon. The Rwenzori Trust, 288 pp.

Paillard, D., 2015. Quaternary glaciations: from observations to theories. *Quaternary Science Reviews* 107, 11–24.

Peixoto, J.P., Oort, A.H., 1992. The physics of climate. American institute of Physics, 520 pp.

Perrott, R.A., 1982. A high altitude pollen diagram from Mount Kenya: Its implications for the history of glaciation. In: Coetzee J.A. and van Zinderen Bakker, E.M. (eds). *Paleoecology of Africa* 14, 77-83.

Pierrehumbert, R.T., 1995. Thermostats, radiator fins, and the local runaway greenhouse. *Journal of the Atmospheric Sciences* 52, 1784-1806.

Pierrehumbert, R.T., 1999. Climate change and the tropical Pacific: The sleeping dragon wakes. *Proceedings of the National Academy of Sciences* 97, 1355-1358.

Pierrehumbert, R. T., 2002. The hydrologic cycle in deep-time climate problems. *Nature* 419, 191-198.

Plug, L.J., Gosse, J.C., McIntosh, J.J., Bigley, R. Attenuation of cosmic ray flux in temperate forest. *Journal of Geophysical Research* 112, F02022.

Powers, L.A., Johnson, T.C, Werne, J.P., Castaneda, I.S., Hopmans, E.S., Damsté, J.S.S., Schouten, S., 2005. Large temperature variability in the southern African tropics since the Last Glacial Maximum. *Geophysical Research Letters* 32, L08706.

Prinz, R. Nicholson, L. Kaser, G., 2012. Variations of the Lewis Glacier, Mount Kenya, 2004–2012. *Erdkunde* 66, 255–262.

Putnam, A.E., Denton, G.H., Schaefer, J.M., Barrell, D.J.A., Andersen, B.G., Finkel, R.C., Schwartz, R., Doughty, A.M., Kaplan, M.R., Schlüchter, C., 2010. Glacier advance in southern middle-latitudes during the Antarctic Cold Reversal. *Nature Geoscience* 3, 700–704.

Reimer, P.J., Bard, E., Bayliss, A., Beck, J.W., Blackwell, P.G., Ramsey, C.B., Buck, C.E., Cheng, H., Edwards, R.L., Friedrich, M., Grootes, P.M., 2013. IntCal13 and Marine13 radiocarbon age calibration curves 0–50,000 years cal BP. *Radiocarbon* 55, 869-1887.

Rhodes, R. H., Brook, E. J., Chiang, J. H. C., Blunier, T., Maselli, O. J., McConnell, J. R., Romanini, D., Severinghaus, J. P., 2014. Enhanced tropical methane production in response to iceberg discharge in the North Atlantic. *Science* 348, 1016–1019.

Rippert, N., Baumann, K.-H., Pätzold, J., 2015. Thermocline fluctuations in the western tropical Indian Ocean during the past 35 ka. *Journal of Quaternary Science* 30, 201–210.

Rodbell, D.T., Seltzer, G.O., Mark, B.G., Smith, J.A., Abbott, M.B., 2008. Clastic sediment flux to tropical Andean lakes: records of glaciation and soil erosion. *Quaternary Science Reviews* 27, 1612–1626.

Romahn, S., Mackensen, A., Groeneveld, J., Pätzold, J., 2014. Deglacial intermediate water reorganization: new evidence from the Indian Ocean. *Climate of the Past* 10, 293-303.

Rupper, S., Roe, G., 2008. Glacier changes and regional climate: a mass and energy balance approach. *Journal of Climate* 21, 5384–5401.

Rupper, S., Roe, G., Gillespie, A., 2009. Spatial patterns of Holocene glacier advance and retreat in Central Asia. *Quaternary Research* 72, 337–346.

Russell, J.M., Eggermont, H.E., Taylor, R., Verschuren, D., 2009. Paleolimnological records of recent glacier recession in the Rwenzori Mountains, Uganda-D.R. Congo. *Journal of Paleolimnology* 41, 253-271.

Sagredo, E.A., Lowell, T.V., 2012, Climatology of Andean glaciers: A framework to understand glacier response to climate change. *Global and Planetary Change* 86-87, 101–109.

Sagredo, E.A., Rupper, S., Lowell, T.V., 2014, Sensitivities of the equilibrium line altitude to temperature and precipitation changes along the Andes. *Quaternary Research* 81, 355–366.

Saltzman, B., Maasch, K.A., 1990. Instability of the global greenhouse gas system as a cause of the ice ages: a low-order dynamical model. *Annals of Glaciology* 14, 358.

Schaefer, J.M., Kaplan, M., Putnam, A., Schlüchter, C., 2009. Southern mid-latitude terminations of MIS-4, the Last Glacial Maximum and the Late Glacial period in the New Zealand moraine record. *Geochimica et cosmochimica acta* 73, 29-29.

Schefuß, E., Schouten, S., Schneider, R.R., 2005. Climatic controls on central African hydrology during the past 20,000 years. *Nature* 437, 1003-1006.

Seltzer, G.O., Rodbell, D.T., Barker, P.A., Fritz, S.C., Tapia, P.M., Rowe, H.D., Dunbar, R.B., 2002. Early warming of tropical South America at the last glacial-interglacial transition. *Science* 296, 1685-1686.

Shakun, J.D., Clark, P.U., He, F., Marcott, S.A., Mix, A.C., Liu, Z., Otto-Bliesner, B., Schmittner, A., Bard, E., 2012. Global warming preceded by increasing carbon dioxide concentrations during the last deglaciation. *Nature* 484, 49–54.

Shakun, J. D., Clark, P. U., Marcott, S. A., Brook, E. J., Lifton, N. A., Caffee, M., Shakun, W.R., 2015. Cosmogenic dating of Late Pleistocene glaciation, southern tropical Andes, Peru. *Journal of Quaternary Science* 30, 841–847.

Shanahan, T., Zreda, M., 2000. Chronology of Quaternary glaciations in East Africa. *Earth and Planetary Science Letters* 177, 23-42.

Singarayer, J.S., Burrough, S.L., 2015, Interhemispheric dynamics of the African rainbelt during the late Quaternary. *Quaternary Science Reviews* 124, 48–67.

Smart, D. F., Shea, M. A., Flückiger, E. O., 2000. Magnetospheric models and trajectory computations. *Space Science Reviews* 93, 305–333.

Smith, C.A., Lowell, T.V., Owen, L.A., Caffee, M.W., 2011. Late Quaternary glacial chronology on Nevado Illimani, Bolivia, and the implications for paleoclimatic reconstructions across the Andes. *Quaternary Research* 75, 1-10.

Smith, J.A., Finkel, R.C., Farber, D.L., Rodbell, D.T., Seltzer, G.O., 2005a. Moraine preservation in the tropical Andes: interpreting old surface exposure ages in glaciated valleys. *Journal of Quaternary Science* 20, 735-758.

Smith, J.A., Seltzer, G.O., Farber, D. L., Rodbell, D. T., Finkel, R. C., 2005b. Early local Last Glacial Maximum in the tropical Andes. *Science* 308, 678–681.

Smith, J. A., Rodbell, D. T., 2010. Cross-cutting moraines reveal evidence for North Atlantic influence on glaciers in the tropical Andes. *Journal of Quaternary Science* 25, 243-248.

Sobel, A.H., Bretherton, C.S., 2000. Modeling tropical precipitation in a single column. *Journal of Climate* 13, 4378-4392.

Sobel, A.H., Held, I.M., Bretherton, C.S., 2002. The ENSO signal in tropical tropospheric temperature. *Journal of Climate* 15, 2702-2706.

Soden, B.J., Held, I.M., 2006. An assessment of climate feedbacks in coupled ocean-atmosphere models. *Journal of Climate* 19, 3354-3360.

Solomina, O.N., Bradley, R.S., Hodgson, D.A., Ivy-Ochs, S., Jomelli, V., Mackintosh, A.N., Nesje, A., Owen, L.A., Wanner, H., Wiles, G.C., Young, N.E., 2015. Holocene glacier fluctuations. *Quaternary Science Reviews* 111, 9–34.

Son, S.-W., Kim, S.-Y., Min, S.-K., 2018. Widening of the Hadley Cell from Last Glacial Maximum to Future Climate. *Journal of Climate* 31, 267-281.

Stansell, N.D., Rodbell, D.T., Licciardi, J.M., Sedlak, C.M., Schweinsberg, A.D., Huss, E.G., Delgado, G.M., Zimmerman, S.H., Finkel, R.C., 2015. Late Glacial and Holocene glacier fluctuations at Nevado Huaguruncho in the Eastern Cordillera of the Peruvian Andes. *Geology* G36735.1–4.

Stansell, N.D., Licciardi, J.M., Rodbell, D.T., Mark, B.G., 2017. Tropical ocean-atmospheric forcing of Late Glacial and Holocene glacier fluctuations in the Cordillera Blanca, Peru. *Geophysical Research Letters* 44, 4176–4185.

Stocker, T.F., Qin, D., Plattner, G.K., Tignor, M., Allen, S.K., Boschung, J., Nauels, A., Xia, Y., Bex, V., Midgley, P.M., 2013. IPCC, 2013: Climate Change 2013: The Physical Science Basis. Contribution of Working Group I to the Fifth Assessment Report of the Intergovernmental Panel on Climate Change, 1535 pp.

Stone, J.O., 2000. Air pressure and cosmogenic isotope production. *Journal of Geophysical Research* 105, 23753-23759.

Stroup, J.S., Kelly, M.A., Lowell, T.V., Applegate, P.J., Howley, J.A., 2014. Late Holocene fluctuations of Qori Kalis outlet glacier, Quelccaya Ice Cap, Peruvian Andes. *Geology* 42, 347-350.

Tanaka, H.L., Ishizaki, N., Nohara, D., 2005. Intercomparison of the intensities and trends of the intensities and trends of Hadley, Walker, and monsoon circulations in the global warming projections. *SOLA* 1, 77-80.

Taylor, R.G., Mileham, L., Tindimugaya, C., Majugu, A., Muwanga, A., Nakileza, B., 2006. Recent glacial recession in the Ruwenzori Mountains of East Africa due to rising air temperature. *Geophysical Research Letters* 33, L10402.

Thompson, L.G., Mosley-Thompson, E., Davis, M.E., Henderson, K.A., Brecher, H.H., Zagorodnov, V.S., Mashiotta, T.A., Lin, P.N., Mikhalenko, V.N., Hardy, D.R., Beer, J., 2002. Kilimanjaro ice core records: Evidence of Holocene climate change in tropical Africa. *Science* 298, 589–593.

Thompson, L.G., Brecher, H.H., Mosley-Thompson, E., Hardy, D.R., Mark, B.G., 2009. Glacier loss on Kilimanjaro continues unabated. *Proceedings of the National Academies of Science* 106, 1–6.

Thompson, L.G., Mosley-Thompson, E., Davis, M., Mountain, K., 2011. A paleoclimatic perspective on the 21st-century glacier loss on Kilimanjaro, Tanzania. *Annals of Glaciology* 52, 60-68.

Tiercelin, J.J., Gibert, E., Umer, M., Bonnefille, R., Disnar, J.R., Lézine, A.M., Hureau-Mazaudier, D., Travi, Y., Keravis, D., Lamb, H.F., 2008. High-resolution sedimentary record of the last deglaciation from a high-altitude lake in Ethiopia. *Quaternary Science Reviews* 27, 449–467.

Tierney, J.E., Russell, J.M., Huang, Y., Damsté, J., 2008. Northern hemisphere controls on tropical southeast African climate during the past 60,000 years. *Science* 322, 252-255.

Ullman, D.J., Carlson, A.E., LeGrande, A.N., Anslow, F.S., Moore, A.K., Caffee, M., Syverson, K.M., Licciardi, J.M., 2015. Southern Laurentide ice-sheet retreat synchronous with rising boreal summer insolation. *Geology* 43, 23–26.

Vecchi, G.A., Soden, B.J., 2007. Global warming and the weakening of the tropical circulation. *Journal of Climate* 20, 4316-4340.

Verschuren, D., Damsté, J., Moernaut, J., Kristen, I., 2009. Half-precessional dynamics of monsoon rainfall near the East African Equator. *Nature* 462, 637-641.

Vuille, M., Francou, B., Wagnon, P., Juen, I., Kaser, G., Mark, B.G., Bradley, R.S., 2008. Climate change and tropical Andean glaciers: Past, present and future. *Earth-Science Reviews* 89, 79-96.

Walker, M.J., Berkelhammer, M., Björck, S., Cwynar, L.C., Fisher, D.A., Long, A.J., Lowe, J.J., Newnham, R.M., Rasmussen, S.O. and Weiss, H., 2012. Formal subdivision of the Holocene Series/Epoch: a Discussion Paper by a Working Group of INTIMATE (Integration of ice-core, marine and terrestrial records) and the Subcommittee on Quaternary Stratigraphy (International Commission on Stratigraphy). *Journal of Quaternary Science* 27, 649-659.

Weber, M.E., Clark, P.U., Kuhn, G., Timmerman, A., Sprenk, D., Gladstone, R., Zhang, X., Lohmann, G., Menviel, L., Chikamoto, M.O., Friedrich, T., 2014. Millennial-scale variability in Antarctic ice-sheet discharge during the last deglaciation. *Nature* 510, 134-138.

Weijers, J.W.H., Schefuss, E., Schouten, S., Damste, J.S.S., 2007. Coupled Thermal and Hydrological Evolution of Tropical Africa over the Last Deglaciation. *Science* 315, 1701–1704.

Weldeab, S., Schneider, R.R., Kölling, M., Wefer, G., 2005. Holocene African droughts relate to eastern equatorial Atlantic cooling. *Geology* 33, 981-984.

Weldeab, S., Menke, V., Schmiedl, G., 2014. The pace of East African monsoon evolution during the Holocene. *Geophysical Research Letters* 41, 1724-1732.

Wesnousky, S. G., Aranguren, R., Rengifo, M., Owen, L. A., Caffee, M. W., Murari, M. K., Perez, O. J., 2012. Toward quantifying geomorphic rates of crustal displacement, landscape development, and the age of glaciation in the Venezuelan Andes. *Geomorphology* 141-142, 99–113.

Whittow, J.B., Shepherd, A., Goldthorpe, J.E., 1963. Observations on the glaciers of the Ruwenzori. *Journal of Glaciology* 4, 581-616.

Woltering, M., Johnson, T.C., Werne, J.P., Schouten, S., Damsté, J.S.S., 2011. Late Pleistocene temperature history of Southeast Africa: a TEX86 temperature record from Lake Malawi. *Palaeogeography, Palaeoclimatology, Palaeoecology* 303, 93-102.

Yang, W., Seager, R., Crane, M.A., 2015. The Annual Cycle of East African Precipitation. *Journal of Climate* 28, 2385-2404.

Young, N.E., Briner, J.P., Schaefer, J., Zimmerman, S., Finkel, R.C., 2019. Early Younger Dryas glacier culmination in southern Alaska: implications for North Atlantic climate change during the last deglaciation. *Geology (in press)*.

Zech, R., Kull, C., Kubik, P. W, Veit, H., 2007. LGM and Late Glacial glacier advances in the Cordillera Real and Cochabamba (Bolivia) deduced from ^{10}Be surface exposure dating. *Climate of the Past* 3, 839–869.

Zech, J., Zech, R., May, J.-H., Kubik, P.W., Veit, H., 2010. Lateglacial and early Holocene glaciation in the tropical Andes caused by La Niña-like conditions. *Palaeogeography, Palaeoclimatology, Palaeoecology* 293, 248–254.

Zweck, C., Zreda, M., Desilets, D., 2013. Snow shielding factors for cosmogenic nuclide dating inferred from Monte Carlo neutron transport simulations. *Earth and Planetary Science Letters* 379, 64-71.